Pile Dredging in Cohesive Soils

Experimental research on the influence of different dredging configurations

Master of Science Thesis

Delft, 2022

Author:
Bilal Aouragh, 4253310

Graduation committee:

Dr.ir. S.A. Miedema	Delft University of Technology
Prof. dr. ir. C. van Rhee	Delft University of Technology
Dr. P.L. Pahlavan	Delft University of Technology
Dr. ir. A.J. Nobel	Royal Boskalis Westminster N.V.
Ir. I. van Giffen	Royal Boskalis Westminster N.V.

TU Delft Delft University of Technology

Boskalis

Preface

This report forms the closure of the Master of Science (MSc) program in Offshore and Dredging Engineering at the Delft University of Technology. The corresponding graduation project was carried out under supervision of Royal Boskalis Westminster N.V. in Papendrecht.

I am very grateful to Boskalis and in particular to the Research and Development department for giving me the opportunity to graduate on such an interesting subject that combines both theoretical as experimental research. I would like to take this opportunity to thank both Arno Nobel and Ike van Giffen for their unstinting efforts and support. Their input, enthusiasm and their ability to always keep a critical eye really motivated me to push on, especially during the Covid-19 lockdowns. Furthermore, a big thanks to the chairman of the graduation committee Sape Miedema for his insight and helpful advice during the entire length of this track, to all the colleagues at Boskalis Capelle for the assembly of the tool at site and to Ed Stok and Andre van den Bosch for their support in the laboratory, building the test setup and their willingness to help wherever possible.

Finally, I am very grateful to my parents, who supported me with love and understanding throughout the entire duration of my study. Without your everlasting support I would not have come this far.

Bilal Aouragh
Den Haag

Abstract

After decades of exploitation of hydrocarbons, the offshore facilities constructed for this purpose are nearing the end of their design life and/or economic operation. According to international law, these offshore structures need to be completely removed. Decommissioning of the substructures often requires for soil to be removed in piles to facilitate pile cutting works below the seabed. One way of achieving this is by deploying a specialized tool, a so-called Soil Plug Removal Tool (SPRT), that operates using hydraulic excavation.

This research carried out under supervision of Royal Boskalis Westminster N.V. aims to get a more solid basis for comparison of different SPRT concepts that are available in the market. The tools are designed to handle a wide range of soil types. Removal of cohesive sediment is more challenging, mainly due to the very low water permeability present compared to granular soils. This study therefore focusses on the excavation of cohesive soil types only.

In order to verify the performance of several concepts an experimental test program is set up on model scale. The primary goal is to investigate the achievable excavation production in terms of tool progress rate. Therefore, a jetting tool is developed that covers the (complete) spectrum in terms of cohesive soils and performance of the available tools. Two basic SPRT concepts are incorporated in this single tool based on head movement: static or rotating.

Jet pressure, clay strength, rotational velocity and set down pressure of the tool are altered during testing on the condition that all other parameters are fixed. This requirement is met for the testing clay by merely varying the shear strength. The testing clay was therefore prepared both with an artificial and natural clay with shear strengths ranging from 20 kPa to 100 kPa.

It is found that next to jetting, soil failure can also be attributed to cutting and jet trench failure under influence of the jetting head that rests on top of the clay. For this reason, production values belonging to jetting could not be obtained directly and had to be calculated using jetting theory to distinguish between jetting and jet trench failure. Based on the power that is required to excavate a certain volume of soil (i.e. specific energy), insight is given in the contribution of each failure mechanisms to the production in terms of tool progress rate.

During static jetting, the current (nozzle) configuration did not remove enough soil from the jet cavities for the jetting tool to progress downwards. The opposite is true for the rotational tests which comprise the largest part of the test series. An analytical model is proposed to predict the cavity width and depth. This model is only valid for jets with small rotational velocities as encountered in this study.

The total production, which was measured, is found to be inversely proportional to shear strength and directly proportional to jet pressure and rotational velocity.

Table of contents

Nomenclature

Roman letters

a	Adhesion	Pa
a_v	Coefficient of compressibility	$-$
$a_{1,2}$	Auxiliary variable	$-$
A	Adhesive force on the blade	N
A	Surface area	m^2
$b_{1,2}$	Auxiliary variable	$-$
c'	Cohesion	Pa
c_c	Contraction coefficient	$-$
c_d	Discharge coefficient	$-$
c_v	Loss coefficient	$-$
C	Cohesive force on shear plane	N
CR	Cutting Ratio	$-$
CSR	Cement to Soil Ratio	%
CWR	Cement to Water Ratio	kg/m^3
$C_{1,2,3,4}$	Pump coefficients	$-$
D	Diameter	m
e	Void ratio	$-$
ESP	Specific Energy	Pa
f	Darcy-Weisbach friction coefficient	$-$
F	Force	N
Fr	Froude number	$-$
g	Gravitational constant	m/s^2
h_i	Clay layer thickness	m
H	Height	m
I	Momentum flux	N
JR	Jetting Ratio	$-$
k	Hydraulic conductivity	m/s
k_1, k_2	Empirical constants	$-$
K	Dimensionless resistance coefficient	$-$
L	Length	m
m	Mass	kg
n	Porosity	$-$
n	Rotational speed	rpm
N_{bc}	Bearing capacity factor	$-$
N_1	Normal force on shear plane	N
N_2	Normal force on blade	N
PI	Plasticity Index	%
q	Flux or discharge per unit area	m/s
p	Pressure	Pa
p_0'	Effective overburden pressure	Pa
p_c	Consolidation pressure	Pa
$prod$	Progress rate production	cm/min

P	Power	W
P_r	Production	Kg/m^3
q_{bc}	Bearing capacity	Pa
Q	Flow rate or discharge	m^3/s
r	Radial distance to centreline of the jet	m
r_{ac}	Ratio adhesive force to cohesive force	$-$
r_T	Ratio adhesive force to tensile force	$-$
R	Radius	m
Re	Reynolds number	$-$
s	Jet distance, measured along the centreline of the jet	m
s_u	Undrained shear strength	Pa
S	Degree of saturation	$-$
SOD	Stand off distance	m
t	Time	s
u	(isotropic) pore water pressure	Pa
u	Velocity	m/s
v_p	Vertical progress rate of the jetting tool	cm/min
v_r	Rotational velocity of the jetting tool	m/s
V_{cbw}	Volume of clay-bound water fraction	$-$
V_p	Volume of pores	m^3
V_t	Total volume	m^3
V_w	Volume of water	m^3
w	Water content	$-$
W_c	Cavity width	m
Z_c	Cavity depth	m

Greek letters

α	(Blade) angle	rad
α_{nom}	Entrainment coefficient	$-$
β	Angle of the shear plane with the direction of cutting velocity	rad
Δp_E	Euler pressure	Pa
ε	Strain	$-$
$\dot{\varepsilon}$	Strain rate	$1/s$
η	Efficiency	$-$
λ_{HF}	Horizontal cutting force coefficient Flow Type	$-$
λ_{HT}	Horizontal cutting force coefficient Tear Type	$-$
λ_s	Strain rate factor average adhesion and cohesion	$-$
λ_{VT}	Vertical cutting force coefficient Tear Type	$-$
μ	Dynamic viscosity	$Pa \cdot s$
μ_F	Coefficient of friction	$-$
ρ	Density	kg/m^3
σ	Total stress applied normal to the shear plane	Pa
σ_d	Cavitation number of cone development	$-$
σ_i	Cavitation inception index	$-$

σ_t	Tensile strength	Pa
σ'	Effective stress	Pa
$\sigma'_\perp$	Effective normal compressive stress	Pa
$\sigma_1, \sigma_2, \sigma_3$	Principal stresses	Pa
τ	Shear strength	Pa
ϕ	Internal friction angle	$-$
ω	Angular velocity	rad/s

Subscripts

a	Airlift
atm	Atmospheric
$a0$	Ambient
c	Cutting
com	Combined
cav	Cavitation
cav, i	Cavitation inception
dr	Development region
e	Engine
eff	Effective
fr	Frictional losses in pump driveline
g	Gravitational
h	Horizontal
hyd	Hydraulic
i	In
j	Jet
max	maximum
n	Nozzle
nb	Near bed
o	Out
p	Pile
$pile + c$	Pile+pile contents
sd	Set down
ss	Original soil surface
$stag$	Stagnation
tf	Trench failure
tw	Tool weight
T	Tool
v	Vertical
va	Vapour
w	water
0	At nozzle exit or initially

Abbreviations

AC	Artificial Clay
BX	Batch X with $X = 1 - 11$
DP	Dredge Pump
HP	High Pressure ($p_j = 130\ bar$)
LP	Low Pressure ($p_j = 3\ bar$)
LSP	Large Submersible Pump
MP	Medium pressure ($p_j = 30\ bar$)
NPT	National Pipe Thread
NC	Natural Clay
NX	Nozzle X with $X = 1 - 8$
PP	Perforated Plate
SF	Scale Factor
SP	Supply Pump
$SPRT$	Soil Plug Removal Tool
SSP	Small Submersible Pump

1 Introduction

1.1 Background

After decades of exploitation of hydrocarbons, the facilities constructed for this purpose are nearing the end of their design life and/or economic operation. The number of installations which are reaching this end will steadily increase in the upcoming years mainly due to depletion of existing oil and gas wells offshore. This does not mean however that these platforms can simply be abandoned after the completion of all activities related to the extraction of hydrocarbons.
Abandoned platforms pose two main problems. Firstly, they can consist of a threat to the safety of other offshore activities like fishery and navigation and secondly, they can be destructive to the marine environment present. Abandoned and decommissioned installations should therefore be completely removed in accordance with the Geneva Convention on the Continental Shelf, effectual since 1958 (Trevisanut, 2020).

Royal Boskalis Westminster NV is a specialized contractor in the offshore installation and decommissioning field (see Figure 1-1). For decommissioning and thus removal of offshore platforms often soil needs to be removed from inside the piles. This is mostly done to facilitate pile cutting works below the seabed.


Figure 1-1: Bokalift 1 decommissioning Viking Vulcan jacket structures and topsides

Therefore, the problem of managing and removing these offshore platforms urgently presents itself. The entire decommissioning process goes through four stages: preparation, dismantling, transport and onshore recycling/disposal. The most crucial link in this chain is the actual dismantling of the platform. A large amount of the offshore platforms deployed at sea consist of a jacket substructure as shown in Figure 1-2. About 95% of the offshore platforms worldwide make use of this steel space frame which consists of plate girder or deck truss structure supported by tubular welding. In the North Sea these foundation structures are often applied up to water depths of $60\ m$.

Figure 1-2: Jacket substructure in which four piles are driven through the jacket legs

The jacket foundation is provided by open-ended tubular steel piles, which are piled into the seabed and serve as a foundation for the entire platform. There are two methods commonly encountered in offshore pile installation for jacket/pile arrangement:

1. Pile through-leg: the pile is installed directly in one of the corner legs of the jacket
2. Skirt pile: the pile is installed through a pile sleeve at the base of the jacket

An overview of the methods mentioned here is given in Figure 1-3. The piles are driven approximately $40 - 80\ m$, and in some cases $120\ m$ deep into the seabed.

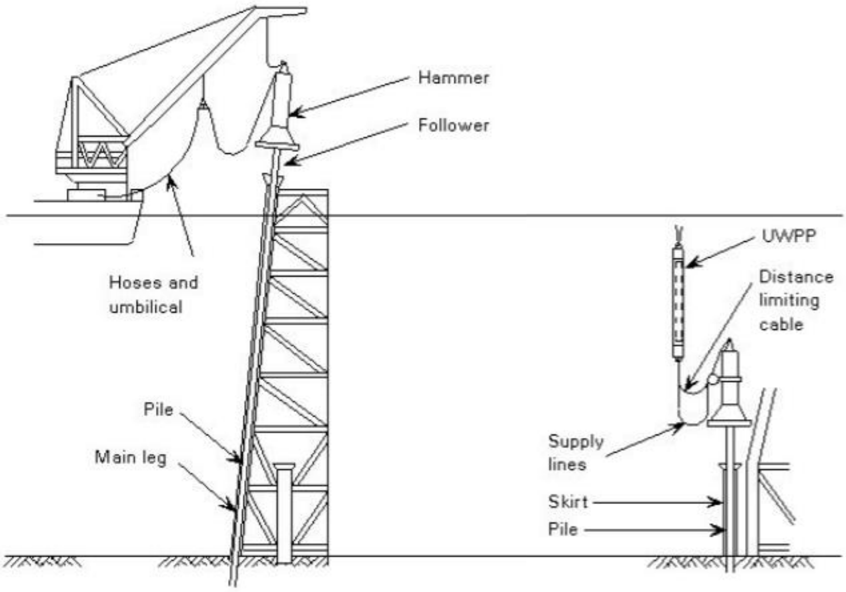

Figure 1-3: Jacket/pile arrangement. Left picture: Pile through-leg. Right picture: Skirt pile.

After removing the platform, these piles also need be withdrawn from the seabed. Legislation (in the Netherlands) indicates that a section of at least $6 - 7\ m$ underneath the mudline must be removed. Preferably this is done with a tool specifically designed for pile cutting works below the seabed and thus deployed inside the pile, instead of from the outside which is more common in cutting works above the mudline. The soil plug inside the pile still needs to be removed first in order for the cutting tool to reach the correct depth where it can operate by using abrasive jets that can cut through steel pile wall. This thesis report will focus on the former (i.e. soli plug removal) over the latter (i.e. pile cutting).

1.2 Problem description and objectives

Many subcontractors have their specific tools, so called Soil Plug Removal Tools (i.e. SPRT), for removal of stiff clay and/or sands in piles. These tools use water jets to loosen the soil, after which it is removed by means of a suction line. A cross section of such a SPRT is shown in Figure 1-4, illustrating the general working method. In short: a tool with the ability to hydraulically excavate soil (pressurized water through nozzles) is placed inside a pile forming a slurry, which then is removed through a suction line. Certain tools have the additional ability of rotating while excavating.

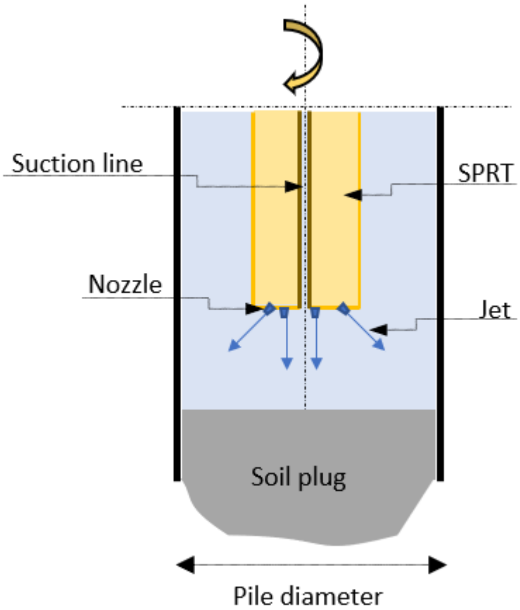

Figure 1-4: Cross section of a typical SPRT placed inside an offshore pile

The main objective for this research, carried out within the Research & Development department of Boskalis, is to get a more solid basis for comparison of the different concepts that are available in the market. This would allow Boskalis to assess the best tool for the job at hand, resulting in the most effective offshore cycle time. The tools that are offered on the market (by subcontractors) will be assessed on the following four points:

- Cost effective design
- Variability in soil conditions
- Robustness and reliability
- Effective and efficient execution

Concerning the performance of the tools there is still a great deal of ground to be gained here by Boskalis in terms of knowledge. Therefore, a contribution needs to be made to the cost competitiveness of the decommissioning industry by theoretically assessing different dredging techniques, selecting the most attractive concepts/tools and performing scale tests to verify the performance of several concepts

For these scale tests a tool will be developed that covers the (complete) spectrum in terms of soil types and performance.
With regard to soil types, it is assumed that excavating a sandy soil layer i.e., non-cohesive sediment is easier than excavating a clayey soil layer i.e., cohesive sediment under the same offshore circumstances. For this reason, considering that cohesion is an intrinsic property, this research will solely focus on clay type soils.

In accordance with all mentioned above, a main research question is formulated:

What is the influence of the dredging configuration on the overall performance for different soil plug removal concepts?

Subsequently the following sub questions are formulated:

- What is the influence of jet pressure?
- What is the influence of clay strength?
- What is the influence of rotational velocity?
- What is the influence of set down pressure of the tool?
- What is the influence of nozzle orientation?

1.3 Research scope

This thesis report focusses on a design assignment in which several scale tests need to be performed in order to get a better understanding of the available SPRT's and their specific advantages/disadvantages over each other. For this, three specific SPRT's will be examined that are manufactured by the leading companies in the pile dredging industry (Deep C, Deco and Claxton) and an in-house tool from Boskalis. A generic overview of the available tools with respect to head configuration, nozzle type and pump pressure is given in Table 1-1.

- Boskalis Airlift 2.0 (*Boskalis*)
- Onslow dredging tool *(Deco)*
- Deep C® SPRT 3000 *(Deep C)*
- Claxton SPRT *(Claxton)*

Table 1-1: Available tools

Tool	Head configuration	Nozzles	Pump pressure
Boskalis	Static	Static	Low pressure
Deco	Rotating	Moving	High pressure
Deep C	Rotating	Static	High pressure
Claxton	Static	Static	High pressure

Although these four SPRT's are examined, they will merely serve as a reference. They will not be reconstructed to a full-scale model. Rather, the idea is to focus on two basic concepts that deal with the different jetting configurations present.

The basic concepts for a SPRT, based on head movement, are as follows:

1. Static head
2. Rotating head

Both concepts will be incorporated in the same tool and will be tested under a variety of different parameters covering the entire scope of the field as has been laid out in the problem description.

In order to narrow the above-mentioned criteria down, a couple of boundary conditions need to be met that are typical for dredging operations in the North Sea:

- Pile diameter: $0.5\ m \sim 1.5\ m$
- Pile embedment: Vertical
- Tool orientation: Centralized
- Soil plug length: $4 - 7\ m$
- Water depth $25 - 60\ m$
- Maximum undrained shear strength: $500\ kPa$
- Vertical displacement method: Vessel crane

These boundary conditions form a starting point for the jet parameters and soil parameters, which are treated in Chapter 3.

1.4 Outline

This thesis report is divided in two distinct parts. The first part is the literature review, in which an analysis of the present knowledge is given that covers the relevant parts of the research field. Both this chapter and Chapter 2 are part of this literature study.

A theoretical background into cohesive soils and their classification as well as performance of submerged turbulent jets and the phenomena that come along with it like cavitation will be discussed in Chapter 2. This chapter also investigates the crucial step of removing the developed slurry mixture from inside the pile by using an airlift or pump system. In the last part, the emphasis is on scaling an actual size setup (i.e. prototype) down to a laboratory setup (i.e. model) with the aim of performing relative simple tests in comparison to the actual size of the setup. Scaling factors in combination with dimensionless indicators like the Froude number will ensure that all relevant parameters can be scaled.

The second part of this report deals with the actual scale tests that will be performed. In Chapter 3 a description of the experimental setup is provided, including all dimensions, equipment, measuring tools, soil types and the designed soil plug removal tool. Chapter 4 establishes the used test program and procedures that are followed before, during and after the experiments. Reproducibility is also treated here. The obtained data is commented upon in Chapter 5. Chapter 6 deals with the analysis of the results as described in the previous chapter by looking into of the tests and comparing the test results to results obtained in practice, with emphasis on the soil that was used during the experiments.

Finally, the conclusions of this thesis report and recommendations for future work are given in Chapter 7.

2 Theoretical background

During pile dredging various mechanisms contribute to the overall performance of the Soil Plug Removal Tool. The main reason to employ such a SPRT is the removal of soil inside a pile. The soil that will be discussed here is clay. Its physical characteristics and behaviour are given in Section 2.1, with a special mention for Subsection 2.1.5 that deals with artificial clays. This clay will be removed by means of hydraulic excavation. In Section 2.2 literature about jetting is reviewed and commented upon. Although hydraulic excavation removes the bulk of the clay, a side effect of placing the SPRT on top of the clay layer is that mechanical excavation will also give a contribution. This cutting of clay will be discussed in Section 2.3. After the soil is excavated by the SPRT either by jetting and/or cutting, the developed soil-water mixture needs to be removed from the pile through a conduit. This can either be done by an airlift or a pump system. For this purpose, in Section 2.4 the mechanism of slurry transport is reviewed. To give insight in the operation of a SPRT, experimental research will be performed in which a scaled version of an actual SPRT is tested. The method of scaling is explained in Section 2.5.

2.1 Clay behaviour and classification

2.1.1 Introduction

Soil is made out of a multiphase accumulation of solid particles, air and water. Soils can roughly be divided in two distinct groups. If the amount of sand and gravel exceeds 50% by weight, the soil will be classified as coarse grained, granular, and *cohesionless*. The soil is classified as fine grained and *cohesive* if the number of fines (i.e. silt and/or clay-size material) exceeds 50% [1].

Soil is often classified by specific ranges of particle sizes (see Figure 2-1). Out of all soil particles, clay particles have the smallest diameters (less than $0.002\ mm$) [2].

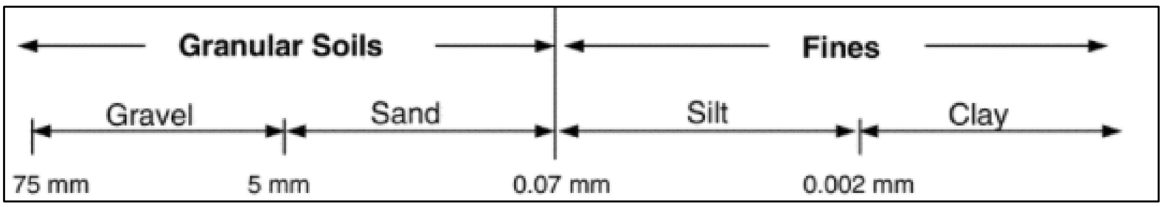

Figure 2-1: Particle size ranges (Mitchell & Soga, 2005)

[1] The terms cohesionless and cohesive must be used with care, as even a few percent of clay mineral in a coarse-grained soil can impart plastic characteristics.

[2] . Most sedimentary rocks are described using both mineral content and particle size. While this is also true for clays, the particle size description is most reliable and most often used.

This report will solely focus on fully saturated soils. Those are soils whose voids are entirely filled with water. This kind of soil mass will decrease in volume when it is exposed to a compressive normal stress, assuming that it was initially in a loose state. In order for such a mass to decrease in volume however, first water must be forced out of its pores (i.e. voids). The level of saturation S is given as the ratio of the volume of water and the total volume of the pore space.

$$S = \frac{V_w}{V_p} \tag{2.1}$$

In which V_w and V_p are the volume of the water and the volume of the pores, respectively. From this equation it is clear that $S = 1$ for a fully saturated soil.

Porosity n is defined by the ratio of the pore volume to the total volume of material present. Porosity effectively represents the storage capacity that is present in each porous body. The primary porosity is made out of the spaces between the grains that together form the material. This applies to both sediment as well as rock. How tighter the grains are packed, the lower the porosity becomes.

$$n = \frac{V_p}{V_t} \tag{2.2}$$

In which the total volume V_t is the sum of the volume of the pores V_p and the volume of the soil V_s. This expression can be rewritten based on the void ratio e. This is the ratio of the volume of pore space to the volume of solid substance in any material consisting of pore space and solid material, such as a soil. The equation reads as follows $n = e/(1 + e)$.

2.1.2 Characteristics

The main characteristics of cohesive soils are:

• very low water permeability

• high skeleton compressibility

• plasticity

Permeability is a measure of the ability of a material such as sediment, porous rock or soil to transmit fluids; thus describing the ease of fluids (mostly water) flowing through the material. Permeability is controlled by packing, form, and sorting of granular materials; the same applies to the porosity mentioned above. Even though clays are very porous, fluids cannot flow easily through the materials structure since the pores are not interconnected. In other words, the fluid will stay trapped in the closed and isolated pores. The effective porosity provides a measure to which extent the pores in a sediment or soil are interconnected.

$$n_{eff} = n - V_{cbw} \tag{2.3}$$

In which n_{eff} is the effective porosity, that is calculated by subtracting the volume of clay-bound water fraction V_{cbw} from the total porosity n. To provide an effective porosity requires an accurate quantification of the volume clay-bound water V_{cbw}. The application of Eq. (2.3) for calculation of accurate effective porosity depends on accurate quantification of the volume of clay-bound water. One way of doing this, is by using elemental capture spectroscopy (ECS).

Clay usually acts as a so-called aquitard i.e., a material that impedes fluid flow, compared to other materials in its surrounding. Darcy's law describes the flow of a fluid through a porous medium:

$$q = -\frac{k}{\mu L} \cdot \Delta p \tag{2.4}$$

In which q is flux or discharge per unit area, k is the hydraulic conductivity or permeability, L is the length of the sample, μ is the dynamic viscosity and Δp stand for the total pressure drop.

This equation, for single phase (fluid) flow, is the defining equation for absolute permeability. The permeability k can be estimated by particle size analysis of the sediment of interest, using empirical equations relating either k to some size property of the sediment. Focussing only on the standard regime of water contents (plastic limit to liquid limit), the permeability of all the clay minerals is less than about $10^{-7}\ m/s$ and may range to values less than $10^{-12}\ m/s$ for some of the monovalent ionic forms of smectite minerals at low porosity. For natural clays this range is narrowed down and spans from 10^{-8} to $10^{-10}\ m/s$ (Mitchell & Soga, 2005). When comparing clay minerals that have the same water content, the values for the permeability are ordered as: smectite (montmorillonite) < attapulgite < illite < kaolinite.

Compressibility of a soil is defined as the property in which a pressure is applied on to the soil and thereby removing air and/or water from the pores; effectively decreasing the volume by bringing soil particles closer to each other compared to the situation prior to mechanical loading.
This phenomenon is expressed in terms of the coefficient of compressibility a_v as the rate of change of void ratio Δe over the applied effective pressure Δp during compression.

$$a_v = \frac{\Delta e}{\Delta p} = \frac{e_o - e_1}{p_1 - p_o} \tag{2.5}$$

In which e_o and e_1 stand for initial and final void ratio, respectively. The given pressures p_o and p_1 are effective pressures, applied initially and at the end of the compression stage. A schematic overview of this relation is given in Figure 2-2.

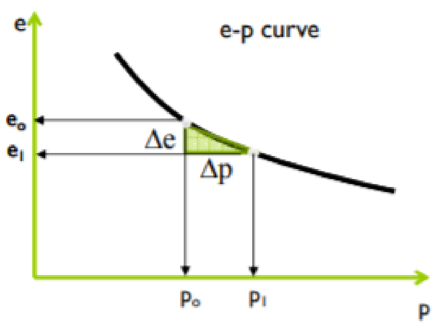

Figure 2-2: void ratio - pressure curve for compressibility

The compressibility of a clay-skeleton is assumed to be higher than that for a granular (non-clay) soil. Furthermore, the relative particle movement in a clay-skeleton is less constrained than is the case for a granular-skeleton (Winterwerp & van Kesteren, 2004). These distinct characteristics of cohesive sediments play a huge role in their response to mechanical loading

In dredging practice, natural layers of saturated clay are often very fast loaded (or unloaded) compared to the rate at which drainage or consolidation can take place. Under these conditions an ideal undrained condition can be assumed. Because of the low permeability and high compressibility of cohesive soils, loading generally generates this undrained response. Such undrained reaction is responsible for the typical behaviour of cohesive sediments. If the time of loading is not restricted however, the behaviour of cohesive sediment will become drained.

Both the clay volume and the amount of water in the clay remain constant during undrained loading, generating excess pore water pressures in the process. The shear strength for such undrained conditions can be defined as the undrained shear strength s_u. Analysing the undrained behaviour of saturated clays in terms of total stresses, assessment of pore water pressures becomes obsolete. Therefore, another analysis method is introduced, the so-called $\phi = 0$ method. This method assumes an undrained shear strength s_u that is equal to the cohesion intercept c_u of the Mohr-Coulomb envelope for total stresses. Consequently, changes in confining stress have no effect on the undrained shear strength of saturated clays provided that the water content remains unchanged.

The consolidation history of the saturated clay plays a key role in understanding the undrained shear strength. For young, normally consolidated clays, it is assumed that the water content is uniquely related to the consolidation pressure p_c. This pressure is equal to the in situ effective overburden pressure p_o'. In this way a linear function between s_u and p_o' becomes apparent. The application of the ratio s_u/p_o' was first suggested by (Skempton, 1948). For (lightly) overconsolidated clays, s_u will be a function of the existing consolidation pressure (or water content w) and the maximum past consolidation pressure p_{cm}. These relations are shown in Figure 2-3. For normally consolidated conditions, the curve of log s_u plotted against w is assumed to be roughly parallel to the virgin compression curve.

In this study, the influence of jetting in clay is examined. Because of the rapid rate of loading caused by a jet, the response of the soil is assumed to be undrained.

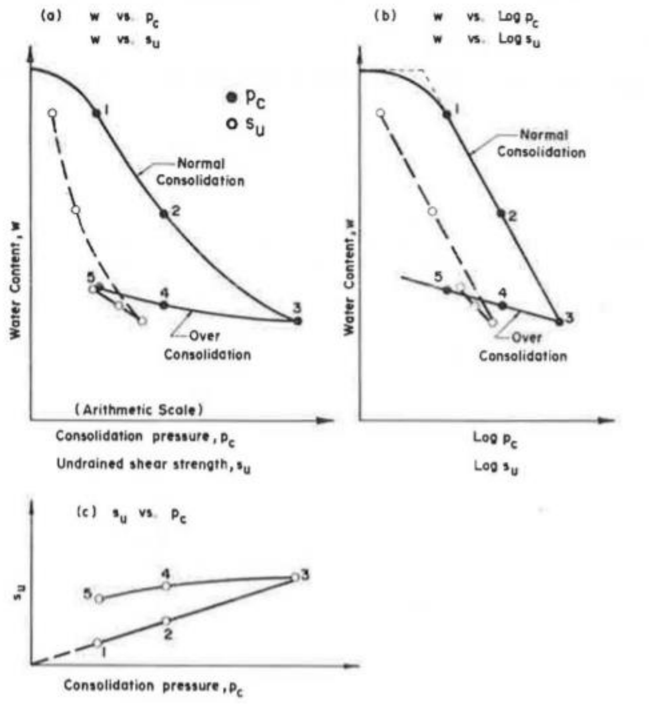

Figure 2-3: Effects of consolidation history on undrained shear strength (Wahls, 1983).

Plasticity

The Atterberg limits are a basic measure of the nature of a fine-grained soil. Depending on the soil water content, it could act in four distinctive ways: solid, semi-solid, plastic and liquid. These four ways are designated by four states, see Figure 2-4. Each state corresponds to a specific list of engineering properties, because of the differences in consistency and overall behaviour of a soil that occur in each state. Hence, the boundary between each state can be defined based on a change in the behaviour of the soil. In practice, the Atterberg limits are used to differentiate between clay and silt, and can also help by differentiating between different types of clays and silts.

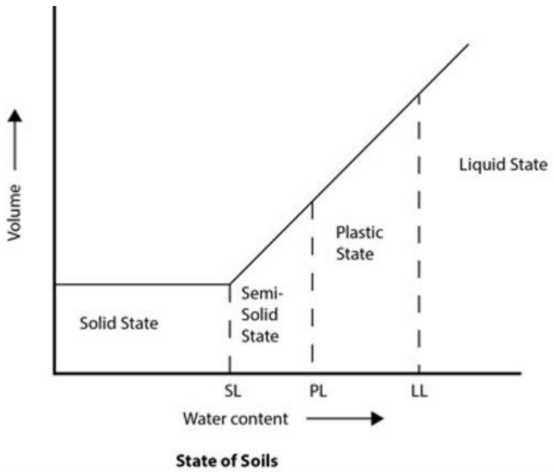

Figure 2-4: Plasticity chart depicting four different soil states

The potential usefulness of the Atterberg limits in soil mechanics was first indicated by (Terzaghi, 1925) when he noted that ‘‘the results of the simplified soil tests (Atterberg limits) depend precisely on the same physical factors which determine the resistance and the permeability of soils (shape of particles, effective size, uniformity) only in a far more complex manner.’’ Further studies led to the formation of a soil classification system based on the Atterberg limits for identification of cohesive soils (Casagrande, 1948).

The *shrinkage limit* (SL) corresponds to the water content in which additional loss of fluid will not result in any more volume decrease. The test to determine the shrinkage limit is the standardized ASTM International D4943. Compared to its counterparts i.e., the liquid and plastic limit, the shrinkage limit is much less frequently used.

The *plastic limit* (PL) corresponds to the water content where soil shifts between brittle and plastic behaviour. Seen from the righthand side of Figure 2-4, a portion of soil reaches its plastic limit when it begins to crumble (displaying brittle behaviour) when rolled to a diameter of $3\ mm$. In order to improve consistency of test results, a $3\ mm$ diameter rod is frequently used to gauge the thickness of the clay while performing a test. The Plastic Limit test is defined by ASTM standard test method D 4318.

The *liquid limit* (LL) corresponds to the water content at which a soil changes from plastic to liquid behaviour. Atterberg's original liquid limit test involved mixing a pat of clay in a round-bottomed porcelain bowl of $10 - 12\ cm$ diameter. After, a groove was cut through the pat of clay with a spatula, and the bowl was then struck many times against the palm of one hand. Casagrande subsequently standardized the apparatus and the procedures to make the measurement more reliable and repeatable.

These limit values can be used in an array of ways and for different purposes. Deriving and implementing the *Plasticity Index (PI)* is an often recurring one. This index gives insight in the plasticity of a soil by measuring it. The size of the range of water contents where the soil exhibits plastic properties is called the plasticity index. Therefore, PI is the difference between the liquid limit and the plastic limit:

$$PI = LL - PL \tag{2.6}$$

Soils with a high PI tend to be clay, those with a lower PI tend to be silt, and those with a PI of 0 (non-plastic) tend to have little or no silt or clay. For clay in a way this makes sense. It signifies the fineness of the soil and its capacity to change shape without altering its volume. From this another characteristic is defined, namely that for higher value of PI the soil compressibility is higher, which correspond to the initial remarks made at the beginning of this subsection.

In (Nobel, 2013) two clay samples were examined with different plasticity indexes. One with $PI = 60\%$ and the other with $PI = 50\%$. No correlational relationship with regard to the final results for jet cavity depth Z_c and width W_c could be established for plasticity. The reason for this is that the jet pressure that is applied (over the complete range of tests) is much higher than the strength of the clay. The same holds for this study. Basically, the lower strength clay layer is being ''pushed off'' by the stronger impinging jets.

However, for a situation where the shear strength of the clay exceeds the jet pressure, plasticity cannot be neglected. For cases with very low jet pressures, the cohesive soil initially needs to swell i.e., decrease in strength by increasing the water content before erosion can take place.

It is important to note that the nozzles on top of a soil plug removal tool are fixed. This implies that jetting with one jet at a certain location will take place. Therefore, the failure of the clay is primarily determined by the jet pressure at this location. After a while jetting will only occur in the created cavity, causing the cavity to increase due to erosion. As discussed before, plasticity may have an influence again due to this secondary process that will be initiated after some time.

In short, PI is only important for drained loading (i.e. surface erosion), which is the case for situations where the shear strength of the clay is higher than the pressure of the water jets. This process of surface erosion takes time (decreasing the strength of the clay by increasing the water content) and it depends on the PI how long this will take.

2.1.3 Effective stress and shear strength

The relationship for effective stress was first proposed by (Terzaghi, 1936). For him, the term 'effective' meant the calculated stress that was effective in moving soil or causing displacements. As noted by Terzaghi: '' all quantifiable effects of a change in stress (compression, distortion, change in shear strength) are due to changes in the effective stress''. It embodies the average stress carried by the soil skeleton. Effective stress σ' acting on a soil is calculated as follows:

$$\sigma' = \sigma - u \tag{2.7}$$

In which σ is the total stress and u is the (isotropic) pore water pressure.

In a so-called soil-water system, that is a system where both soil particles and pore water are present in the same material in order to establish the integrity of the soil. Adding to this soil an external pressure i.e., mechanical loading will result in a pressure development in both the pore water and soil particles. Pressures can also be developed in the gas phase when the soil-water system is partially water-saturated. Therefore, by definition, the effective stresses are the stresses that are developed between soil particles due to stress transfer at the contact points between particles.

Shear strength is a term used in soil mechanics to describe the magnitude of the shear stress that a soil can sustain. The shear strength τ of a soil is mostly given by an equation of the form (Mohr-Coulomb law):

$$\tau = c' + \sigma_{\perp}' \cdot \tan\phi \tag{2.8}$$

In which c' is the cohesion, $\sigma_{\perp}'$ is the effective compressive normal stress on the shear plane and ϕ is the internal friction angle. The effective normal compressive stress is defined as the total normal compressive stress $\sigma_{\perp}$ minus the pore water pressure u: $\sigma_{\perp}' = \sigma_{\perp} - u$ (Terzaghi, 1943).

The shear strength of a soil stems from different soil parameters. Most influential is the packing of soil particles. Soil particles have a certain dense or loose packing relative to each other. When they are packed together, they have to overlap, resulting in an increase in volume, until a certain critical packing is reached. Other aspects that play a role are the friction and interlocking of particles (and possibly bonding or cementation at the contact points of the particles). When a material is exposed to shear strains, some material can contract (contractive behaviour) or expand (dilative behaviour) in volume, due to the interlocking characteristic that is present and prevents the particles to move around one another. During shearing, a lever motion occurs between neighbouring particles, which results in a volume expansion of the soil. A volume expansion leads to a decrease in the density of particles and a decrease in strength. Thus, the peak strength would be followed by a reduction in shear stress.

The relationship of stress-strain determines when the material stops expanding or contracting, and when inter-particle bonds are broken. The theoretical state at which the shear stress and density remain constant while the shear strain increases is called the critical state, steady state, or residual strength.

Under undrained shear circumstances, if particles are enclosed by a (nearly) incompressible fluid such as water the density of the soil particles is not able to change without drainage. The water pressure and the effective stress will change, however. Under this undrained and constant volume shearing, the Mohr–Coulomb criterion reduces to the Tresca criterion ($\phi = 0$) and can be applied to predict the shear strength during undrained conditions. The Tresca (yield) criterion, based on Mohr's circle is defined as:

$$s_u = \frac{1}{2} \cdot (\sigma_1 - \sigma_3) \tag{2.9}$$

The Mohr representation of the principal stresses (σ_1 , σ_2 and σ_3) acting on a sample is shown in Figure 2-5. The normal and shear stresses acting on any section, such as the one shown in the diagram in the top left corner of the figure, are contained in the largest circle defined by the most right stress σ_1 and most left stress σ_3.

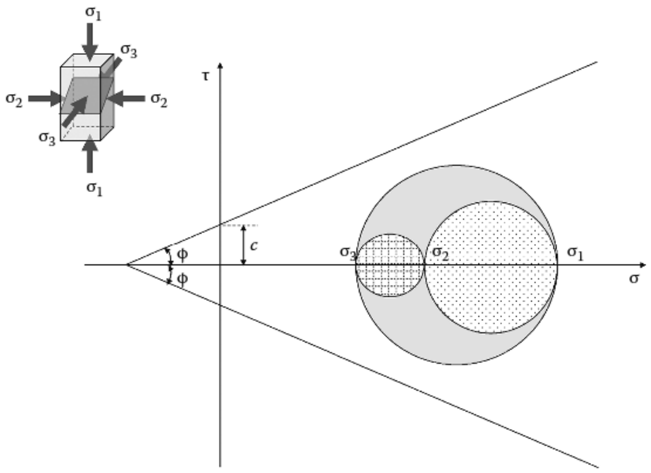

Figure 2-5: Mohr representation of stresses in three-dimensional system (Yong et al., 2012).

2.1.4 Stress strain behaviour

During jetting the soil fails in a fraction of a second and will experience a large strain rate $\dot{\varepsilon}$.
The undrained peak shear strength of cohesive soils depends on the strain-rate. The higher the strain-rate, the higher the viscous resistance and the higher the undrained shear strength s_u. This is described in the following equation:

$$\frac{s_u}{s_{u,ref}} = 1 + n_{sr} \cdot \log\left(\frac{\dot{\varepsilon}}{\dot{\varepsilon}_{\mathrm{ref}}}\right) \tag{2.10}$$

In which $s_{u,ref}$ is the reference undrained shear strength determined at a strain rate $\dot{\varepsilon}_{\mathrm{ref}}$ and n_{sr} is an empirical constant.

(Kulhawy & Mayne, 1990) found for n_{sr} a value of 0.1, based on 209 shear tests on 26 different cohesive soils. According to (Dayal & Allen, 1975) and (Winterwerp & van Kesteren, 2004) n_{sr} depends on the undrained shear strength.

According to (Soga & Mitchell, 1996) the strain rate dependency of the undrained shear strength can be expressed as follows:

$$\frac{s_u}{s_{u,ref}} = \left(\frac{\dot{\varepsilon}}{\dot{\varepsilon}_{\mathrm{ref}}}\right)^{m_{sr}} \tag{2.11}$$

In which m_{sr} is a rate parameter with a value between 0.018 and 0.087. The corresponding values for n_{sr} are 0.04 and 0.25, respectively ($1 < \dot{\varepsilon}/\dot{\varepsilon}_{ref} < 10.000$). These values correspond well with the values found by (Dayal & Allen, 1975).

2.1.5 Artificial clay

Experiments on cohesive soils are normally conducted on natural clays coming from specific sites. In this report however insight is given in different soil shear strengths and their effect during pile dredging. By focussing on the shear strength of the clay other variables (e.g. adhesion, cohesion plasticity, consistency etc.) need to be kept constant. These so-called control variables are held constant because they could influence the outcomes of the study.

Selecting different natural clays based on their shear strength will undermine the internal validity of the study. It will become impossible to establish a correlational or causal relationship between the variables of interest (e.g. change in shear strength versus excavational production rates).

Understanding the effect of an independent variable (i.e. shear strength) on a dependent variable a uniform artificial clay is suggested by (Zhang et al., 2016). This artificial clay is a mixture of natural clay and cement. The shear strength can be controlled by varying the cement content. A clay preparation system was set up to simulate clay with different shear strengths. Different cement to soil ratio's (CSR's), including 2.5%, 5.0%, and 7.5% were tested in accordance with (Ho, 2005) where artificial clays were produced using kaolin clay and cement. A higher cement content results in greater shear strength. The ratio of water, clay, and cement was kept the same for every artificial clay in order to control the moisture content of the clay. To prevent water loss during curing time the moulds in which the clay was stored were covered by plastic film.

Although (Zhang et al., 2016) did research into trenching in clay by submerged vertical traveling jets, the effect of the shear strength on the trenching depth (see Figure 2-6) gives insight in the trend that most likely can be expected during excavation by submerged rotating jets, namely a production trend that decreases with increasing shear strength.

The only difference a rotating jet has with respect to a translational jet, is the orientation of the direction in which the jet moves. In a straight line or curved for translational and rotational movement, respectively. The principle remains the same, movement in a forward direction.

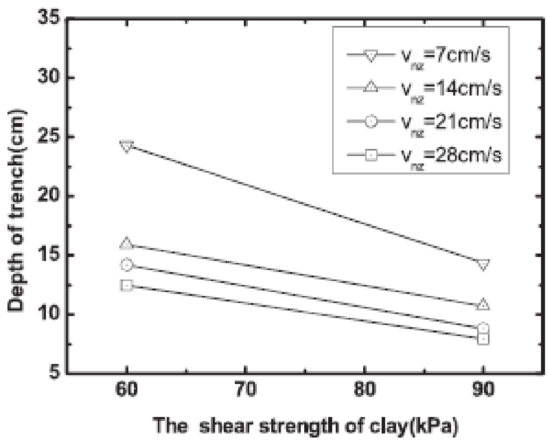

Figure 2-6: The correlation between the depth of the trench and the shear strength of the clay (Zhang et al., 2016)

The test parameters used by (Zhang et al., 2016) are given in Table 2-1. A standoff distance, $SOD = 0$ is applied to all 72 experiments.

Table 2-1: Test parameter for 72 jet trenching tests (Zhang et al., 2016).

Vane shear strength of clay (kPa)	Jet pressure (bar)	Diameter of nozzle (mm)	Translational velocity (cm/s)
$60, 90$	$2, 4, 6$	$9, 12, 16$	$7, 14, 21, 28$

Figure 2-7 shows the correlation between the jet pressure and the depth of the trench. This figure implies that an increase in jet pressure will result in a deeper trench, while keeping other parameters fixed. Subsequently a nearly linear correlation is found.

The effect of the nozzle diameter on the depth of the trench is shown in Figure 2-8. It shows that an increase in nozzle diameter is directionally proportional to the depth of the trenches. Compared to the correlation from Figure 2-7, this correlation is not linear.

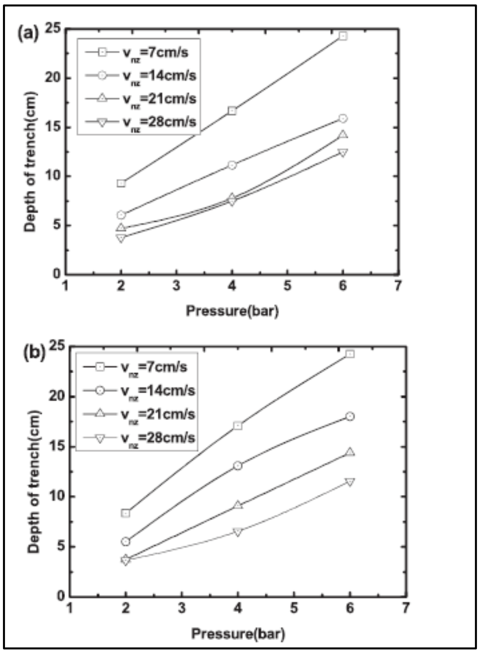

Figure 2-7: The correlation between the jet pressure and the depth of the trench (Zhang et al., 2016).

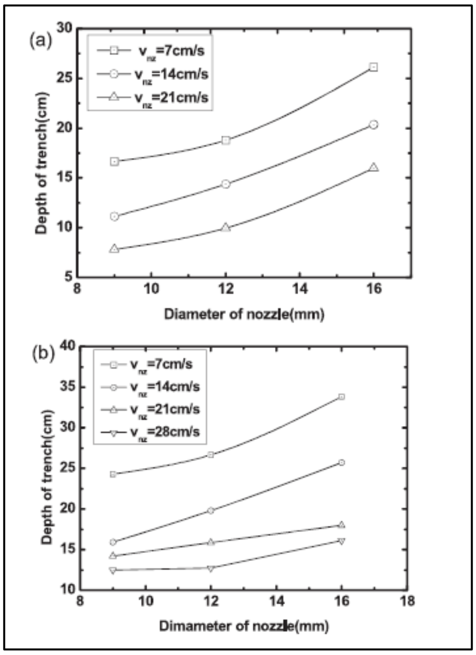

Figure 2-8: The correlation between the depth of the trench and the nozzle diameter (Zhang et al., 2016)

The study performed in this report has a lot in common with the study performed by (Zhang et al., 2016). The linear correlation form Figure 2-7 can certainly be translated to a potential linear correlation between the production and jet pressure. The translational velocity however, is inversely proportional to the depth of the trench. A higher translational velocity represented a shorter exposure time of the clay, and therefore resulted in a less deep trench. This is different for the tests that will be performed in this report, in which the trend between production and rotational velocity is expected to be proportional, since exposure time is less relevant for rotational movement. The jet will return to the same location after each round in contrast to trenching where this is not the case.

The correlation presented in Figure 2-8, can only be relevant to the study performed in this report if the jet momentum flux[3] is kept the same for all nozzle diameters used. Otherwise, an increase in nozzle diameter would imply an increase in flow rate (i.e. flux) and therefore in jet momentum flux (see Section 2.5.3). Reducing the value of the correlation that is found in the process.

2.2 Jet performance

This section discusses the process of hydraulic excavation by water jetting. In dredging practices, a circular turbulent jet is used for excavating cohesive soil and therefore will be highlighted here.

[3] (Zhang et al., 2016) only mentioned that a gate valve was used to control the jet speed by changing the flux to the nozzle. This does not necessarily mean that the jet momentum flux is altered, since this parameter depends on other variables.

2.2.1 Flow field from a nozzle

Before the excavation of a jet in soil is treated first some basic information of jets under water is described. Figure 2-9 shows the flow field from a free circular jet. At the exit position an almost uniform velocity distribution is present. Due to the high difference in velocity between the jet and the surrounding fluid a shear zone or mixing layer will develop. The diameter of the jet will increase with distance and the average flow velocity will decrease in the jet.

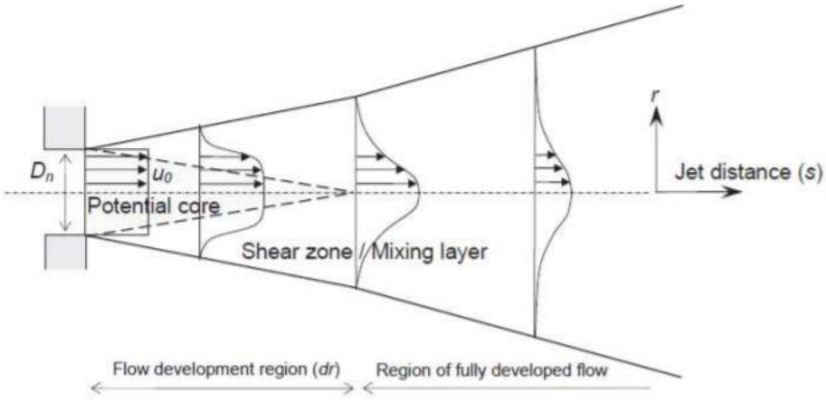

Figure 2-9: Flow field in a free circular jet (Nobel, 2013).

Two zones can be distinguished. The flow development region and the fully developed flow region.

Fully developed flow region

In the developed flow region the velocity profile of a turbulent circular free jet is Gaussian. The velocity distribution can be determined with:

$$u_{s,r} = \sqrt{\frac{k_1}{2}} \cdot u_0 \cdot \frac{D_n}{s} \cdot e^{-k_2 \frac{r^2}{s^2}} \tag{2.12}$$

In which $u_{s,r}$ is the flow velocity in axial direction, u_0 is the initial jet velocity at nozzle exit, D_n is the nozzle diameter, r is the radial distance from the centreline, s is (axial) distance from the nozzle and k_1 and k_2 are empirical constants. Also known as entrainment coefficients, (Fischer, 1979) found for k_1 an average value of 77 $\pm$ 2 and for k_2 an average value of 87.3 $\pm$ 5, based on 13 experimental investigations.

It is important to note that the maximum velocity in the centreline is found when $r = 0$:

$$\frac{u_{s,0}}{u_0} = \sqrt{\frac{k_1}{2}} \cdot \frac{D_n}{s} \approx 6.2 \cdot \frac{D_n}{s} \tag{2.13}$$

This equation is only valid when $s > 6.2D_n$. That is when the region of fully developed flow starts. Rewriting this equation will sort in finding this axial distance:

$$s_{dr} = \sqrt{\frac{k_1}{2}} \cdot D_n \approx 6.2 \cdot D_n \tag{2.14}$$

For shorter distance (in the development region) the velocity on the centreline is equal to u_0. The total discharge in the nozzle increases with distance due to entrainment. The discharge is found by integration of the velocity profile in Eq. (2.11) from $r = 0$ to $r = \infty$:

$$\frac{Q_s}{Q_0} = \sqrt{\frac{8}{k}} \cdot \frac{s}{D_n} \approx 0.32 \cdot \frac{s}{D_n} \tag{2.15a}$$

Or per unit length:

$$\frac{dQ_s}{ds} = \sqrt{\frac{8}{k}} \cdot \frac{Q_o}{D_n} = \frac{\pi}{4} \cdot \sqrt{\frac{8}{k}} \cdot u_0 \cdot D_n = \frac{1}{\sqrt{2k}} \cdot \pi \cdot u_0 \cdot D_n \tag{2.15b}$$

The discharge increases linearly with distance. Both Eq. (2.15a) as (2.15b) are only valid for the fully developed region $s \geq s_{dr}$.

From Eq. (2.14b) the entrainment coefficient can be defined as:

$$\alpha_{mom} = \frac{1}{\sqrt{2k}} \approx 0.081 \tag{2.16}$$

In the region of fully developed flow $s \geq s_{dr}$ the entrainment coefficient is constant.

Flow development region

The mixing layer is not yet fully developed in this region. This results in an entrainment coefficient that is not constant and it will increase with increasing axial distance s. The turbulence that originates from the jet boundary layer steadily moves in the direction of the centre of the jet. The profile of this penetrating turbulence will eventually form a region that is cone shaped. This cone shape is depicted in Figure 2-9 and is named the potential core. The point where the mixing layer overlaps the axis of the jet boundary for the first time is given in Eq. (2.14).

Inside the potential core the velocity is assumed to be constant and equal to the jet exit velocity u_0. For the velocity outside of the potential core all the way up to the outer mixing layer a half Gaussian velocity profile is assumed by (Albertson, 1950). An equation was derived for the discharge in this initial region.

$$Q_{dr} = Q_0 \cdot \left[1 + f_1 \cdot \frac{s}{D_n} + f_2 \cdot \left(\frac{s}{D_n}\right)^2\right] \tag{2.17a}$$

With:

$$f_1 = 2\sqrt{\frac{\pi}{k}} - \sqrt{\frac{8}{k}} \approx 0.081 \tag{2.17b}$$

$$f_2 = \frac{6 - \sqrt{8\pi}}{k} \approx 0.013 \tag{2.17c}$$

Substituting Equations (2.17b) and (2.17c) in (2.17a) gives rise to the following equation:

$$\frac{Q_{dr}}{Q_0} = 1 + 0.081\frac{s}{D_n} + 0.013\left(\frac{s}{D_n}\right)^2 \tag{2.18}$$

In which Q_{dr} is the discharge at location s and Q_0 is the discharge at the nozzle outlet.

Momentum flux

By definition, the turbulent jet is momentum driven. The momentum flux I is conserved on any cross section of the jet flow in axial direction (Rajaratnam, 1976):

$$I_s = \rho_w \cdot 2\pi \int_0^\infty u_{s,r}^2 r \cdot dr = I_0 \tag{2.19}$$

In which I_0 and Q_0 are the momentum flux and flow rate at nozzle exit, respectively:

$$I_0 = \rho_w \cdot Q_0 \cdot u_0 \tag{2.20}$$

$$Q_0 = c_d \cdot \frac{1}{4}\pi \cdot D_n^2 \cdot u_0 \tag{2.21}$$

In which c_d is the nozzle discharge coefficient.

2.2.2 Nozzle discharge

The relation between the pressure drop over the nozzle and velocity and discharge of the nozzle is obtained by application of the Bernoulli equation:

$$p_1 + \frac{1}{2}\rho_w \cdot u_1^2 = p_0 + \frac{1}{2}\rho_w \cdot u_0^2 \tag{2.22}$$

In which p_1 is the pressure upstream of the nozzle, u_1 is the flow velocity upstream of nozzle, p_0 is the pressure in the nozzle and u_0 is the initial jet velocity at nozzle exit (i.e. exit velocity). Often the flow velocity upstream of the nozzle is small compared with the velocity in the nozzle, hence $u_1^2 << u_0^2$ and with the definition of the pressure drop $\Delta p = p_1 - p_0$ the exit velocity reads:

$$u_0 = \sqrt{\frac{2\Delta p}{\rho_w}} \tag{2.23}$$

The discharge Q_0 through the nozzle is now the product of the exit velocity, nozzle area and a discharge coefficient which takes the influence of contraction and hydraulic losses in the nozzle into account. This new equation is found by substituting Eq. (2.23) in Eq. (2.21).

$$Q_0 = c_d \cdot \frac{\pi \cdot D_n^2}{4} \cdot \sqrt{\frac{2\Delta p}{\rho_w}} \tag{2.24}$$

In which Q_0 is the discharge through the nozzle and c_d is the discharge coefficient of the nozzle. The discharge coefficient is the product of the contraction coefficient c_c and loss coefficient c_v.

$$c_d = c_c \cdot c_v \tag{2.25}$$

The contraction coefficient takes into account that not the complete nozzle area is 'used' by the flow. The loss coefficient takes hydraulic losses (for instance due to flow separation in Figure 2-10) into account.

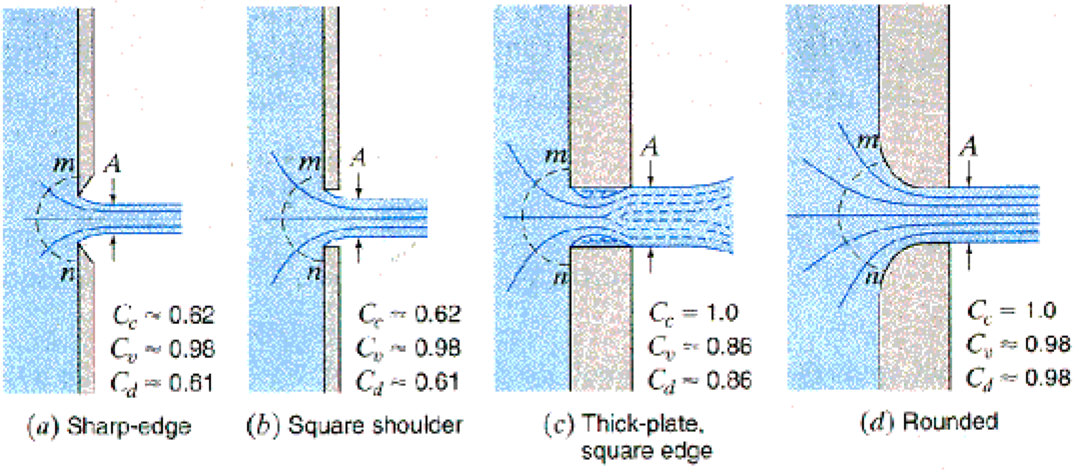

Figure 2-10: Different nozzle shapes with corresponding values for the nozzle coefficients c_c, c_v and c_d (numeric-GmbH, 2015).

The nozzle coefficients corresponding to the four nozzle shapes as depicted in Figure 2-10 are often encountered in dredging practice. Since an ideal situation is never encountered, hydraulic losses should always be considered. Having said that, it is completely possible to design a nozzle with an ideal shape, resulting in a contraction coefficient of $c_c = 1.0$, while keeping the losses as low as possible. This situation is depicted in Figure 2-10 (d).

2.2.3 Stagnation pressure

When a jet hits a surface like the top of a clay layer an excess pressure will develop. This pressure will form shear surfaces in the soil. The soil will fail along these surfaces when the stagnation pressure exceeds the resistance in the shear surfaces. The stagnation pressure is built up at the point of impact as can be seen in Figure 2-11. The magnitude of this so-called stagnation pressure p_{stag} can also be determined using the Bernouilli equation and reads:

$$p_{stag} = \frac{1}{2} \cdot \rho_w \cdot u_s^2 \tag{2.26}$$

In which ρ_w is the density of the water. Hence, the medium used for hydraulic excavation of clays is water.

With Eq. (2.13) the relation between the stagnation pressure and jet pressure p_j reads (for $s/D_n > 6.2$):

$$\frac{p_{stag}}{p_j} = \frac{\frac{1}{2} \cdot \rho_w \cdot u_s^2}{\frac{1}{2} \cdot \rho_w \cdot u_0^2} \approx 38.5 \cdot \left(\frac{D_n}{s}\right)^2 \tag{2.27}$$

The stagnation pressure will eventually decrease due to entrainment of ambient fluid and (cohesive) soil. The distance between the vertical nozzle and the top of the soil surface is called the Stand Off Distance (SOD). When the SOD is relatively small the stagnation pressure will be equal to the jet pressure p_j, $p_{stag} \approx p_j$. According to Eq. (2.22) the stagnation pressure decreases when the jet flow velocity u_s decreases and thus when the jet distance increases

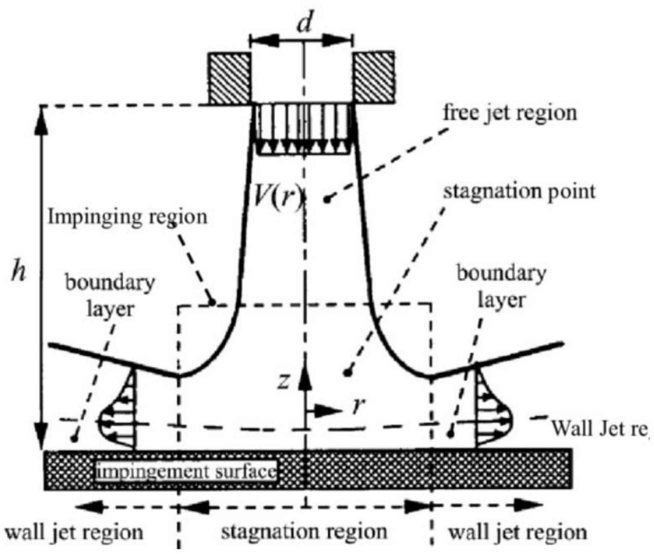

Figure 2-11: schematic of an impinging jet (Rao, 2009).

2.2.4 Cavitating jets

As explained above water is entrained into the shear zone by the large velocity difference between the jet and ambient water. The surrounding flow is accelerated towards the shear zone and by application of Bernoulli's law the pressure will drop along a streamline. When the pressure drops to the vapor pressure cavitation will occur. Cavitation starts when the ratio between the jet pressure and ambient pressure is above a certain value indicated by the cavitation inception index σ_i.

$$\sigma_i = \frac{p_{a0} - p_{va}}{\frac{1}{2} \cdot \rho_w \cdot u_0^2} \approx \frac{p_{a0}}{p_{cav,i}} \tag{2.28}$$

In which p_{a0} is the ambient fluid pressure, $p_{a0} = p_{atm} + \rho_w gH$. Furthermore, p_{va} is the vapor pressure and $p_{cav,i}$ is the jet pressure cavitation inception. This equation is only valid for when the first cavitation bubbles are formed around the jet. This happens at very low jet pressures and they do not influence the jet flow and are therefore less relevant for this study on jetting of clay.

A governing equation which is more relevant for cohesive sediments since cavitation influences the maximum stagnation pressure firstly, is given here:

$$\sigma_d = \frac{p_{a0} - p_{va}}{p_{cav}} \approx \frac{p_{a0}}{p_{cav}} \tag{2.29}$$

In which σ_d is the cavitation number of cone development and p_{cav} is the jet pressure at which the influence of cavitation on the stagnation pressure can be measured, the so-called jet pressure for cavitation cone development.

The value of the cavitation number can vary depending on several factors like the nozzle shape and the fluid properties. The cavitation will show as a vapor cone around the jet (see Figure 2-12). In the figure the nozzle can be observed at the top. At the bottom of the picture a device can be seen that was used to measure the stagnation pressure.

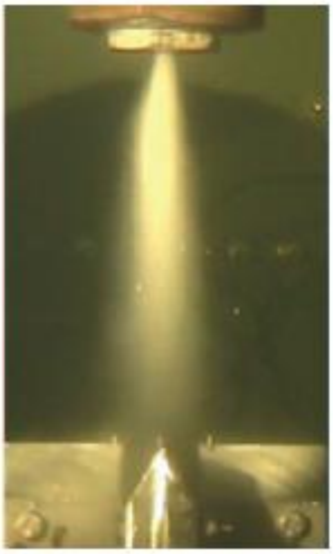

Figure 2-12: cavitating jet (Nobel, 2013).

Figure 2-13 clearly shows the effect of cavitation on the stagnation pressure. The stagnation pressure is normalised with the jet pressure p_j . For a non-cavitating jet the normalized stagnation pressure is only depending on D_n/s as shown in Eq. (2.27). For $D_n/s = 1/12$ this value is approximately 0.27. This value is indicated with the straight hatched line in the figure.

When the jet pressure is increased the normalized stagnation pressure first increases rapidly when the cavitation cone develops and starts growing with jet pressure. After a certain jet pressure, the cone is fully developed (for this SOD) and the normalized stagnation pressure tends to a constant value. The cavitation number σ_d measured during the tests of (Nobel, 2013) was 0.052. The increase in stagnation pressure is caused by less entrainment of ambient water in the jet. The vapor cone decreases the momentum exchange between the jet and ambient water. The reduced entrainment can be expressed with an adapted entrainment coefficient. From the experiments the empirical constant k_{cav} for a developed cavitation cone could be estimated as follows:

$$k_{cav} = k \cdot \sqrt{\sigma_d} \cdot \sqrt{\frac{p_j}{p_{a0}}} \tag{2.30}$$

From this the entrainment coefficient for cavitation can be formulated as:

$$\alpha_{mom,cav} = \sqrt{\frac{1}{2k}} \cdot \sqrt[4]{\frac{\rho_{a0}}{\sigma_d p_j}} \tag{2.31}$$

Substituting Eq. (2.30) for $k = k_{cav}$ in Eq. (2.27), results in the following normalised stagnation pressure:

$$\frac{p_{stag}}{p_j} = \frac{k}{2} \cdot \sqrt{\sigma_d} \cdot \sqrt{\frac{p_j}{p_{a0}}} \cdot \left(\frac{D_n}{s}\right)^2 \tag{2.32}$$

In which p_{ao} is the ambient pressure. From this it is clear that the stagnation pressure is not only depending on the normalized stand off distance, but also on the ratio between the jet- and ambient pressure. The equation is only valid when cavitation occurs hence when $p_j > p_{cav}$ or $p_j > \frac{p_{ao}}{\sigma_d}$.

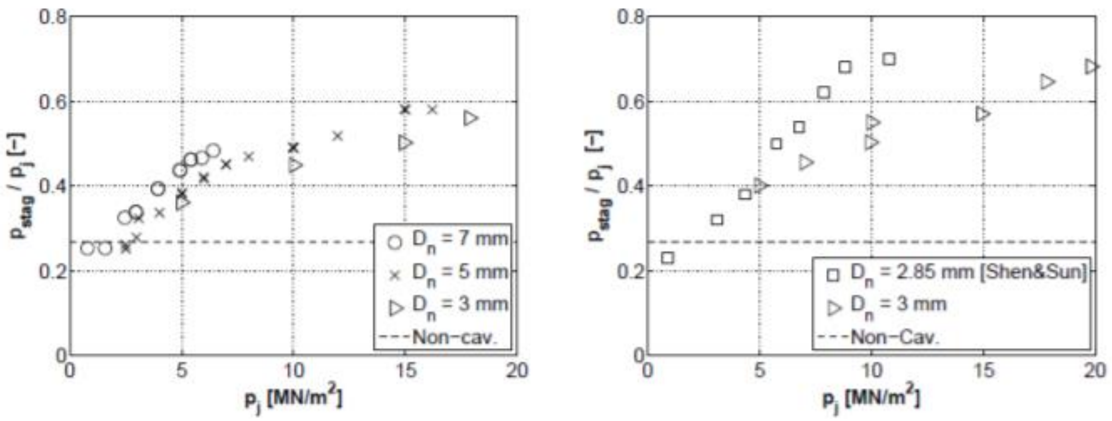

Figure 2-13: Stagnation pressure cavitating jet (Nobel, 2013).

2.2.5 Jetting in clay

In (Nobel, 2013) experimental jetting tests in clay were performed and reported. The test setup used in these experiments consisted of a flume where a block of clay was pressed against a glass wall. After the flume was filled with water a nozzle was transferred over the block. The jet could also be moved close to a glass wall making a visual observation of the hydraulic excavation process possible.

Figure 2-14 shows typical cross sections of the cavities created by the moving jet. The depth / width ratio of the jet cavities is rather large especially for higher values of the jet pressure. Due to the shear strength of the clay the steep side walls remain stable.

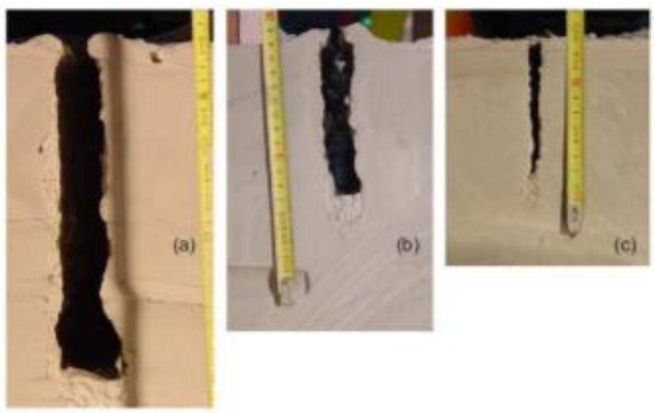

Figure 2-14: Typical cross sections of jet cavity (Nobel, 2013).

Analysis of high-speed video recordings of the penetration process revealed that the jet cavity was created by failure of the clay surface due to the stagnation pressure of the impinging jet on the clay. In previous sections the stagnation pressure is treated. The focus will now be shifted on the bearing strength of clay. In all basic soil mechanical textbooks i.e. (Verruijt, 2004) can be found that the bearing strength of a cohesive soil under a strip loading reads:

$$q_{bc} = N_{bc} \cdot s_u \tag{2.33}$$

In which q_{bc} is the pressure exerted on the clay, s_u is the undrained shear strength of the clay and N_{bc} is the bearing capacity, for undrained failure this value is approximately 5.14 for strip foot loading of a surface (Verruijt, 2004). In this study however, in which a round circular jet is used, this value will correspond to the value of 6.2 as given in Section 2.2.1.

The stagnation pressure therefore reads (see Eq. 2.23):

$$\frac{p_{stag}}{p_{jet}} = f\left(\frac{D_n}{s}\right) \tag{2.34}$$

The stagnation pressure decreases with distance from the nozzle, so when the jet has reached a certain distance in the cavity the pressure will be insufficient to increase depth even further. By combining Equations (2.33) and (2.34) it is therefore expected that the following relation between jet cavity depth Z_c and the jet and soil parameters can be expected:

$$\frac{Z_c}{D_n} = f\left(\frac{p_j}{s_u}\right) \tag{2.35}$$

Figure 2-15 shows the normalized cavity depth as a function of the ratio between the jet pressure and undrained shear strength. The expected relation is clearly visible although scatter is presence because the influence of the transverse (trail) velocity is not included in the above analysis.

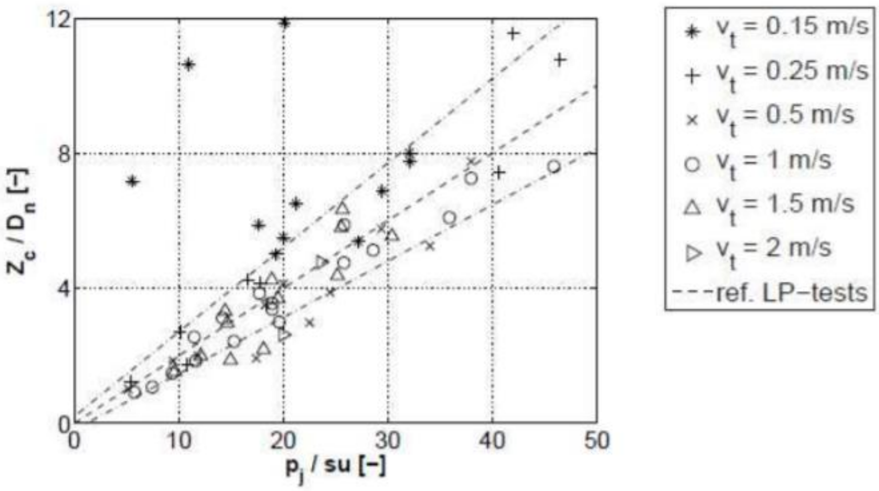

Figure 2-15: Normalized cavity depth low pressure test (Nobel, 2013).

Based on the cavity dimensions and wall structure, four different types of jets / failure modes can be distinguished:

• Penetrating jet: $\frac{p_j}{s_u} > 12$

- narrow deep cavities
- a soil wall structure with small straight nearly vertical nerves
- completely dissolved excavated soil in the jet and ambient water

• Deflecting jet: $7.3 < \frac{p_j}{s_u} < 12$

- shallow cavities
- a soil wall structure with nerves deflecting in opposite of the traverse direction
- after tests only a few dislodged soil lumps can be found

• Dispersing jet: $5.4 < \frac{p_j}{s_u} < 7.3$

- wide shallow cavities
- irregular soil structure
- after tests dislodged soil lumps can be found

• Hydro-fracturing: $v_t < 0.15\ m/s$

- irregular cavity dimensions
- soil fails along preferred weak surfaces
- cavity dimensions can increase significantly compared to the penetrating and deflecting jet

2.2.6 Oblique impinging jets

As for jetting in clay, when it comes to oblique imping jets literature on this topic is rare. Most available literature is made up of studies about water jets discharging in air (or submerged air jets). One study however, performed by (Beltaos, 1976) and further elaborated on by (Jalil & Rajaratnam, 2006) has some interfaces that correspond to this study.

Beltaos performed tests with jets within a H/d range between 15 and 50, in which H stands for the axial distance between the nozzle and the wall (i.e. in this study mentioned as SOD) and d represents the diameter of the nozzle. A schematic overview is given in Figure 2-16. Whilst varying the H/d value within the aforementioned range, Beltaos concluded that the Stand Off Distance has no effect on the overall process. The value for the SOD used here are bigger than those that are encountered in dredging practice. Furthermore, Beltaos is not necessarily focussed on the centrum, where impingement takes place. In this case and only in this case, the effect of the SOD is negligible.

In the present study performed in this report, the nozzles are placed relatively close to the clay layer and in some tests a $SOD = 0$ is present. Additionally, processes taking place near the centre of impingement are more closely watched. As opposed to (Beltaos, 1976), the present study deals with oblique impingement in soil rather than on a flat plate. In short, the SOD does matter in this study.

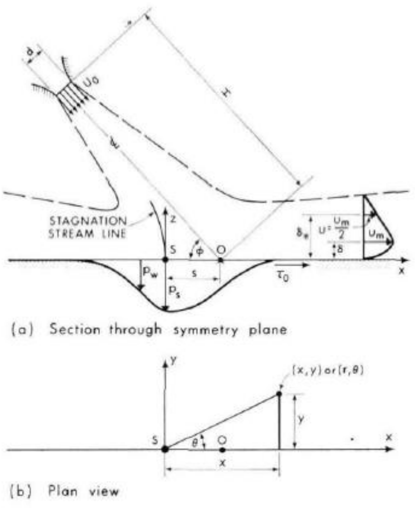

Figure 2-16: Oblique impinging jet (Beltaos, 1976).

Beltaos was also able to provide these conclusions by a couple of equations. The near bed velocity u_{nb} is formulated as follows:

$$u_{nb} = \frac{f\ (\phi_b, \theta_b) \cdot u_0 \cdot D_0}{r} \tag{2.36}$$

And depends on the following function that relates two angles:

$$f\ (\phi_b, \theta_b) = \frac{1.1}{\sqrt{\sin \phi_b}} \cdot \frac{1 + \cos \phi_b \cdot \cos \theta_b}{\cos^2 \theta_b + \left(\frac{\sin \theta_b}{\sin \phi_b}\right)^2} \tag{2.37}$$

In which ϕ_b is the angle between jet and wall in x, z plane and θ_b is the angle between jet and wall in x, y plane. Both equations can be simplified by assuming $\theta_b = 0$. Substituting $\theta_b = 0$ in Eq. (2.37) will result in:

$$f\ (\phi_b, \theta_b) = \frac{1.1}{\sqrt{\sin \phi_b}} \frac{1 + \cos \phi_b}{1} \tag{2.38}$$

Equation (2.36) is then rewritten as:

$$u_{nb} = \frac{1.1}{\sqrt{\sin \phi_b}} \frac{1 + \cos \phi_b}{1} \frac{u_0 \cdot D_0}{r} \tag{2.39}$$

The main findings related to the study performed by (Jalil & Rajaratnam, 2006) are as follows:

- The deflected jet was mostly in the forward direction with very little backward flow for $\theta < 45°$, which increased to an estimated value of about $5 – 10\%$ for the larger angles.
- The transverse thickness profiles in the deflected jet were also found to be similar, with the length scale L in the transverse direction varying mainly with $\frac{x}{d}$ for $\theta = 15°,\ 30°$ and $45°$.
- The velocity profiles in the deflected jet clearly showed the boundary layer in which the velocity profiles were similar and its thickness δ remained constant for $\frac{x}{d}$ up to about 7.5 as in the case of stagnation flows.

The boundary shear stress τ_0 appeared to increase first with the distance from the impingement point and then decrease as in the case of the impingement of submerged impinging jets. This study has shown that the oblique impingement of water jets has some similarities to impinging submerged jets but there are also many important differences. In Figure 2-17 a schematic overview of oblique jet on a plate is given

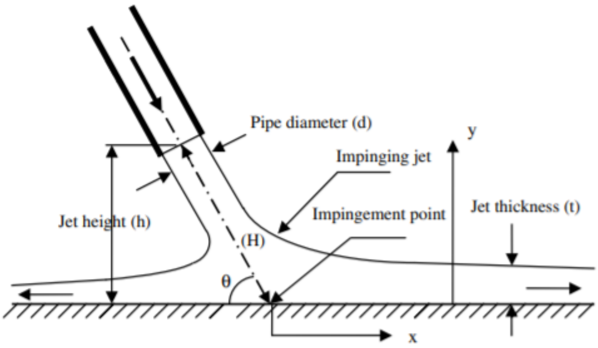

Figure 2-17: oblique impingement of a circular water jet on a flat plate (Jalil & Rajaratnam, 2006).

2.3 Clay cutting

During the process of hydraulic excavation by water jets, also mechanical excavation of the soil by means of cutting is observed. The reason behind this is that the SPRT rests on top of the cohesive soil while excavating it. In the case of a static tool no cutting is observed and the entire excavation is performed by the jets. This is not the case for a rotating tool however, where clay is being removed by both the jets and the frictional contact between the tool and the top layer of the clay.

Three failure mechanisms in soil cutting are distinguished by (Hatamura & Chijiiwa, 1977). The Shear Type, the Flow Type and the Tear Type. The Shear Type only occurs in cohesionless soils like sand. The Flow Type and Tear Type on the other hand occur in cohesive soils like clay. A fourth mechanism, the Curling type is mentioned in (Miedema, New developments of cutting theories with respect to dredging, the cutting of clay, 1992). All four types were derived for different cutting methods in dredging engineering. As opposed to these methods (e.g., cutter heads of cutter suction dredges, dredging wheels of wheel dredges, drag heads of trailing suction hopper dredges and other devices) a Soil Plug Removal Tool does not incorporate blades in its design. The only section of such a tool that comes into direct contact with the soil, while rotating, is the bottom part of the metal housing of the tool. This can be modelled as a round metal plate that shears the top of the clay layer inside the pile. This process corresponds to the two failure mechanism encountered in clay, namely the Flow Type and Tear Type as shown in Figure 2-18 and Figure 2-19, respectively.

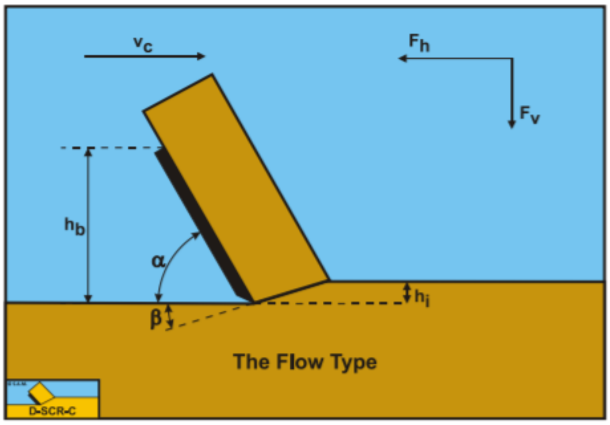

Figure 2-18: Flow Type cutting mechanism (Miedema, 2019).

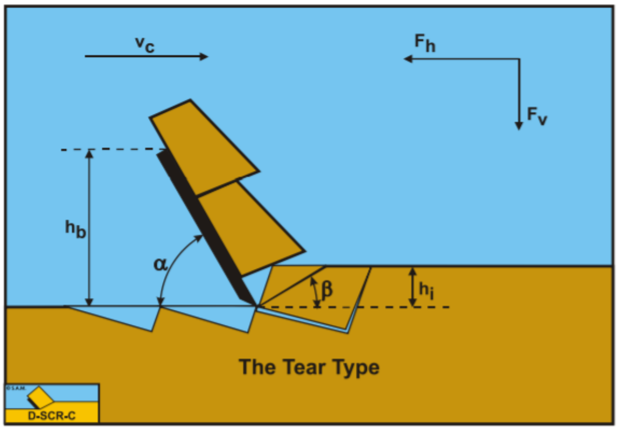

Figure 2-19: Tear type cutting mechanism (Miedema, 2019).

Flow type

This failure mechanism is most commonly encountered in (natural) clay. It is assumed that these clays are plastic and therefore exhibit the mechanism ductile process that is encountered in this failure mechanism. Figure 2-20 and 2-21 illustrate the forces on the layer of soil and the forces on a straight blade when cutting soil, respectively.

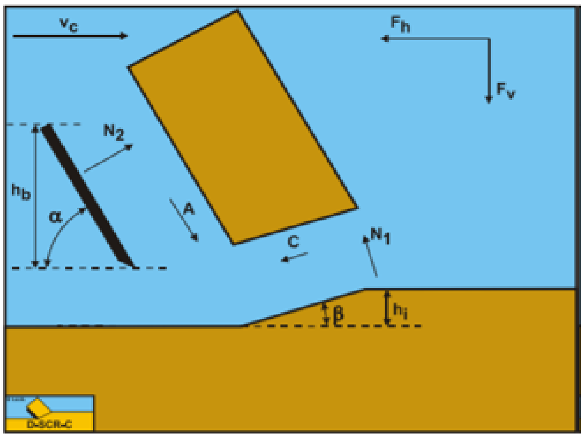

Figure 2-20: Forces on the layer of soil (Miedema, 2019).

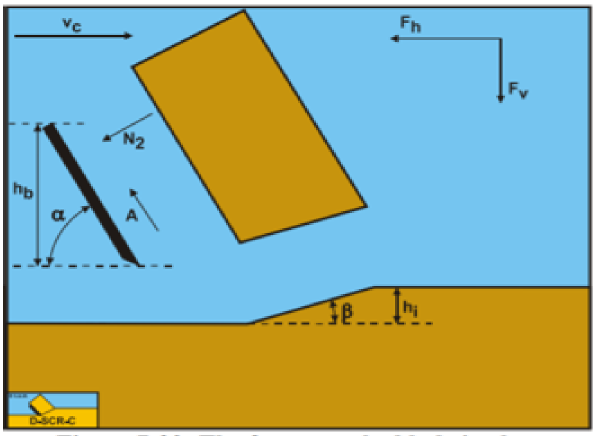

Figure 2-21: Forces acting on the blade (Miedema, 2019).

The following forces can be distinguished:

- N_1 is the normal force acting on the shear surface and N_2 is a normal force to the blade
- C is a shear force as a result of pure cohesion τ_c
- A is a shear force as a result of pure adhesion between the soil and the blade τ_a

During the cutting of clay, undrained conditions are assumed and the $\phi = 0$ concept is valid. Not only the internal friction angle can be considered zero, the same applies to the external friction angle because of high strain and deformation rates that are present. Additionally, gravity and inertia are neglected, since cohesive and/or adhesive forces play a dominant role.

From the horizontal and vertical equilibrium of forces, the forces from Figures 2-20 and 2-21 can be derived.

$$N_1 = \frac{-C \cdot \cos(\alpha + \beta) + A}{\sin(\alpha + \beta)} \tag{2.40}$$

$$N_2 = \frac{C - A \cdot \cos(\alpha + \beta)}{\sin(\alpha + \beta)} \tag{2.41}$$

In which α is the blade angle and β is the angle of the shear plane with the direction of the cutting velocity.

In the relations for the cohesive force C and the adhesive force A an average value for the strain rate factor is introduced. This factor usually equals $\lambda_s = 2$. This is done because the separate strain rate factors for the cohesive and adhesive force are almost identical.

$$C = \frac{\lambda_s \cdot c \cdot h_i \cdot w}{\sin(\beta)} \tag{2.42}$$

$$A = \frac{\lambda_s \cdot a \cdot h_b \cdot w}{\sin(\alpha)} \tag{2.43}$$

In which a and c stand for the adhesion and cohesion, respectively. h_i is the layer thickness of the clay, h_b is the blade height and w is the blade width. The four parameters mentioned here are related to each other by means of the ac-ratio r_{ac}:

$$r_{ac} = \frac{a \cdot h_b}{c \cdot h_i} \tag{2.44}$$

The amount of energy, that has to be added to a volume unit of soil to excavate it is called the specific cutting energy E_{sp}.

$$ESP = \lambda_s \cdot c \cdot \lambda_{HF} \tag{2.45}$$

In which λ_{HF} is the horizontal cutting force coefficient for the Flow Type and is defined as:

$$\lambda_{HF} = \frac{\sin^2(\alpha) + r_{ac} \cdot \sin^2(\beta)}{\sin(\alpha + \beta) \cdot \sin(\alpha\,) \cdot \sin(\beta)} \tag{2.46}$$

Tear type

Normal forces and thus stresses can become negative and, in that way, exceed the tensile strength of the clay. The equations for the Flow type mentioned above do not take this into consideration, since plastic shear failure is assumed. When the tensile strength is exceeded, tensile failure will occur, as depicted in Figure 2-19 This process roughly corresponds to the process of cutting artificial clays, which are brittle due to addition of cement to a natural clay (see Section 2.1.5). Brittle failure gives the following forces for the Tear Type:

$$F_h = \lambda_s \cdot \sigma_t \cdot h_i \cdot w \cdot r_T \cdot \frac{\lambda_{HT}}{r_T} \tag{2.47}$$

$$F_v = \lambda_s \cdot \sigma_t \cdot h_i \cdot w \cdot r_T \cdot \frac{\lambda_{VT}}{r_T} \tag{2.48}$$

In which F_h and F_v are the horizontal and vertical forces, respectively. Furthermore, σ_t is the tensile strength, r_T is the ratio adhesive force to tensile force and λ_{HT} and λ_{VT} stand for the horizontal and vertical cutting force coefficient for the Tear Type.

2.4 Slurry transport

A soil-water mixture is formed when clay is excavated by a SPRT in a pile. In order to remove this so-called slurry a conduit is positioned inside the tool. This pipe often covers the entire length of the tool; starting from the bottom where the slurry is trapped in the pile and going up all the way to the top of the tool where the slurry is discharged from the pile. This can only be done by creating a vacuum inside the pile (right under the suction pipe).

A vacuum refers to any space in which the pressure is much lower than the atmospheric pressure of $p_{atm} \approx 1\ bar$. This partial vacuum is thus created by displacing air. On Earth, this requires a barrel. Pumping air out of a sealed vessel i.e. submerged conduit in a SPRT (creating a vacuum in the vessel) reduces the pressure in the vessel. The more air that is pumped out of the vessel, the lower the pressure. The pressure in the vessel, which is lower than outside the vessel, is called a vacuum. When the pressure approaches zero, there is a maximum vacuum.

The application used for vertical slurry transport is suction, which basically is the creation of a vacuum in order to attract the slurry. In dredging practices often an airlift is used to create this suction. Another option is the usage of a centrifugal pump.

In most cases encountered however, especially in dredging practices, a centrifugal pump not self-priming. Prior to starting a centrifugal pump, it is possible that there is air in the casing of the pump. This will prevent correct operation of the pump. Once the pump is up and running it can operate with a vacuum (negative suction pressure on the suction side). This problem is not encountered with an airlift.

An airlift however cannot be used for system in which a limited hydraulic head is available. The force applied is insufficient to establish the required vacuum. This most definitely is the case in the scale tests that will be performed in this study. In general, the suction is always lower than de suction present in centrifugal pump. For example, it is relatively easy to establish a pressure of 10 bar. For an airlift this is much more difficult

2.4.1 Centrifugal pump

The Euler impulse moment equation is the first step in describing the performance of a centrifugal pump:

$$\Delta p_E = \rho_f \cdot u_0 \left(u_0 - \frac{Q \cdot \cot \beta_0}{2\pi \cdot r_0} \right) - \rho_f \cdot u_i \left(u_i - \frac{Q \cdot \cot \beta_i}{2\pi \cdot r_i} \right) \tag{2.49}$$

According to (Miedema, 2019), for a known pump this can be simplified to:

$$\Delta p_E = \rho_f \cdot (C_1 - C2 \cdot Q) \tag{2.50}$$

Due to inconsistencies encountered in impeller blades and flow, the finite number of blades, the blade thickness and the internal friction of the fluid; the Euler pressure Δp_E must be adjusted with a constant factor k, with a value of roughly 0.8. The efficiency of the pump however is not influenced by this factor. The resulting equation must be corrected for losses from:

- frictional contact with the walls and deflection and diversion → $\Delta p_{h,f}$
- inlet and impact → $\Delta p_{h,i}$

The pressure reduction due to frictional losses:

$$\Delta p_{h,f} = C_3 \cdot \rho_f \cdot Q^2 \tag{2.51}$$

Given a design flow Q_d the impact losses can be described with:

$$\Delta p_{h,i} = C_4 \cdot \rho_f \cdot (Q_d - Q)^2 \tag{2.52}$$

Therefore, the total head of the pump as a function of the flow:

$$\Delta p_p = k\Delta p_E - \Delta p_{h,f} - \Delta p_{h,i} \tag{2.53}$$

Substituting Equations (2.50), (2,51) and (2.52) now in Eq. (2.53) and rearranging gives the following relation for the total head of a centrifugal pump:

$$\Delta p_p = \rho_f \cdot [k(C_1 - C_2 \cdot Q) - C_3 \cdot Q^2 - C_4 \cdot (Q_d - Q)^2] \tag{2.54}$$

In which C_1, C_2, C_3 and C_4 are pump coefficients. The fluid density ρ_f in the pump can be either the density of a homogeneous fluid (for water ρ_w) or the density of a mixture ρ_m passing the pump; The latter is holds true in case of the transport of soil-water mixtures (i.e. slurries) during pile dredging.

The total efficiency of the pump can now be determined by dividing the power that is added to the flow $P_f = \Delta p_p \cdot Q$ by the power that is output of the (diesel) engine $P_e = k \cdot \Delta p_E \cdot Q + P_{fr}$(in which P_{fr} is the power required for the frictional losses in the gear box, the pump bearings, etc.), this gives:

$$\eta_p = \frac{k \cdot \Delta p_E - \Delta p_{h,f} - \Delta p_{h,i}}{k \cdot \Delta p_E \cdot Q + P_{fr}} \tag{2.55}$$

2.4.2 Airlift

Another way to establish a pumping operation in submerged environments is by implementing an airlift. A conventional airlift pump configuration is illustrated in Figure 25. At the base of the depicted riser tube a gas, typically air, is injected. The resulting gas bubbles that arise will be in suspension in the fluid (for convenience water is assumed throughout the text); this will have an effect on the average density of the two-phase mixture in the tube. This density will become smaller than the density of the surrounding fluid. Hence, a buoyant force is developed that will result in pumping process.

Most widely encountered in airlift pump operations is the slug flow regime. This regime is characterised by its large bubbles that have the capacity to nearly span the riser tube. The length of the bubbles ranges from roughly the diameter of the tube, to several times this value. The space in-between the bubbles is mostly filled with liquid as mentioned in (Govier & Aziz, 1972) and denoted as the liquid slug. The large gas bubbles that can be seen in Figure 2-22 are referred to as gas slug or Taylor bubble. For a better understanding the distinction between bubble flow and slug flow is illustrated in Figure 2-23.

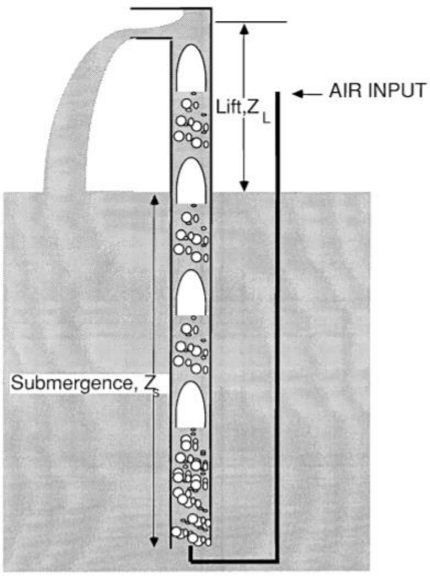

Figure 2-22: Airlift pump (Reinemann & Timmons, 1987)

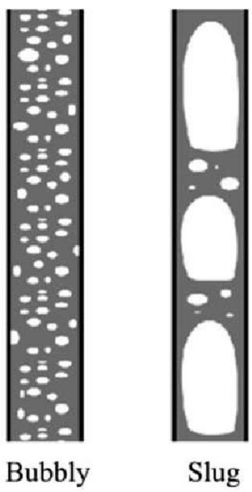

Figure 2-23: A diagram showing the classification of gas-liquid flow regimes mostly encountered in airlifts (Ambrose, 2015).

A lot of research is done on the working principles of airlift pumps throughout the years; both experimental and theoretical. Here, an emphasis is placed on the theory behind airlift pumps in the slug flow regime.

The rise velocity of a gas slug in a vertical tube relative to a moving liquid slug is given as

$$v_t = c_0 \cdot v_m + v_{ts} \tag{2.56}$$

In which v_t is the rise velocity of the Taylor bubble, v_{ts} is the rise velocity of the Taylor bubble in still fluid, c_0 is the liquid slug velocity profile coefficient and v_m is the mean velocity of the liquid slug, given by:

$$v_m = \frac{Q_1 + Q_g}{A} \tag{2.57}$$

In which Q_1 is the volumetric liquid flow rate, Q_g is the volumetric gas flow rate and A is the tube cross sectional area.

Following the analysis implemented by (Nicklin, 1963) the velocity of the Taylor bubble is set equal to the average linear velocity of the gas in the riser tube:

$$v_t = \frac{Q_g}{\epsilon A} \tag{2.58}$$

In which ϵ is the gas void ratio.

The submergence ratio α is a parameter commonly found in airlift analysis and is defined as:

$$\alpha = \frac{Z_S}{Z_L + Z_S} \tag{2.59}$$

In which Z_L is the lift height and Z_S is the length of the submerged tube (see Figure 25). The submergence ratio is equal to the average pressure gradient along the riser tube which is made up of components due to the weight of the two-phase mixture and frictional losses. Performing a static pressure balance on a vertical tube which is submerged in fluid it follows that:

$$\rho \cdot g \cdot Z_s = \rho \cdot g \cdot (1 - \epsilon) \cdot (Z_s + Z_1) \tag{2.60}$$

Thus, the weight of the gas is negligible relative to the weight of the liquid. If the fluid in the tube is moving, an additional pressure drop due to frictional losses must be added to the right-hand side of Eq. (2.60). The single-phase frictional pressure drop can be calculated based upon the mean slug velocity as:

$$p_s = f \cdot \frac{(Z_s + Z_1)}{2D} \cdot \rho v_m^2 \tag{2.61}$$

In which ρ_s is the single-phase frictional pressure drop, D is the diameter of the tube and f is friction factor by (Giles, 1962), $f = 0.316/Re^{0.25}$.

The single-phase frictional loss must then be multiplied by $(1 - \epsilon)$, the fraction of the tube occupied by the liquid slugs, to obtain the total frictional pressure drop in the riser tube.

It is usual to define the efficiency of the airlift pump as the net work done in lifting the liquid, divided by the work done by the isothermal expansion of the air (Nicklin, 1963):

$$\eta = \frac{Q_1 \cdot Z_1 \cdot \rho \cdot g}{Q_g \cdot P_a \cdot \ln(p_0/p_{atm})} \tag{2.62}$$

Where p_{atm} is the atmospheric pressure and p_0 is the pressure at base of the riser tube.

2.5 Scaling theory

A model is developed in order to predict the excavation production of a SPRT. Measurements are performed on a small model and scaling laws are used to convert and predict the magnitude of numerous variables on the full-scale prototype SPRT. In general, this prototype is more expensive than a small-scale model. By using scaling theory, a cheap way is found to model design information for a prototype while keeping costs relatively low.

2.5.1 Scaling factors

A scale model is produced by scaling down an actual situation i.e., prototype without deviating too much from the original situation i.e., model. This can only be achieved if the corresponding dimensions and physics involved in the model and prototype exhibit similarity. Instead of complete similarity (White, 2011) speaks of three distinct types of similarity:

1. Geometric similarity: a model and prototype are geometrically similar if and only if all body dimensions in all three coordinates have the same linear scale ratio.
2. Kinematic similarity: the motions of two systems are kinematically similar if velocities and accelerations are in constant ratio at all geometrically equivalent points
3. Dynamic similarity: a model and prototype are dynamically similar exists if and only if the length scale ratio, time scale ratio, and force scale (or mass scale) ratio are the same

Once geometric similarity is satisfied, dynamic and kinematic similarity will exist simultaneously if the pressure and force coefficients of the model and prototype are the same. This is ensured by applying scaling rules defined for several physical processes and dimensions that are present in the prototype. Subsequently scaling factors can be introduced. A scale factor is defined as the ratio between a parameter in the model and the protype.

$$n_x = \frac{x_p}{x_m} \tag{2.63}$$

In which n_x is the scaling factor of a parameter x and x_p and x_m are the values of the parameter x in the prototype and the model, respectively. As mentioned above, a scaling factor will only hold true if it meets certain rules. The following three scaling rules are mentioned by (van der Schrieck & van Rhee, 2010):

1. Scale of the product of two parameters = product of the scales of two parameters.
2. Scale of the sum of two parameters = scale of one of the two parameters. This only holds if the scale of the two parameters is equal; scaling effects will occur if not.
3. Scaling factor of a constant is equal to unity.

2.5.2 Dimensionless parameters

For most fluid mechanics problems, it is important to preserve dynamic similarity, as was discussed in subsection 2.5.1. Dynamic similarity can be reached by implementing the dimensional homogeneity. This concept is based on a constant relation between parameters in both prototype and model and is often presented as a dimensionless indicator i.e., dimensionless parameter.

These parameters can be obtained from the Navier-Stokes equations that describe the motion of a fluid. For almost all types of fluid flow these formulas contain nonlinear partial differential equations. These equations can be simplified to linear equations for a limited number of cases, in which certain theoretical boundary and kinematic conditions need to be satisfied

Various dimensionless flow parameters can be defined when approaching this problem with the Navier-Stokes equations (Cengel, 2006). First, the momentum equation in x-direction is defined:

$$\rho \cdot g - \frac{\partial p}{\partial x} + \mu \cdot \left(\frac{\partial^2 u}{\partial x^2} + \frac{\partial^2 u}{\partial y^2} + \frac{\partial^2 u}{\partial z^2}\right) = \rho \cdot \left(\frac{\partial u}{\partial t} + (u\frac{\partial u}{\partial x} + v\frac{\partial u}{\partial y} + w\frac{\partial u}{\partial z})\right) \tag{2.64}$$

In which μ is the dynamic viscosity of the fluid. The first term in Eq. (2.64) represents the gravity component in x-direction. The second term represents the pressure gradient in x-direction. The third term describes the change in velocity component in x-direction in x-, y- and z-direction, respectively. The fourth term equals the change of velocity over time in x-direction.

The Navier-Stokes equation from Eq. (2.64) is then normalized by introducing the following scaling parameters: L for length, U for velocity, T for time and P for pressure. The gravity g is assumed to be the only external force present. This leads to the following dimensionless parameters:

$$U_d = \frac{u}{U}, \quad t_d = \frac{t}{T} \quad p_d = \frac{p}{P} \quad g_d = \frac{g}{g_0}, \quad \nabla_d = L \cdot \nabla, \quad \nabla_d^2 = L^2 \cdot \nabla^2 \tag{2.65}$$

Where $\nabla = \left(\frac{\partial^2}{\partial x^2} + \frac{\partial^2}{\partial y^2} + \frac{\partial^2}{\partial z^2}\right)$

Now, the dimensionless parameters of Eq. (2.65) are substituted into Eq. (2.64) and divided by $\rho \cdot U^2 \cdot L^{-1}$. After some rearrangement, the nondimensional form of the Navier-Stokes equation is produced:

$$\left(\frac{gL}{U^2}\right) \cdot g_d - \left(\frac{P}{\rho U^2}\right) \cdot \nabla_d \cdot p_d + \left(\frac{\eta}{\rho L U^2}\right) \nabla_d^2 \cdot u_d = \left(\frac{L}{UT}\right) \cdot \frac{\partial u_d}{\partial t} \tag{2.66}$$

Clearly, four dimensionless numbers can be seen in In Eq. (2.66). These dimensionless numbers are in fact the dimensionless flow parameters that were searched for:

$\left(\frac{g*L}{U^2}\right) = Fr^{-1}$ **Froude number**; the ratio between gravitational and inertial forces in a fluid. Is used to maintain similarity for gravitational driven flows, such as free surface flow.

$\left(\frac{P}{\rho_f * U^2}\right) = Eu^{-1}$ **Euler number**; the ratio between the pressure drop and kinetic energy. The Euler number is used to characterize losses in a flow due to a pressure drop.

$\left(\frac{\eta}{\rho_f * L * U^2}\right) = Re^{-1}$ **Reynolds number**; the ratio between the viscous and inertial forces in a fluid. The Reynolds number is used to characterise flow regimes (laminar/turbulent), which can be divided by the importance of the viscous and inertia forces for a specific regime, such as in fully enclosed (pipe) flows.

$\left(\frac{L}{U * T}\right) = St^{-1}$ **Strouhal number**; a measure for the occurrence of vortex shedding. An equal Strouhal number means the frequency of separation of the boundary layer is similar on both situations.

What really stands out from this derivation is that all dimensionless flow parameters here have a fixed relation between length L, velocity U and density ρ. In short, it is nearly impossible to maintain similarity for all parameters at the same time. The consequence is that deviations are formed in the model will in comparison to the ideal scaling situation. These deviations are called scaling effects.

To maintain dynamic similarity under the influence of the forces of gravity and inertia as is the case in this study, the Froude number will be further elaborated upon.

$$Fr^2 = \frac{u^2}{gL} \tag{2.67}$$

In which Fr is the Froude number, u is the fluid velocity and g is the gravitational acceleration and u is the fluid velocity. Dynamic similarity is thus achieved when $n_{Fr} = 1$. The model that is used in this study is therefore called a *Froude scale model*. Since gravity can be assumed constant, the scaling rule for velocity is given as:

$$n_u = \sqrt{n_g \cdot n_L} = \sqrt{n_L} \tag{2.68}$$

2.5.3 Scaled parameters

The parameters that need to be scaled are discussed in sections prior to this one. The scaling factors that are affiliated with those parameters are considered here.

Pile diameter
The pile diameter scales according to the length scale:

$$n_D = n_L \tag{2.69}$$

Jet exit velocity and jet pressure
The exit velocity of the jet has scales according to the velocity scale:

$$n_{u_0} = n_u = \sqrt{n_L} \tag{2.70}$$

The jet pressure (pressure drop over the nozzle) is proportionally related to the exit velocity and fluid density. The fluid that will be used in the experiments is fresh water, compared to salt water that is encountered in practice. This will lead to a scale effect. The effect that this difference in density has on the overall process of hydraulic excavation is assumed to be negligible. The fluid density i.e., density of the (fresh water) is therefore assumed to be constant, resulting in a scaling factor of $n_{\rho_w} = 1$. The scaling rule for the jet pressure is then formulated as:

$$n_{p_j} = n_{u_0}^2 \cdot n_{\rho_w} = n_{u_0}^2 = n_L \tag{2.71}$$

The same scaling rule holds true for the stagnation pressure.

Discharge through the nozzle
The discharge is the product of the exit velocity and the nozzle area, resulting in:

$$n_{Q_0} = n_u \cdot n_L^2 = n_L^{5/2} \tag{2.72}$$

Turbulence
As mentioned in Section 2.5.2, the Reynolds number is an indication of turbulence. Assuming a constant value for the kinematic viscosity $n_v = 1$, the scaling rule for the initiation of turbulence is:

$$n_{Re} = \frac{n_u \cdot n_L}{n_v} = n_u \cdot n_L = n_L^{3/2} \tag{2.73}$$

This scaling rule gives rise to a scale effect that has a great influence on the process, if not dealt with properly. The scale effect of $1/n_L^{3/2}$ for Reynolds implies that the turbulence is underestimated in the model. When choosing the final scale that will be applied in this study, this should be taken into account. The protype situation always assumes turbulent flow, therefore it is of importance to retain the turbulent regime for the model. This is especially the case when working with low pressure jets. Turbulent flow is achieved at $Re > 2000$.

Nonetheless, it is important to note that even though model and prototype both are in the turbulent regime, this does not necessarily mean that mixing behaves identical. Turbulent fluctuations are different after all even if the flow regime is the same. It is assumed that if the difference in order of magnitude for the value of the Reynolds number is not larger than 10^2 and $Re \gg 2000$ the difference in turbulent fluctuations between prototype and model are negligible.

Jet Power
The power that a jet can produce is related to the pressure of the jet and the resulting discharge through the nozzle:

$$n_P = n_{p_j} \cdot n_{Q_0} = n_L \cdot n_L^{5/2} = n_L^{7/2} \tag{2.74}$$

Jet momentum flux
The characterization of a jet can be described by three jet flow parameters: mass flux, specific momentum flux and specific buoyancy flux (Fischer, 1979). The buoyancy flux implies that there is a difference between the density of the jet and the density of the ambient fluid. In this study, that is not the case and therefore the buoyancy flux is zero. The mass flux is nothing more than the jet discharge, which is already treated.

The specific momentum flux equals the jet momentum flux. This parameter is important for relating the low-pressure jets to the high pressure jets. Although lots of other variables are altered during experiments; this parameter should be kept constant throughout the whole process. Without it, it would be impossible to make a proper comparison between jet pressure regimes under the same circumstances.

The jet momentum flux at the nozzle exit I_0 can be scaled in the following manner:

$$n_{I_0} = n_{\rho_w} \cdot n_{Q_0} \cdot n_{u_0} = n_L^{5/2} \cdot \sqrt{n_L} = n_L^3 \tag{2.75}$$

Rotational speed

The rotational speed of the tool expressed in Rounds Per Minute (RPM) has a scale factor n_n that is equal to the scale factor of the angular velocity n_ω. The angular velocity is a function of time.

$$n_t = \frac{n_L}{n_u} = \frac{n_L}{\sqrt{n_L}} = \sqrt{n_L} \tag{2.76}$$

In which n_t is the scale factor for time. This leads to the following scaling rule for rotational speed:

$$n_n = n_\omega = \frac{1}{n_t} = \frac{1}{\sqrt{n_L}} \tag{2.77}$$

This would imply that the rotational speed is overestimated in the model. Rotational speeds in the model therefore need to be larger than the ones encountered in the prototype. This should be looked at when selecting the desired scale, although the scale effect of $\sqrt{n_L}$ is quantitively smaller in an absolute sense than the one encountered for turbulence. Moreover, the minor contribution of this parameter to the overall physical processes that take place during the experiments is worth mentioning.

Undrained shear strength

Conceptually, there is no such thing as the undrained shear strength. Nevertheless, a definition is given (see Section 2.1.3) that describes this parameter as the magnitude of the shear stress that a soil can sustain before it fails. Thus, the undrained shear strength s_u scales as a stress. A stress is formulated as the ratio between a force and an area on which the force is applied, in which a force is mass times acceleration in accordance with Newton’s second law.

$$n_F = n_m \cdot n_a = n_m = n_{\rho_w} \cdot n_L^3 = n_L^3 \tag{2.78}$$

Because of the definition of acceleration being the ratio of the velocity and time and both these parameters are equal in Froude scaling, the scale factor automatically becomes 1. This leads to the scaling rule for the undrained shear strength:

$$n_{s_u} = \frac{n_F}{n_A} = \frac{n_L^3}{n_L^2} = n_L \tag{2.79}$$

Specific Energy

In cohesive soils like clay, the specific energy for jetting (Joules per suspended soil volume $[J/m^3]$) is an order of magnitude higher than for cutting. Specific energy is formulated as the ratio of jet power to jet discharge.

$$n_{ESP} = \frac{n_P}{n_{Q_0}} = \frac{n_L^{7/2}}{n_L^{5/2}} = n_L \tag{2.80}$$

Cavity depth

As mentioned before in the theory (see Eq. 2.35) the cavity depth Z_c for non-cavitating jets must scale with the nozzle diameter D_n and the ratio p_j/s_u. It is however not necessary to derive a separate scaling factor for this parameter. The expected relation is automatically achieved by implementing a Froude scaling scenario, as was done in this study.

Combining Eq. 2.71 and Eq. 2.79 will lead to:

$$n_{Z_c} = \frac{n_{D_n} \cdot n_{P_j}}{n_{s_u}} = \frac{n_L \cdot n_L}{n_L} = n_L \tag{2.81}$$

This shows that the derived scale factor indeed scales with the initially chosen length scale.

3 Experimental setup

3.1 Introduction

This chapter aims to give a thorough overview of all the components that make up the test setup that are required for this study. Two test setups are designed that will incorporate all the features of the available tools, as mentioned in the introduction to this report (see Table 1-1). All four tools mentioned here, will be further elaborated upon in Section 3.2. Several scale tests need to be done in order to get a better understanding of the performance of the available SPRT's. The applied scaling is discussed in Section 3.3 and the model setup is described in Section 3.4. Section 3.5 introduces the selected artificial clay. Lastly, in Section 3.6, prior to the main experiments, some preliminary experiments were carried out in the lab to get acquainted with equipment and procedures.

3.2 Available tools

This study focusses on a design assignment in which several scale tests need to be done in order to get a better understanding of the performance of the available SPRT's and their specific advantages /disadvantages over each other. For this, three specific SPRT's will be examined that are manufactured by the leading companies in the pile dredging industry (Deep C, Deco and Claxton) and an in-house tool from Boskalis. An overview of all relevant parameters of each tool is given in Table 3-1. Not all parameters were provided by the suppliers. These missing parameters were estimated according to the parameters that were present using the hydraulic jetting equations presented in Section 2.2.

Table 3-1: Key parameters of the available tools

Parameter	Symbol	Boskalis	Deco	Deep C	Claxton	Unit
Hydraulic power	P_{hyd}					kW
Jet pressure	p_j					bar
Jet flow	Q_j					l/min
Jet momentum flux	I_j					N
Airlift diameter	D_a					mm
Nozzle diameter	D_n					mm

3.2.1 Boskalis Airlift (*Boskalis*)

This is the only SPRT out of the available tools that is based on a low-pressure pump system. The airlift tool was initially used for the Viking & Vulcan project and has multiple sections of $8\ m$ with flanged connections. The supply lines are two times 5" jet water supply and a single 4" air pressure supply. An 8" centralized line will transport the resulting clay-water mixture upwards. Underneath the airlift the last section has a jet layout where 8 nozzles are located for loosening the soil. This tool can only operate static (jetting head cannot rotate).

3.2.2 Onslow dredging tool *(Deco)*

This SPRT is able to excavate non-cohesive material (i.e. sand and gravel) as well as soft to extremely high strength clay layers. Because of the required ability to dredge high strength clays, the tool is equipped with clay dredging capabilities. The SPRT is clamped inside the pile while a series of ultra-high-pressure water jets (2 times 1000 bar) that will cut and break up the high strength clay layers. Next to the ability of the jetting head to rotate, the individual nozzles are additionally able to move separately to cover the complete soil surface inside the piles. This feature is only incorporated in this specific tool; other tools contain only fixed nozzles (either facing downwards or placed under an angle).

The suspension that arises after jet impingement will be transported using a 12” airlift incorporated in the tool. The jets can also be inclined towards the pile wall to clean it while dredging. The complete layout of the tool is shown in Figure 3-1

Figure 3-1: Deco tool hanging in a vessel crane prior to deployment

3.2.3 Deep C® SPRT 3000 *(Deep C)*

This SPRT is designed for both removal of soil plugs and cleaning of piles. The tool has a deployment system on the pile and integrated level control independent of vessels cranes. A high-pressure rotating water jetting system is applied with a (project) specific number of nozzles for soil loosening. There is one 12” supply line available for jet water supply. Furthermore, a pumping unit with a 12’’ suction head is supplied for removal of the developing mixture inside the pile.

This SPRT is operated via a launch-frame (catcher) placed standing on top of the pile to accurately and safely handle the operation of the SPRT in and out of the pile. The SPRT with the subsea launch and recovery (L&R) frame is transferred from deck to pile in one lift. After the frame is installed, no use of a vessel crane is necessary. Figure 3-2 shows the SPRT in question hanging from a vessel crane prior to subsea transfer. The tool however can also be deployed in the conventional way using a vessel crane throughout the entire pile dredging operation.

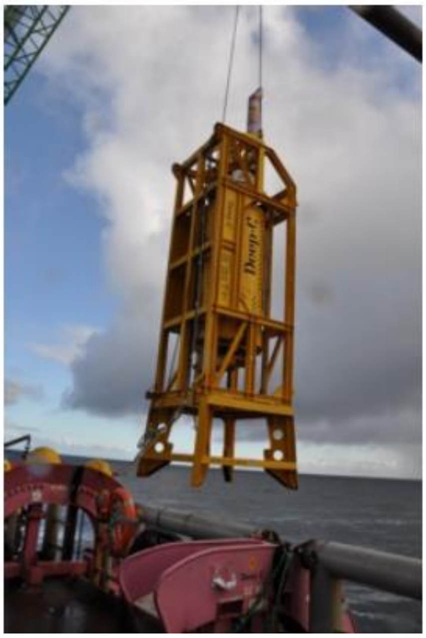

Figure 3-2: Deep C SPRT deployed by L&R frame.

3.2.4 Claxton SPRT *(Claxton)*

The high-pressure water jetting and air lift system of the Claxton SPRT is based on the principal of downward and angled high pressure jets within a head which shall break up the soil and fluidise it. An airlift system extracts the loosened material and transports it up a central pipe that is connected to a (flexi) hose which then connects to an elbow section above the pile catcher. The elbow section is supported by buoyancy (deployed on its own rigging). The soil is then ejected from the outlet mid-water.

Similar to the tool discussed in Section 3.2.3, this SPRT also makes use of a submerged operating frame. This so-called pile catcher / hang-off frame is being deployed and landed on the top of the pile. In this case, different to the L&R frame, the SPRT is now hang from winches that control the descent of the SPRT as it excavates and removes the soil plug. The pile catcher holds the SPRT and provides a locking mechanism designed to secure the tooling during transport and lifting.

The tool incorporates 36 nozzles divided equally over four quarters at the base plate. The jet water is supplied by two $3/4''$ jetting lines. Internal setup of the air lift consists of a central opening of $8''$ at the base plate, leading into this are 4 channels that will help pull in outlying soil and prevent blockages

3.3 Scaling

In choosing the final scale that will be applied during the experiments the various occurring scale effects should be limited to some extent. In this study the diameter of the offshore pile and dimensions related to the SPRT are leading.

This led to a **scale of $\mathbf{1:5}$**. This scale is considered to dimensionally maximise the experimental setup in such a way that experiments can relatively be performed with ease while at the same time also be able to narrow down scale effects.

The values that will be applied in the experimental test setup can now be determined by the scaling factors from Section 2.5. An overview of all relevant jet parameters is given in Table 3-2; soil parameters are included as well.

It has been decided to perform the jetting tests for three jet pressure regimes:

1. Low Pressure (LP) $p_j = 3\ bar$
2. Medium Pressure (MP) $p_j = 30\ bar$
3. High Pressure (HP) $p_j = 130\ bar$

The abbreviations LP, MP and HP will be used from this point on to distinguish between the three selected jetting pressure regimes.

Table 3-2: Scaled values of characteristic parameters

Parameter	Symbol	Prototype value(s)	Model value(s)	Unit
$Pile\ diameter$	D	1500	300	mm
$Jet\ pressure$	p_j	20, 150, 650	3, 30, 130	bar
$Jet\ discharge$	Q_0	3007,849,458	54, 15, 8	l/min
$Nozzle\ diameter$	D_n	2.5, 5.0, 11.5	0.5, 1.0, 2.3	mm
$Jet\ Power$	P_0	84, 252, 559	0.3, 0.9, 2.0	kW
$Stand\ off\ distance$	SOD	$0 - 150D_n$	$0 - 30D_n$	$-$
$Jet\ momentum\ flux$	I_0	~ 2375	~ 19	N
$Airlift\ diameter$	D_a	170	34	mm
$Airlift\ discharge$	Q_a	$3000 - 4600$	$50 - 80$	l/min
$Rotational\ speed$	n	0.4, 0.7, 0.9	1, 1.5, 2	rpm
$Undrained\ shear\ strength$	s_u	100, 300, 500	20, 60, 100	kPa

The prototype values are based on the values given in Table 3-1 for the available industry manufactured soil plug removal tools. These values do not correspond exact with the values as given here. The values included in Table 3-1 are intended to serve as a guideline for the range in which prototype numbers should fit. This can clearly be seen when examining the parameters listed here (the values do not deviate that much from each other).

The relevant physics are also scaled according to the aforementioned method and displayed in Table 3-3.

Table 3-3: Scaled physics for Low Pressure (LP), Medium Pressure (MP) and High Pressure (HP) systems

System	Parameter	Symbol	Prototype value(s)	Model value(s)	Unit
Jet	$Reynolds\ number, LP$	Re_{LP}	$2.5E+06$	$2.3E+05,$	$-$
	$Reynolds\ number, MP$	Re_{MP}	$1.4E+06$	$1.3E+05,$	$-$
	$Reynolds\ number, HP$	Re_{HP}	$4.5E+05$	$4.0E+04$	$-$
	$Froude\ number, LP$	Fr_{LP}	101	101	$-$
	$Froude\ number, MP$	Fr_{MP}	452	452	$-$
	$Froude\ number, HP$	Fr_{HP}	4515	4515	$-$
$Airlift$	$Reynolds\ number$	Re_a	$3.7 - 5.8(E+05)$	$3.3 - 5.1(E+04)$	$-$

Application of Froude scaling implies that the Froude number is kept constant. Consequently, the turbulence indicator i.e. Reynolds number, must have a scale effect. An implication of this is that turbulence is underestimated. Given the scale of $1:5$ used in this study and the scale effect of ${n_L}^{3/2}$

for turbulence, the Reynolds number for the model is approximately 11 times smaller than the one for the prototype. Both can be observed in the resulting calculations performed using the scaling factors.

Another important matter is retaining the turbulent regime for the model. Adding the fact that for both prototype as model $Re \gg 2000$ (way outside the laminar region and even the transitional region between laminar and turbulent flow) difference in turbulent fluctuations can be assumed negligible in this study. This holds true for both the jet as the airlift (taken right under the exit of the airlift).

3.4 Test setup

This section will focus on the test setup and the corresponding equipment, materials and sensors.

3.4.1 Soil Plug Removal Tool

The SPRT that is used during the scale tests is designed in the 3D CAD program *SolidWorks*. The tool is entirely made of structural steel. It can be divided in two main components:

1. Jetting tool
2. Centre frame

The jetting tool consists of a shaft and jetting head. The shaft is used to bridge the distance from the starting point to the bottom of the pile and is connected to the head. The head contains the nozzles that are used in the hydraulic excavation process. It also contains an opening in the middle through which a conduit is run all the way up to the top of the shaft. A drawing of the jetting tool is given Figure 3-3; Figure 3-4 shows the centre frame.

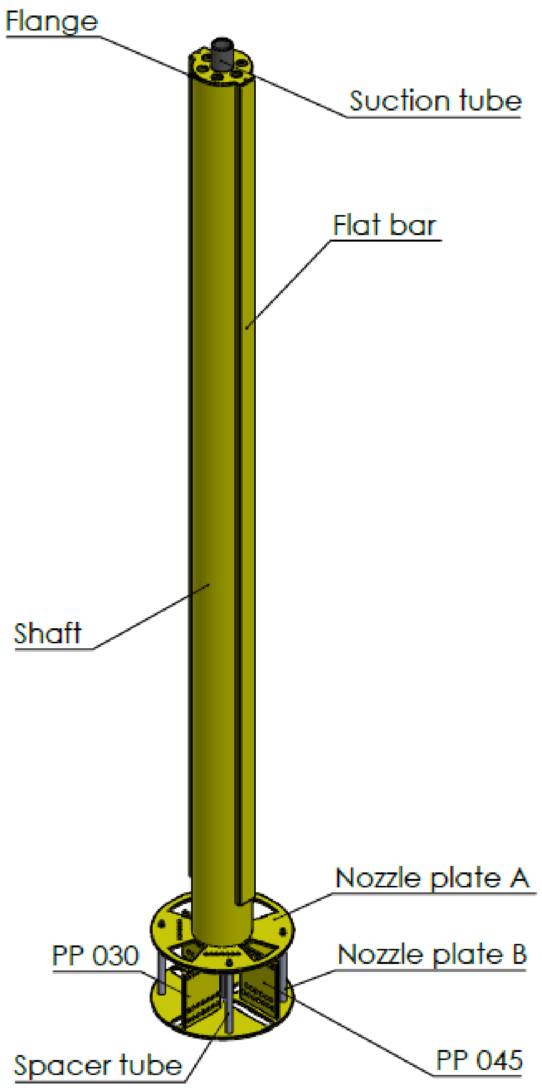

Figure 3-3: Self designed jetting tool and its components

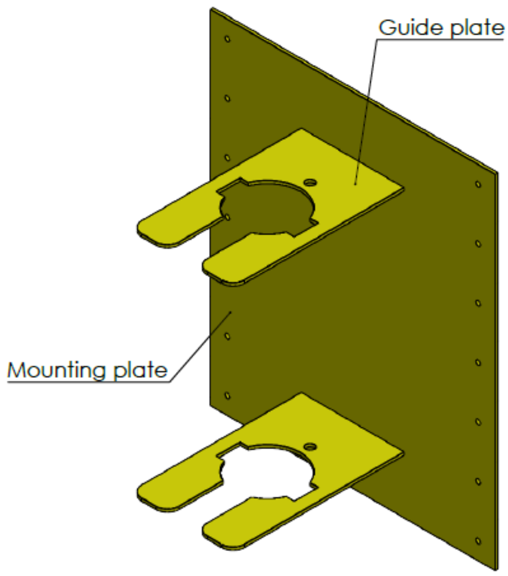

Figure 3-4: Centre frame

The jetting tool consists of a $2000\ mm$ long shaft. A flange is mounted on the top of the tool. This flange contains a hole with a dimeter of $42\ mm$ through which a PVC suction pipe with an outer diameter of $40\ mm$ will pass and eventually will exit at the bottom until it reaches Nozzle plate B. This suction pipe must have a minimum inner diameter of $30\ mm$ according to the scaling scenario. This lower boundary must be increased in practice, as was described above, therefore a suction inlet of $1.35"$ is proposed, roughly $34\ mm$.

The tool is placed inside the two guide plates of the centre frame during testing. The centre frame has two functions. The first function is to centralize the tool inside the pile; the second function is to prevent the tool from rotating. For this reason, two flat bars are welded to both sides of the shaft to ensure that the tool can safely slide up and down while maintaining torsional rigidity (i.e. the resistance to rotate). The flat bars have a rectangular profile and a length of $1900\ mm$. The flat bars do not span the entire length of the shaft. This design decision is made to guarantee sufficient room for the jet water distribution system that will be mounted on the tool. This system is required to transport water from a water supply source to the nozzles which are located at the end of the line. In this case, the end of the line is located at the jetting head, see Figure 3-5 for the 3D drawing and Figure 3-6 for the manufactured jetting head to which the jet water distribution system is added including the nozzle mountings that pass through the slots in Nozzle plate B.

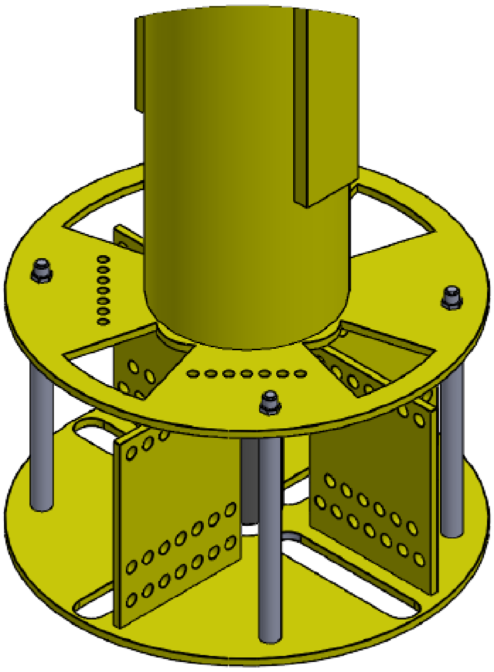

Figure 3-5: 3D drawing of jetting head

Figure 3-6: Actual jetting head with jet water distribution system (hoses + nozzle mountings)

The different pile dredging companies use a multitude of pile diameter over tool diameters ratios. For this experiment, the diameter of the nozzle plates (A and B) is set to be as large as possible for practical reasons. This led to a tool diameter of $270\ mm$. Nozzle plate A is directly connected to the shaft. It contains four large openings through which parts of the jet water distribution system can pass. It is connected to the bottom plate (Nozzle plate B) by making use of four spacer tubes. Threated rods pass through these tubes and are bolted at both sides to make sure that the bottom plate is thoroughly secured. This firm connection however can easily be removed in order to perform maintenance works for example.

Nozzle plate B features four Perforated Plates (PP), which are divided over the circumference (i.e. 90 degrees apart). Specific tube clamps can be attached to these plates making use of the perforated configuration present. All plates ensure a vertical orientation for the tube clamps. Nevertheless, it is also possible to achieve an inclined orientation of $30\ °$ and $45\ °$ from the vertical for PP-030 and PP-045, respectively. The hoses that are fixed in these tube clamps are the ones that contain the nozzles. Each Perforated Plate has a slot next to it that serves as an opening through which jet water from the nozzle exit can pass onto the soil underneath the bottom plate. A hole with a diameter of $34\ mm$ is located at the centre of Nozzle plate B; this diameter is equal to the inner diameter of the suction pipe, ensuring the suction pipe to rest on top of the bottom plate.

The initial idea was to construct a modular tool; that is a tool in which the size of the tool can be altered by either increasing or reducing the diameter. Instead of actually changing the diameter of the tool shaft for different experiments, the same principle is achieved by moving the jets through the slots from an inner position close to the shaft and to a maximum outer position of $60\ mm$.

3.4.2 Equipment

The experiments were carried out in the dredging laboratory located at the faculty 3mE in Delft. A schematic overview of the complete test setup is given in Figure 3-7.

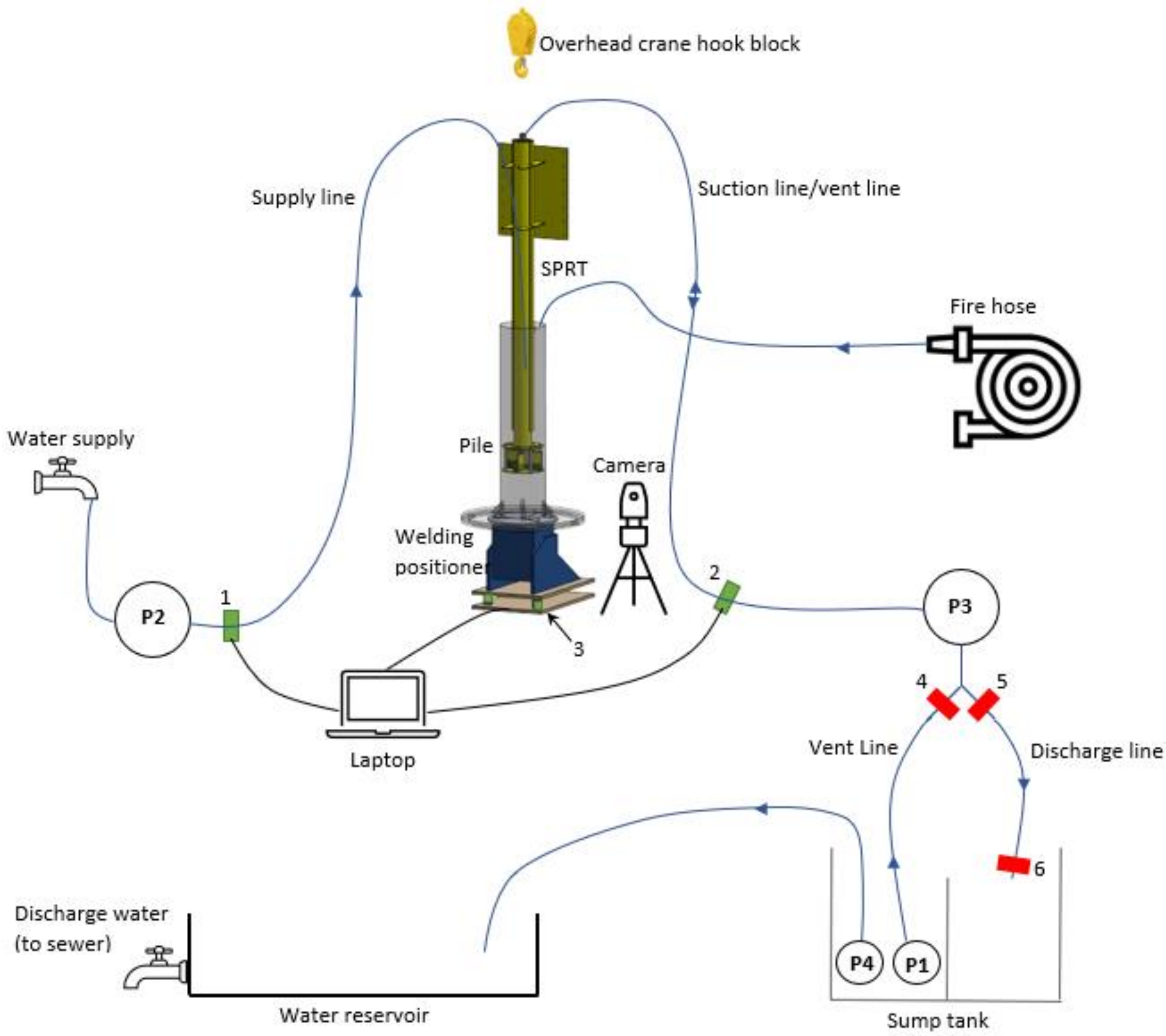

Figure 3-7: Schematic overview of the test setup

The numbers assigned in Figure 3-7 belong to different sensors (green rectangles) and valves (red rectangles). A total of four pumps will be used during the experiments; they are represented here by a circle in which the letter *P* is followed by a number. All components, not already mentioned in the figure, are listed in Table 3-4.

See Appendix A for the actual laboratory test setup in which the process is described chronologically making use of photos taken during the experiments.

Table 3-4: numbered components from Figure 3-8

Number	Sensor/valve		Pump number	Pump name
1	Pressure sensor		P1	Small Submersible Pump (SSP)
2	Flow sensor		P2	Supply Pump (SP)
3	Loadcell (x3)		P3	Dredge pump (DP)
4	SSP ball valve		P4	Large Submersible Pump (LSP)
5	DP ball valve			
6	Gate valve			

All components that make up the test setup, as depicted in Figure 3-7, are further elaborated upon in this subsection.

Welding positioner - rotation
Two out of the four available tools use rotating jets, i.e. a rotating head configuration as seen in Table 1-1. In dredging practice only the bottom part of the tool, the part where the nozzles are located, rotates. For the experiments performed in this study, it is challenging to implement the same system and mechanisms without constructing a very complex (e.g. waterproof inner part) and expensive tool. Another option is to rotate the complete tool from the top, eliminating placing electronic parts inside the tool shaft. Nonetheless, this option is limited to a $180°$ rotation. A full rotation will most certainly damage the supply lines and therefore its connections.

A more discrete way of achieving the same principle, namely rotating jets, is by rotating the pile instead. A welding positioner with a rotary table is proposed that is able to withstand the weight of the pile (assembly) and its contents at full capacity, roughly $150\ kg$. An additional advantage is the possibility to adjust the rotational velocity by using the available control panel on the device.

The rotational speed was varied for the experiments. A range of $0 - 2\ rpm$ could be achieved, enough for the jets to have sufficient time to excavate the soil.

Pile assembly - pile
The experiments will be carried out inside a pile. Its height is the most important dimension, due to the length of the soil plug. Alongside a soil plug length of $\sim 0.4\ m$ and a water column of $0.5\ m$ at the start of the experiments, there should also be enough space for the tool to perform in. In order to achieve this, a pile with a height of $H = 1.5\ m$ was proposed. The soil plug length mentioned here is sufficient to perform all necessary tests required while returning comprehensive measurements.

The acrylic pile is transparent, in order for the viewer to gain insight, to some extent, in the physical processes that take place inside. Measuring tape is added to the pile; so that the amount of clay removed during each test step can be observed and hence be translated to an average progress rate (production).

The scaling scenario returns an outer diameter of $300\ mm$. The wall thickness is set to a value of $5\ mm$, returning an inner diameter of $290\ mm$.

The pile is part of an assembly (see Figure 3-8). Some tests require for the remaining space (excluding soil plug and initial water column) inside the pile to be filled with water. This implies that water will be spilled over a short period of time. An overflow with an attached draining pipe guides the spilled water to the outside without splashing over electrical components and/or reducing sight on the pile.

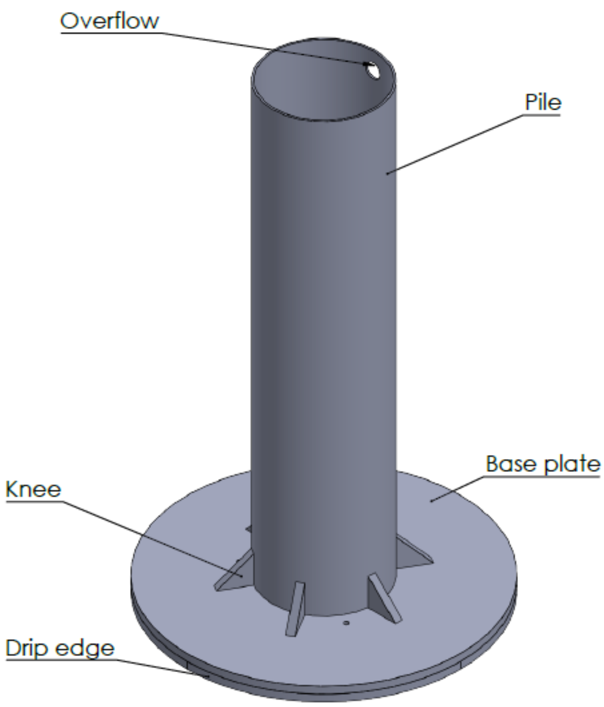

Figure 3-8: Pile assembly made of plexiglass

Supply pumps - jet water

As mentioned before both low-pressure as high-pressure jets were tested. As an indication, the jet pressure in dredging practice varies in the range $20 - 1000\ bar$. The jet pumps however will be selected based on water discharges used in dredging practice $240 - 5000\ l/min$. The final decision is based on delivered power. Because of efficiency losses in the system in between; the calculated hydraulic power is assumed to be at least $20 - 30\ \%$ lower than the delivered power by the pump. An overview is given in Table 3-5.

Table 3-5: Supply pumps

Pump type	Pressure (bar)	Theoretical discharge (l/min)	Pump name
High Pressure (HP)	130	19	Kranzle quadro 1200 TST
Medium Pressure (MP)	30	19	
Low Pressure (LP)	3	60	Kärcher home&garden BP7

From Table 3-5 it is clear that the same pump will be used for both MP as HP. This pump is equipped with stepless pressure regulation. This fully adjustable control allows for operating pressures to be set between 20 and 180 bar.

Jet water distribution system

Both static as rotating jets are implemented in the test setup. A straight single-point distribution pattern (i.e. spray angle of 0°) is selected in accordance with the prototypes. See Figure 3-9 for the spray pattern.

The angle under which these nozzles perform (i.e. nozzle angle) can be altered though. This is the angle the nozzle makes with respect to the vertical. The inclined angles are realized in the jetting head, see Subsection 3.4.1. It should be noted that during a test not necessarily all nozzles have the same configuration in terms of the nozzle angle.

All equipment needed for jet supply in the stage between the supply pump and clay layer (hose, fittings and nozzle) are linked by means of a threaded connection. A standard 1/4" NPT thread is desired with or without additional fittings depending on the equipment that is available. NPT stands for *National Pipe Thread,* an American standard thread which is often used for hydraulic components.

Figure 3-9: Solid stream nozzle with external thread

Water supply: tap water
Fresh water will be used during the experiments for jetting water. The delivered water comes from the water supply network available in the laboratory. This network has a water pressure of $2\ bar$.

To maintain the water column inside the pile a fire hose with a steady supply of water will be placed inside the pile. The amount of water supplied can be altered to achieve an adjustable discharge between $0 - 56\ l/min$. In dredging practice however, the pile is filled with saline water instead of fresh water. Saline water is denser than fresh water due to its salt content. Because of the relatively small density difference between the two, it is presumed acceptable to use fresh water instead.

Dredge pump and discharge - slurry transport
An airlift diameter over pile diameter ratio of 0.1 is used in dredging practice. It should be noted that this ratio serves as a lower boundary. Unlike the tool diameter, the airlift diameter is preferably as large as possible in order to prevent blockages from happening.

An airlift however cannot be used for these experiments. The reason for this is the limited hydraulic head available in the system. The force applied is insufficient to establish the required vacuum. Instead, a dredge pump (DP) i.e. centrifugal pump is used to remove the slurry.

After leaving the centrifugal pump trough the outlet/discharge, the slurry will end up in a dedicated sump tank. The sump tank is dived in two parts with equal volume. The slurry transported through the discharge line ends up in the right half of the tank, where a big bag is placed that holds most clay particles and serves as filter. The partition between the two sides leads to a water flow from the right side to the left side of the tank. The LSP (pump P4) placed inside this compartment transports the water towards a water reservoir that can be drained into the sewer.

The water draining capacity of the water reservoir is smaller than the discharge capacity of the DP and LSP. Hence, the tests were carried out in intermediate steps i.e., the tests were stopped periodically in order to assess the process that has taken place inside.

The supply pumps mentioned above, each have a single water outlet. Fittings must be implemented to connect all hoses. Appendix A.4 shows the schematic representations of all the jet supply connections i.e. fittings applied for the LP-system and the MP&HP-system.

In both setups a maximum of 8 connections can be achieved overall. The number of connections is restricted by the diameter of the tool and the width of available tube clamps. Taking these two restrictions in mind, only two nozzles per slot can be positioned. In short, a configuration with 8 nozzles is examined in both test setups.

Finally, the nozzle diameter, an important parameter in the experiments, is given by an equivalent nozzle diameter that can manage the discharges of the supply pump at operating pressure. Both systems have been developed in such a way that hydraulic losses are kept low. An overview of the nozzle diameters corresponding to the specific pumps from Table 3-5 is given in Table 3-6.

Table 3-6: Nozzle diameters

Pump type	**Nozzle diameter** (mm)
HP	0.50
MP	1.00
LP	2.30

3.4.3 Data acquisition and logging

Sensors
A set of different sensors is added to the test setup in order to capture the data that is needed for the analysis afterwards. These sensors also contribute to the experiments themselves by returning information that will be used to change input parameters, e.g. suction capacity and jet pressure.

An overview of the parameters to be measured and the corresponding sensors is given in Table 3-7. Three measuring tools are added to determine clay strength and progress rate of the tool.

Table 3-7: Sensors and measuring tools

Parameter	**Sensors**	**Range**
Pump pressure (HP&MP)	Pressure sensor	$0-200\ bar$
Pump pressure (LP)	Pressure sensor	$0-6\ bar$
Slurry discharge	Flow meter (electromagnetic)	$0-5\ l/s$
Jet pressure	Pressure sensor	$0-200\ bar$
Soil plug weight	Loadcell (x3)	$0-300\ kg$
Undrained shear strength	Shear vane	$0-100\ kPa$
Vertical velocity (tool)	GoPro Camera	$-$
Progress rate	Measuring tape	$0-3\ cm/min$

A dedicated data analysis was performed after completing the experiments. During the experiments and analysis, the focus was put on:

- Soil collapse mechanism
- Developing slurry
- Particle entrainment / excavating rates

Logging

All incoming signals are processed by a DAQ device (Data Acquisition device), the output signal is transferred to a laptop that includes a *LabView* software package using a ''write to measurement file'' that transforms the raw data to a structured *Excel* sheet. The three incoming signals correspond to the three sensors depicted in Figure 3-10.

Figure 3-10: Sensors connected to the data logger. From left to right: pressure sensor, flow meter and load cell.

The pressure sensor is placed between the supply line of the SP and main hose of the jet water distribution system that delivers the jet water to the nozzles. This closed system ensures a reliable value for the jet pressure. The unit applied here is $bar = 10^5\ N/m^2$. The pressure can be regulated manually.

The flow meter is connected between the first stage of the suction line and the second stage of the suction line. It returns values with a unit of $l/min = 0.06\ m^3/h$. The discharge can be regulated manually in two ways: through the speed of the DP and the gate valve at the discharge line.

The load cells are placed on top of wooden blocks and attached right under the welding positioner. Two at the front (2 times $300\ kg$) and one at the back (1 times $200\ kg$). Three-leg weighing systems balance like a tripod, with load distribution being virtually automatic. Vertical cylindrical systems, like the one used here are often measured at three points. The cells are preferably placed at equal distance from each other in a circle orientation ($120°$) apart. The SI-unit kg is used here. The weight can be altered manually in two ways: by rotating the control valve at fire hose and/or rotating the gate valve at the discharge line.

3.5 Cement-bentonite mixture

3.5.1 Introduction

In most experimental research with clays, a specific natural clay is chosen. From there on different tests will be carried out. This especially holds true for experiments on physical scale and the ones that are site specific.

In this research however, the clay is primarily scaled based on its undrained shear strength. For the experiments, the emphasis lies on stiff to hard clays. The resulting clay strengths that are examined are $20, 60$ and $100\ kPa$ on model scale (see Table 3-2). Assuming a penetrating jet with a stagnation pressure over shear strength ratio, i.e. p_{stag}/s_u that has to be larger than 12.

There are multiple options for choosing the desired clay. One option is to use bentonite that needs to be consolidated to reach the desired clay strength. This process however has a huge drawback considering the experiments that will be performed here. The consolidation process is very time-consuming, especially for high clay strengths such as $100\ kPa$.

Eventually, the decision is made to prepare the clay in the laboratory in Delft and to not outsource the procedure. The clay that will be used in this study is a mixture of **bentonite and cement**. The required clay strength is achieved by varying the amount of cement that is added. The shear strength is measured by means of a shear vane test. This test is carried out with equipment consisting of a rod with vanes mounted to it that is inserted into the ground and rotated. A gauge on the top of the rod measures the torque required to cause failure of the soil and provides a conversion to shear strength. See Figure 3-11 for an overview of the system.

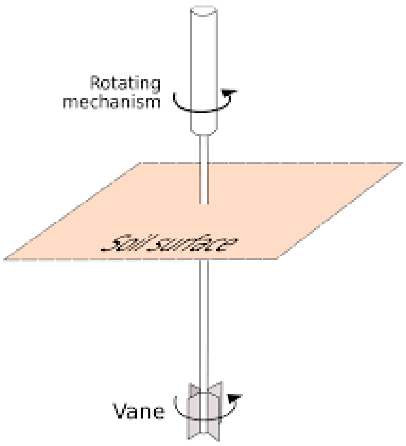

Figure 3-11: Shear vane system

The chemical composition of the cement and bentonite used in this study is given in Appendix B.

3.5.2 Clay preparation system

Prior to starting with the jetting experiments, the simulated clay material must first be examined in order to give insight in the quantities that are needed for the scale tests. In short, how much cement and bentonite is required to fill the pile up to $\pm\ 400\ mm$ for undrained shear strengths of $20, 60$ and $100\ kPa$?

Small samples of artificial clay were prepared in $2.5\ liter$ buckets (see Figure 3-12). The shear strength is controlled by varying the cement content. To avoid large disturbances, a hand shear vane was used to measure the shear strength. To prevent the clay from failing sideways, the shear vane is supposed to penetrate the clay vertically. The tail-end of the vane was lowered completely into the soil and rotated at a steady speed of approximately $1\ rpm$.

Three shear vane sizes are provided along with the hand shear vane: Small (S), Medium (M) and Large (L). The value that can be read from the gauge on top of the shear vane rod must be multiplied by the numbers as illustrated in Figure 3-13, $READ$: $S \cdot 2, M \cdot 1, L \cdot 2$. The values calculated from this straightforward rule provide the undrained shear strength s_u of the clay.

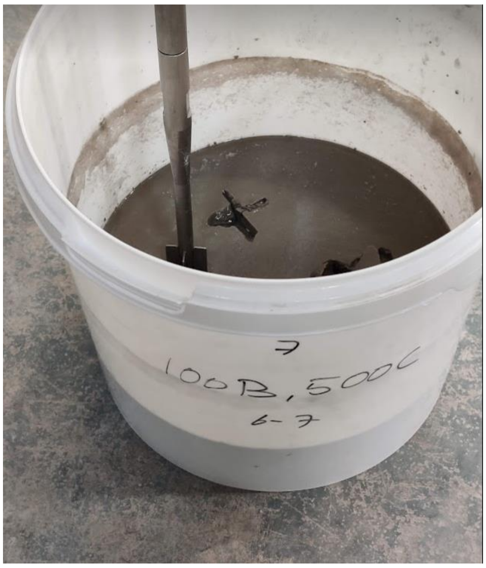

Figure 3-12: Soil sample with shear vane

Figure 3-13: Measuring gauge of shear vane

The clay samples were prepared in accordance with the following steps:

1. Add a quantity x_c of cement C to the bucket
2. Add a quantity x_B of bentonite B to the bucket
3. Dry mix C and B
4. Add a quantity x_w of water
5. Mix all components using a drill-mixer
6. Cover bucket with plastic wrap to prevent water loss

The first batch contained 12 samples from which 3 samples had the same composition for reproductivity purposes. The batch contained two series. The first series used $100g\ B$ to which $100 - 500g\ C$ was added in incremental steps of $100g\ C$. The second series used $200g\ B$ to which $100 - 500g\ C$ was added in the same steps as was done for the first series. All 13 samples had the same water quantity of $1000\ ml$. Measurements were taken after 24 hours. The next day, each sample contained a water layer of approximately $400 - 500\ ml$ after inspection . This bleeding effect, which is also encountered in concrete structures, is the result of excess water being forced to the surface of the mixture.

Hence, the mixtures are completely saturated and the resulting shear strengths are therefore not representative.

The amount of excess water in the first batch was measured for all samples and deducted from the initial water quantity of $1000\ ml$ for the second batch. A new series of $300g\ B$ was introduced in batch 2, taking the place of the $100g\ B$ series, due to the fact that the shear vane came in contact with the bottom of the bucket. There was simply not enough material in this series to fill the bucket up to a level in which the vane was completely lowered into the clay.

After some finetuning the fourth batch delivered valuable results for this study. The quantities of the batch are given in Table 3-8. A normalised value gives the influence of water, the so-called Cement - to - Water Ratio (CWR).

Table 3-8: Artificial clay samples

Sample	**Water**	**Bentonite**	**Cement**	**Vane size**	$\boldsymbol{CWR}$
	(ml)	(g)	(g)	$-$	(g/ml)
1	450	300	70	S	0.16
2	525	300	125	S	0.24
3	550	300	160	S	0.29
4	525	300	200	S	0.38
5	550	300	250	S	0.45

The blue shaded rows indicate the desired values needed to obtain undrained shear strengths of $20, 60$ and $100\ kPa$ after $24\ hr$ for samples 1,3 and 5 respectively. Samples 2 and 4 correspond to 40 and 80 kPa respectively. These last two samples fall out of the scope of this study, but were nevertheless examined to give a more thorough image of shear strength increase over time.

The results shown in the graph in Figure 3-14 are normalised by dividing the amount of cement by the amount of water added. In this way different CWR- values can be compared to each other. The amount of bentonite is kept constant.

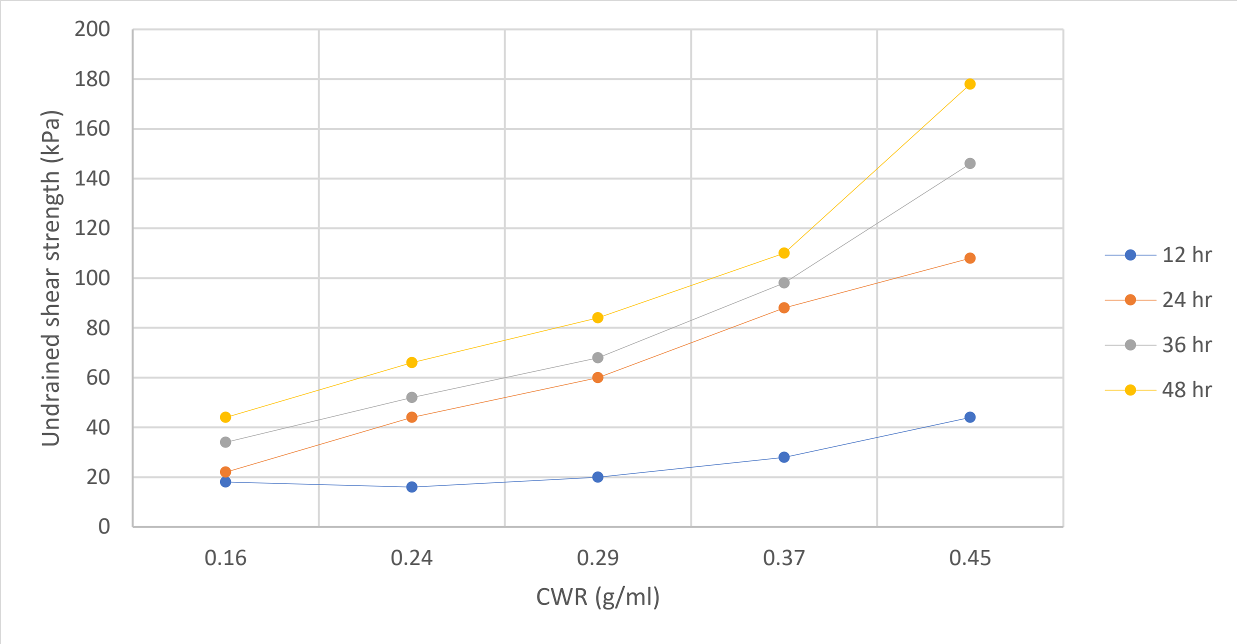

Figure 3-14: Correlation between cement-to-water ratios (CWR) and undrained shear strength for different curing times

There is an obvious trend that a higher cement content will result in greater shear strength and longer curing times will result in greater shear strength for the same cement content. For the purpose of controlling the moisture content of the clay, the ratio of water, bentonite, and cement was kept the same for every sample of artificial clay.

The trend observed from the $12\ hr$ line deviates from the other three lines. An explanation can be that a curing time of $12\ hr$ is simply too short for the cement to adequately dry. The chemical reactions discussed in Appendix B are most likely still in their initial stages and far from finished for the cement to harden.

The three shear strengths mentioned at the begin of this section are attained with CWR- values of $0.19, 0.29$ and $0.45\ g/ml$ after a curing time of $24\ hr$ as shown in Figure 3-15. Although $CWR = 0.16$ and $CWR = 0.45$ do not match completely with the aforementioned shear strengths, the quantities provided in Table 3-8 are sufficiently close that they can be translated to quantities used in the jetting experiments. Figure 3-14 also contributes to this argument, because the tests do not necessarily need to be performed after $24\ hr$. A time frame of $19 - 24\ hr$ is used during testing. This time frame guarantees enough time to perform a jetting test; taking starting and ending time into account.

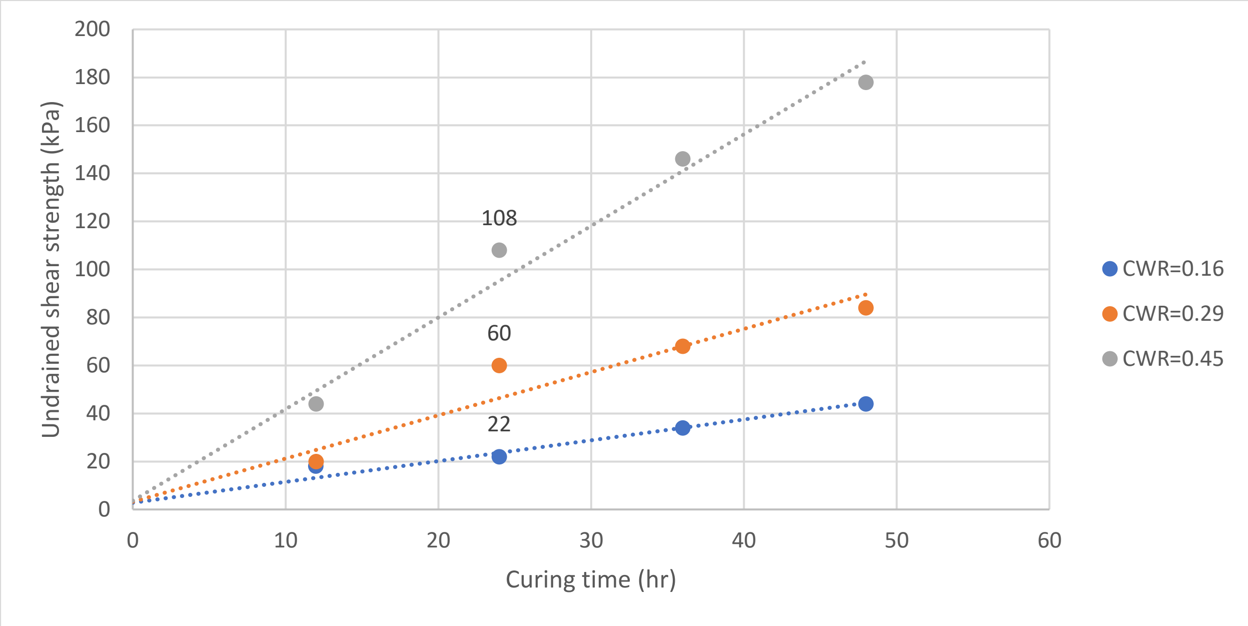

Figure 3-15: Correlation between curing time and undrained shear strength for cement-bentonite mixture

3.5.3 Effect of curing time on main experiments

The time frame in which tests are performed is an indispensable parameter in this study. As explained above, the shear strength of an artificial clay to which cement is added is a function of the curing time; opposed to a natural clay that has a constant shear strength independent of time. In one of the main experiments encountered later on in Chapter 5 it was tried to give insight in the effect of time on production, see Figure 3-16.

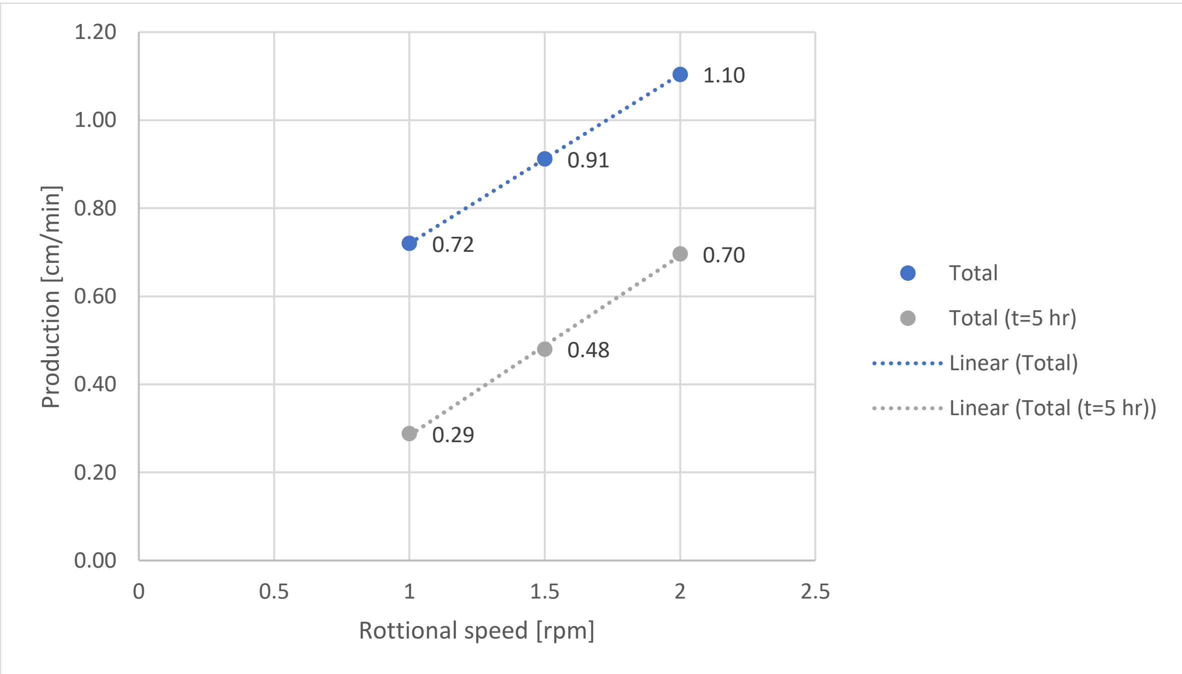

Figure 3-16: correlation between rotational speed and production for $s_u = 20\ kPa, p_j = 3\ bar$

Performing the same rotational jetting tests on a single batch of clay, but with $t = 5\ hr$ in between the start of the first round of tests and the second one, a significant decrease in progress rate of

$\sim 0{,}4\ cm/min$ is observed (across all datapoints). This contributes to the stance that these artificial clay tests are reproducible.

Another conclusion from this graph is that the tests carried out on a single batch should be carried out in a small but convenient time frames i.e. waiting too long will return invalid results for the examined shear strength. The properties of the clay will reflect those of a stiffer clay; the cement is still curing and hardens progressively. Turning back to Figure 3-15 a value of $s_u(t = 5\ hr) \approx 30\ kPa$ can be read from the graph; as was expected an increase that cannot be neglected.

Throughout the entirety of the test program these observations were taken into account and dealt with. Due to circumstances (e.g. emptying sump tank in between tests, resolving errors like blocked nozzle outlets etc.) the experiments performed at the end of a testing day, for rotational speeds $n = 2\ rpm$ (see test procedure laid out in Chapter 4), could be slightly underestimated.

3.5.4 Natural (modelling) clay

During the experiments an attempt was made to also investigate the performance of the developed jetting tool when operated in natural clay. The emphasis clearly is on the different behaviour encountered in natural and artificial clay. This is reflected in the difference in plasticity. It is assumed that a natural clay, in general, is more plastic than a mixture to which cement is added. After all, with the adsorption of free water by the cement the chemical reaction of cement hydration will produce a brittle substance. The chemical properties of the selected natural clay (in fact a modelling clay) can be found in Appendix B.

The shear strength of this natural clay was determined in the same way as was done for the artificial clays, namely using a shear vane. A shear strength of $s_u = 30\ kPa$ was measured.

3.6 Preliminary experiments

This section describes preliminary experiments that were undertaken to reduce the number of unsupported assumptions and design decisions. Another purpose of these tests was to familiarize with the concepts, equipment, and procedures in order to get a better understanding of the main experiments that follow in Chapter 5.

A total of three experiments were performed after which the following points were identified:

- The soil was mechanically excavated by the nozzles that were in direct contact with the soil. This led to an added form of excavation production in the form of cutting (only for the MP&HP configuration)
- The progress rates encountered were relatively small compared to what was assumed beforehand. This led to a re-evaluation of the time scale and batch size of the experiments.
- The provided/calculated jet discharges deviate from the ones encountered during testing. This led to adjustments in jet momentum and specific energy
- The selected nozzle configuration was unsuitable for efficient soil excavation. This led to repositioning the nozzles in the jetting head.

The same test setup was used as the one described in Secttion 3.4 for the main experiments. It has been decided to perform all preliminary tests on an artificial clay with a shear strength of $s_u = 60\ kPa$. This is the most representative clay out of the three that were tested. It is not too stiff ($s_u =$

$100\ kPa$) and not too soft ($s_u = 20\ kPa$). The same reasoning was used for the applied jet pressure of $p_{jet} = 30\ bar$, since ($3 < 30 < 130\ bar$).

Excavation method and jetting head

The failure mechanism could not be properly evaluated during the preliminary experiments. The reason for this is the orientation of the last stage of the jet water distribution system (see Appendix B). The nozzle mountings that were added to the MP&HP jetting head to secure the nozzles stick $35\ mm$ out from underneath Nozzle plate B, as can clearly be seen in Figure 3-6. Putting the tool down on top of the bed while rotating the pile therefore resulted in excavating behaviour that resembled that of a plough or cutter head instead of a jetting device. Two deep rings of $\sim 50\ mm$ were observed after the tests (see Figure 3-17). These two rings were located at a distance that corresponded exactly to the arrangement of the nozzles seen from the centreline. Another observation is the poor excavation ability employed by this nozzle configuration to the centre and to the side of the pile.

Figure 3-17: Clay surface after ''ploughing''

These tests results contributed to an adjustment in the design. A wooden disk with a diameter equal to the diameter of the nozzle plates and a thickness of $t = 50\ mm$ was added to the jetting head to hide the nozzle mounts from showing and effectively putting them in the casing of the newly formed head (see Figure 3-18). A simple calculation leads to a stand off distance $SOD = t - 35\ mm = 15\ mm$ for the MP&HP system.

The addition of this wooden disk removed the ploughing effect, but it did not completely get rid of production by cutting. Placing the jetting head on the clay layer and rotating the pile still resulted in some cutting contribution. See Section 2.3 for the theoretical background into cutting (also encountered in dredging practice). This led to the notion that it is crucial to differentiate between hydraulic excavation and mechanical excavation in order to understand what processes occur inside the pile during operation of the jetting tool.

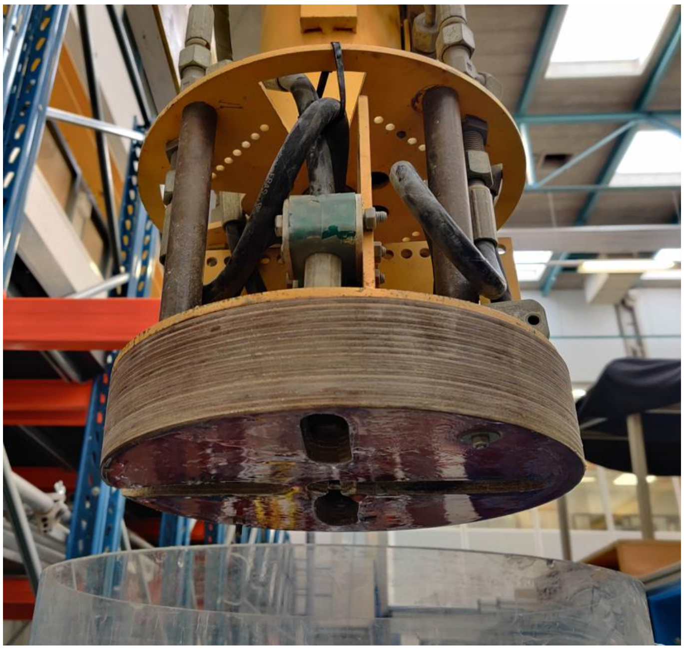

Figure 3-18: Wooden disk mounted on jetting head with SOD=15 mm

Time scale and clay column
The time scale of the experiments is important to determine what minimum volume of clay is necessary to perform all required tests in one batch. This decision was made on the basis of the intermediate results shown in Table 3-9. It is important to note that the time scale was taken as large as possible.

Table 3-9: Preliminary test P3

	Rotational speed	Clay column	Removed layer	Duration	Production
	(rpm)	(cm)	(cm)	$(mm:ss)$	(cm/min)
$Start$	$-$	38.0	$-$	$00:00$	$-$
$T1$	1	27.4	10.6	$21:05$	0.503
$T2$	2	13.9	13.5	$21:55$	0.616
End	$-$				

After a bit more than 20 minutes at rotational speeds of $1\ rpm$ and $2\ rpm$ not more than $\ngeq 15\ cm$ of clay is removed. Bearing in mind that ploughing is present in these results and thus the assumption can be made that, under the same conditions, a jetting head (nozzles inside casing) will excavate less. Moreover, tests during the main experiments will not last longer than roughly between $3 - 12\ min$. Depending on the shear strength tested. Nonetheless, the final results are expressed in (cm/min).

The conclusion that was derived from this evaluation is that making two sets of artificial clay for a batch, in which a set matches roughly $10\ L$ water, provides sufficient clay to perform all tests. Depending on the shear strength a clay column of $38 - 41\ cm$ is attained in this way.

Nozzle discharge
The discharge through the nozzle was calculated according to Eq. (2.21). Two parameters in this equation however, the nozzle discharge c_d and the exit velocity u_0 depend on different assumptions. The nozzles used for the MP and HP tests were manufactured by drilling a hole in a

steel end plug. According to (White, 2011) this method of drilling in steel corresponds to the c_d value of a thin-plate orifice. Since no other parameters are available to determine the discharge coefficient a minimum value of $c_d = 0.61$ was applied here. The exit velocity u_0 on the other hand depends on the friction losses that arise in the system

$$u_0 \propto \left(\sqrt{p_j}\right) = f(\Delta p) \tag{3.1}$$

$$\Delta p = \left(f \cdot \frac{L}{D} + \Sigma K\right) \cdot \frac{\rho u^2}{2} \tag{3.2}$$

In addition to the Moody-type friction loss computed for the length of a hose, there are additional so-called minor losses or local losses due to fittings (T-pieces/Y-pieces) that connect several hoses to each other (see Subsection 3.4.2). The flow pattern that is found in fittings is complex, the theory is very weak. The dimensionless resistance coefficients K were taken from standard tables for branch flow Tees with value of $K = 0.95$ and $K = 3.2$ for LP and MP&HP (White, 2011).

All these uncertainties and assumptions that were made in the beginning contributed to a disparity between the actual discharge and the theoretical/calculated discharge. The difference for the given jet pressure systems is listed in Table 3-10.

Table 3-10: Disparity in theoretical vs measured discharge

Pump type	**Theoretical discharge** (l/min)	**Measured discharge** (l/min)	**Disparity** (l/min)	**Disparity** (%)
HP	9.12	7.13	−1.98	−22
MP	17.41	15.19	−2.21	−13
LP	52.37	53.78	1.41	+2

Both flow rates for MP and HP were overestimated (the same jet water distribution system was used, hence the same coefficients). The LP system on the other hand was underestimated, which implies a loss factor that was selected too low.

The discharge coefficient can now be determined by rewriting Eq. (2.21) as follows:

$$\mathrm{c_d} = \frac{Q_{0,measured}}{A_n \cdot u_0} \tag{3.3}$$

In which $Q_{0,measured}$ is the measured discharge from Table 3-10, A_n is the total flow area of the nozzle and u_0 is the jet exit velocity. The newly calculated discharge coefficients are presented in Table 3-11 alongside the provided/assumed coefficients at the start. As stated above the values for MP&HP were assumed based on theory. The discharge coefficient belonging to LP was provided by the manufacturer.

Table 3-11: Initial vs adjusted discharge coefficient

Pump type	Initial discharge coefficient $(-)$	Adjusted discharge coefficient $(-)$
HP	0.61	0.64
MP	0.61	0.65
LP	0.95	0.89

Nozzle configuration
As was explained in Subsection 3.4.2 a total number of 8 nozzles could be incorporated into the jetting tool. At the start every nozzle pair corresponding to one slot was positioned at the exact same place as the other pairs. This led to only two places of impact (while rotating) and thus only two trenches were observed. The rearrangement that followed from this observation had the objective to implement a nozzle configuration in which each nozzle is situated at a different distance from the centre of the tool. The effective contribution of the nozzles is increased in this way, because the impact over the surface is increased. In short, each jet will have its own place of impact. This of course does not mean that the jets will not be able to influence the point (static) or path (rotating) of another jet. Turbulence effects present underneath the jetting head would imply this.

Another result of the preliminary experiments was the inadequate removal of clay from the sides of the pile and near the centre, see Figure 3-17. This resulted in inclining two nozzles under an angle of 45°. Nozzle $N2$ faces inward towards the centre of the tool and nozzle $N5$ faces outward towards the pile wall. A schematic representation of the final nozzle configuration is given in Figure 3-19.

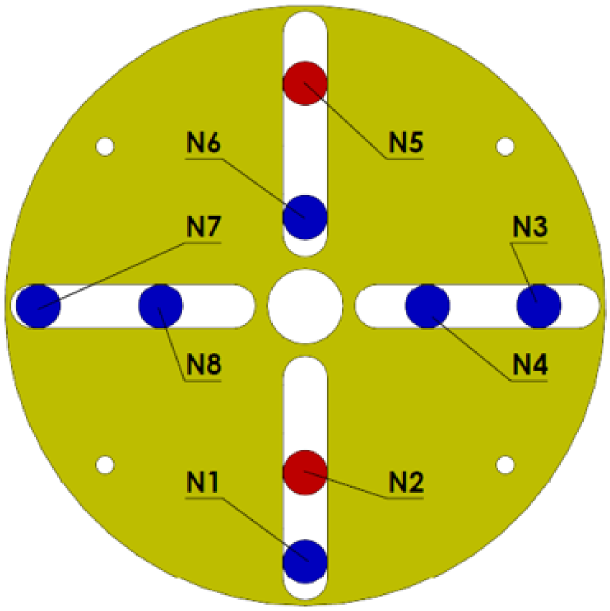

#	Distance to centre (mm)	Nozzle angle (°)
N1	115	0
N2	75	45
N3	105	0
N4	55	0
N5	100	45
N6	40	0
N7	120	0
N8	65	0

Figure 3-19: Nozzle configuration. N2 is directed inwards, N5 is directed outwards.

Nozzle $N2$ is placed at a relatively large distance ($75\ mm$) from the centre. This has a practical reason, namely moving the nozzle closer to the centre would make the resulting jet hit the suction pipe.

4 Experiments and methodology

4.1 Introduction

The primary goals of this study are to investigate the achievable excavation production and overall performance of different soil plug removal concepts in cohesive soil. This chapter describes laboratory jet excavations that were conducted using an artificial clay. This study focuses on a jetting head in which a total number of 8 nozzles were fitted. This will establish the fundamental framework for understanding the jet-soil interaction behaviour.

The objectives of the laboratory measurements were to observe the physical form (geometry, mixing) of the excavation to clarify the mechanisms of jet excavation, and to validate the analytical relationships linking operational parameters of the fluid jet and shear strength properties of the cohesive soil described in Chapter 2. In order to formulate an answer to the main research question, it is of importance to vary different testing parameters while keeping others constant. This makes it possible to distinguish between the influence of one parameter over the other. To this avail, a test matrix was setup in Section 4.2. This chapter ends with an investigation into reproducibility testing in Section 4.3.

4.2 Test matrix

A total number of 88 experiments are performed, divided over 11 batches of clay ($B1 - B11$). That amounts to 8 tests per batch, excluding repeated tests for reproducibility purposes (see Section 4.3).

Tests on a batch were carried out on a single day, since the prepared clay could not remain in the pile until the next day. The additional curing time overnight would increase the shear strength of the mixture that is examined (see Figure 3-16); effectively returning a ''different'' clay type making measurements on the same batch irrelevant. Another potential obstacle is the risk of a significant increase in shear strength in such a way that it would be impossible to get the mixture out of the pile without damaging it. Another contributing factor is that the prepared clay cannot be used immediately, since the cement takes at least $20\ hr$ to cure. Therefore, it is crucial to complete all required tests on a batch, so that the pile can be cleaned, and another batch can be added the next day.

The test matrix is compiled in such a way that the test results can be assessed as follows:

- For a specific type (see Subsection 4.3.1) a set of three datapoints can be constructed while keeping all other parameters constant

See Table 4-1 below. All measuring tables corresponding to a batch are given in Appendix C.

All tests are performed using the same nozzle configuration, incorporating 8 nozzles (see Figure 3-19).

Table 4-1: Test matrix

#	p_{jet}	s_u	$Measured\ s_u$	D_n	Q_0
	(bar)	(kPa)	(kPa)	(mm)	(l/min)
$B1$	3	20	22	2.3	53.8
$B2$	3	20	24	2.3	53.8
$B3$	3	60	62	2.3	53.8
$B4$	30	20	18	1.0	15.2
$B5$	30	60	60	1.0	15.2
$B6$	30	100	106	1.0	15.2
$B7$	130	20	22	0.5	7.1
$B8$	130	60	60	0.5	7.1
$B9$	130	100	98	0.5	7.1
$B10^*$	30	30	30	1.0	15.2
$B11^*$	30	30	27	1.0	15.2

4.2.1 Test procedure

Each batch $(B1 - B11)$ is examined according to a test procedure that incorporates the following parts:

1. Static test
2. Stepwise rotation test
3. Rotational test
    a. $n = 1.0\ rpm$, No jets
    b. $n = 1.0\ rpm$, jets deployed
    c. $n = 1.5\ rpm$, No jets
    d. $n = 1.5\ rpm$, jets deployed
    e. $n = 2.0\ rpm$, No jets
    f. $n = 2.0\ rpm$, jets deployed

This returns 8 distinctive tests for each batch, as was mentioned before. Batch $B10^*$ and $B11^*$ were added to the test matrix and mainly serve as experiments related to (reproducibility) tests on natural modelling clay (see Subsection 4.3.2 for a more in-depth study). The measured shear strength of $s_u = 30\ kPa$, fell outside the scope of clay strengths as given for the artificial clays $B1 - B9$. Therefore, a new batch of artificial clay was prepared in $B10^*$ with an identical shear strength of $s_u = 30\ kPa$. The tests in experiment $B11^*$ were performed on the natural clay mentioned here.

The test procedure focusses on two main findings: jetting head movement and the difference between hydraulic and mechanical excavation. Both are described below.

Pile movement

Considering the different soil plug removal concepts from Table 1-1 it is clear that there are different approaches to head movement (i.e. pile movement in this test setup). The jetting head is either static or rotating while it is operating. The tool developed by *Claxton* is listed as static. This is in fact only true while it is jetting a particular part of the clay. The tool is not operated continuously, rather it jets one part, is turned off, rotated by 30° and then turned on again to jet the next segment. This process is repeated in the same incremental steps of 30° until a full rotation is realised. This sequence is added to the experiments that were carried out and to distinguish it from the continuously rotating concepts employed by *Deco* and *Deep C* it is listed as stepwise rotation. The *Boskalis* tool corresponds to static head movement.

Excavation
As a consequence of placing a SPRT on top of the clay layer, mechanical excavation by cutting also helps to loosen and remove soil next to hydraulic excavation by water jets (see Section 3.6). Although, this study focusses on hydraulic excavation, the contribution of clay cutting cannot be ignored. This led to performing every test in which cutting plays a role twice (essentially only the continuous rotating tests). First a test was carried out by rotating the pile without turning the jets on, giving insight in the cutting process and the resulting production (Test $3a, 3c, 3e$)

Subsequently, the same test was carried out during the same time frame, but this time with the jets turned on (Test $3b, 3d, 3f$). The difference in production was subtracted from the total production observed in the jetting experiments. This approach made it feasible to differentiate between the contribution of cutting and jetting.

4.2.2 Test protocol

The various components, preparations and proceedings in this study call for a thorough and elaborate test protocol. This test protocol is divided into two parts. The first part mainly deals with preparatory works related to the production of artificial clay. These preparatory works were carried out the day before the actual experiments took place. The second part involves all the steps that were taken right before and during the experiments. The complete procedure is given in Appendix D. Critical steps are made bold; two of those steps are marked in red and describe two important processes described below.

Vent system
A dredge pump is thus used to remove the slug from the pile. This centrifugal pump can remove slurries with particles up to a diameter of $40\ mm$. Unlike a vacuum pump, a centrifugal pump cannot pump a gas; therefore, the differential pressure necessary for flow will not be created if the impeller is filled with air. The suction line of a non-self-priming centrifugal pump must be primed prior to the pump's start-up. This includes the suction pipe that runs through the SPRT shaft. Initially a vacuum must be created to draw the liquid into the eye of the impeller.

The system is vented by connecting the SSP (P1) to the discharge of the DP. Before turning the SSP on, its valve must be turned on, while shutting off the valve from the discharge line. This action will result in a consecutive priming of the impeller and the entire suction line which essentially serves as a vent line at start-up. This process is continued for several seconds, even after water is already exiting the suction pipe and filling up the pile. This is done to make sure that all air bubbles are removed from the vent line to ensure a good working discharge after. The SSP valve is now shut off while the valve situated at the discharge line can be turned on. Turning on the DP afterwards results in a steady mixture discharge at the outlet of the centrifugal pump. This discharge can be modified by increasing/decreasing the speed (rpm) of the centrifugal pump or manually turning the gate valve at the outlet of the discharge line.

Vertical displacement of the tool
Regarding pile embedment, it is assumed that the piles for which this jetting tool will be operated are vertically embedded into the soil. However, it is quite possible that some piles will be under an angle. These piles are excluded in this research.

During excavation, the SPRT is displaced vertically in the pile while it excavates the soil plug. Due to the ship’s heave motion, as a result of waves, the tool could potentially be exposed to heavy impacts inside the pile. One way to solve this is to implement heave compensation by means of a dedicated vessel crane. Another option is to use an internal winch instead. This controls the descent in such a way that it makes a vessel crane redundant. However, this option would have led to a more complex tool and potentially more prone to failure due to the addition of moving components. Therefore, this study focusses on a tool that is capable of working solely by vessel crane.

The overhead crane available in the laboratory is used in combination with the centre frame (see Subsection 2.4.1.). The crane's hook is attached to the jetting tool by adding two lifting eyes to the topside of the flat bars. The crane is operated with a special remote control.

4.3 Reproducibility testing

4.3.1 Artificial clay

To determine if the tests that were performed were reliable or not some insight in the reproducibility of the experiments needs to be obtained to make sure that the reported study is somehow validated. During the course of the experiments already a couple of tests were repeated on the same batch of clay. Also encountered in Chapter 5 are the repeated mechanical excavation tests (i.e. cutting production) performed for MP and HP. These were performed on separate days on newly prepared batches as explained before. The results were, excluding some minor deviations, positive. This can already be labelled as an independent experiment.

Separate batches

To truly capture the entire scope of a single experiment, all tests performed in such an experiment need to be repeated on a newly prepared batch keeping all parameters constant.

For the LP tests two single batches were prepared over the course of two days. The first batch $\boldsymbol{B1}$ denoted as $\mathbf{20}\ \boldsymbol{kPa}\ (\boldsymbol{a})$ had to be prepared anyway, because it was part of the test matrix. The second batch $\boldsymbol{B2}$ however, denoted as $\mathbf{20}\ \boldsymbol{kPa}\ (\boldsymbol{b})$ was solely prepared to serve as an independent experiment to verify whether results were reproducible or not. Figure 4-1 shows the individual experiments and the production achieved. The closed dots represent the results belonging to $\mathbf{20}\ \boldsymbol{kPa}\ (\boldsymbol{a})$, while the open dots display the $\mathbf{20}\ \boldsymbol{kPa}\ (\boldsymbol{b})$ points.

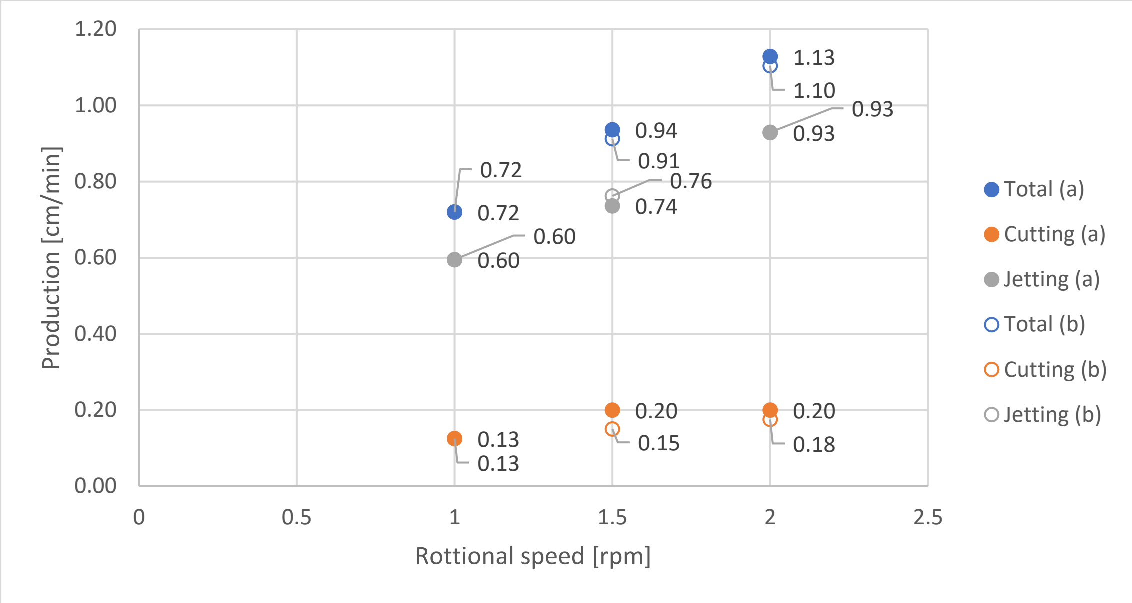

Figure 4-1: Correlation between rotational speed and production for $p_j = 3\ bar$ and $s_u = 20\ kPa^*$

The results are almost identical. The small deviations encountered can be assumed negligible.

As described above the cutting production tests were also reproduced for MP&HP and in those instances the differences were smaller and for $s_u = 60\ kPa$ identical (2 decimal places). A reason could be an inhomogeneity in the clay mixture that was produced, reading error or a temporary blockage of the suction pipe (although there is no sign of significant irregularities in the logged data for pressure and/or mixture discharge).

Overall, the disparities observed are all smaller than 4% and can therefore be subscribed to simple measurement errors and differences in (measured) shear strength. The latter is almost impossible to rule out, because of the ongoing binding of water particles to cement particles that takes place.

Single batch
Reproducibility across separate batches with identical features is meaningful and says something about the consistency of batches produced for experiments in which different base parameters are altered. This says nothing though regarding the quality of a single batch and on which parameters the changes in progress rate are based.

A single batch for a MP test was produced with $s_u = 100\ kPa$. The same progress rate test at $n = 1\ rpm$ was repeated 5 times. The total production was measured for each particular test. The values are given in Table 4-2.

Table 4-2: single batch test for $s_u = 100\ kPa$ and $p_j = 30\ bar$.

$Test$	$Rotational\ speed$	$Clay\ column$	$Removed\ layer$	$Time$	$Production$
$(-)$	(rpm)	(cm)	(cm)	$(mm{:}ss)$	(cm/min)
$T1$	1	44,5	0.5	05:50	0.086
$T2$	1	44.0	0.5	05:30	0.091
$T3$	1	43,5	0.5	05:50	0.086
$T4$	1	42.0	1.7	18:00	0.094

The duration of experiments $T1 - T3$ is almost equal, the same holds true for the resulting values of production given in the right most column. For $T4$ the duration of the experiment was increased 3 times. The effect of a longer testing period was added for comparison reasons only. The regular experiments for which the measuring tables are given in Appendix C were performed in shorter time frames $t = 3 - 6\ min$. Given limited time available in the laboratory to perform all steps from the test protocol (see Appendix D) and taking hydration of cement into account it is not feasible to delay tests much. The assumed time frame is reasonable for the experiments as performed in this study; based on progress rates.

The differences in production (both for shorter as for the longer time frame) can be assumed negligible for a single batch and thus reproducibility is achieved (no large deviations encountered).

4.3.2 Natural clay

Natural clay vs artificial clay

The natural clay introduced in Subsection 3.5.4 is thus examined and compared to an identical artificial clay in terms of shear strength. The results of both clay types are plotted in Figure 4-2. The values for the natural clay are presented as closed dots and denoted by the characters NC between brackets in the legend to the right of the plot. The values for artificial clay correspond to the open dots and are characterised in the legend by AC.

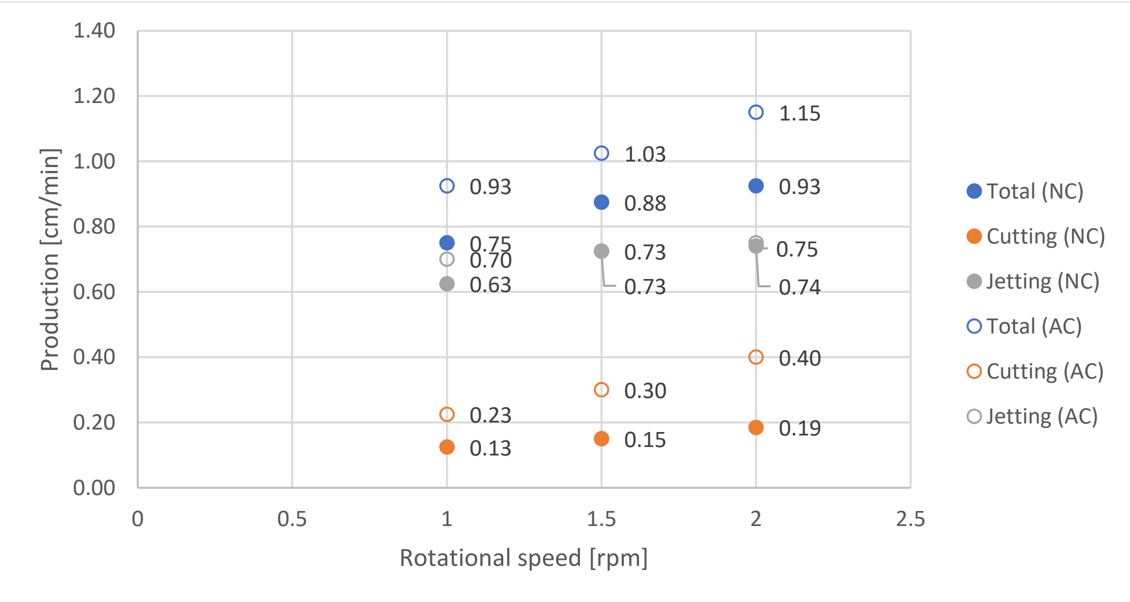

Figure 4-2: Correlation between rotational speed and production for $s_u = 30\ kPa$. NC=Natural Clay, AC=Artificial Clay.

The total production for NC is roughly 0.2 cm/min lower than for AC. This difference is accounted to the distinctive difference in plasticity between the two clays. This manifests itself in the cutting production, since NC is more adhesive than AC (i.e. visual observation) shearing of the jetting head led to natural clay accumulating on top of the head instead of moving towards the suction inlet, hindering a steady transit of particles. This is not the case for the artificial clay hence the cutting production is larger for AC.

Single batch
The natural clay introduced in the above gave insight in variations dependent on variables like plasticity and adhesion. To support this analysis, it is important to also validate the reproducibility of tests performed on this natural clay. In Figure 4-3 the initial tests are denoted by NC (correspond to values in Figure 4-2) and the dataset introduced to check reproducibility is indicated by $NC2$.

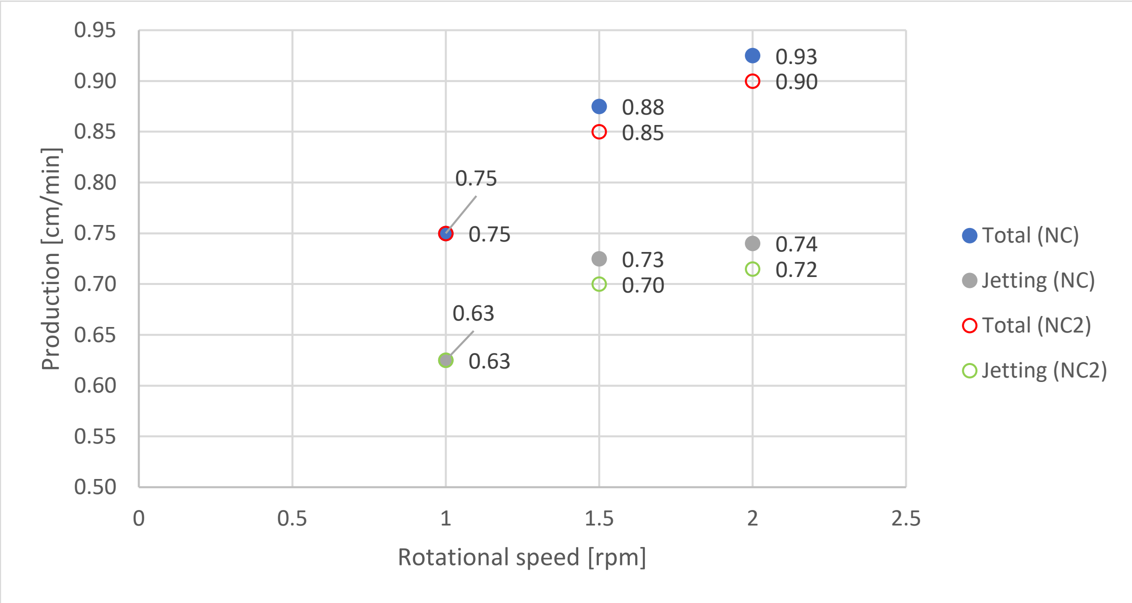

Figure 4-3: correlation between rotational speed and production for a natural clay ($s_u = 30\ kPa\ and\ p_j = 30\ bar$).

The datapoints for $n = 1\ rpm$ coincide and are plotted right on top of each other. For $n > 1\ rpm$ the $NC2$ values are marginally smaller than the initial tests. Cement curing does not play a role here, for obvious reasons, hence these small deviations can be attributed to measuring errors. Reading the measuring tape from the side of the pile was somewhat challenging in some instances and could have contributed to these errors.

5 Results and observations

5.1 Introduction

This chapter presents the results from all the jetting experiments, including observations made on the physical form of the excavated clay after certain experiments with regard to cavity depth and width. The main objective was to determine the production that could be achieved by altering different parameters and keeping others constant. This production is determined by reading the amount of clay removed from measuring tape attached to the pile. In this way an average progress rate v_p was determined by dividing a length scale over time hence returning an average vertical velocity, defined as the lowering rate of the jetting tool in $[cm/min]$. The influence of static and rotating jets is discussed in Section 5.2 and 5.3, respectively. The influence of jet pressure p_j and undrained shear strength s_u is discussed in Section 5.4. The results regarding set down pressure of the tool, stepwise rotation and single nozzle water jet are given in Section 5.5.

5.2 Static production

The progress rate was negligible for all static jetting tests performed in this study. Figure 5-1 shows a typical view of the bed after a static test. The orientation of this figure corresponds to Figure 3-21. You can clearly distinguish 6 cavities (encircled in red) that were formed by the vertical nozzles. The impact of the nozzle that was placed under an angle of $45°$ inwards (towards the centre of the pile) also penetrates the soil, although not as visible as for the vertically placed nozzles. Arrow **N2** indicates the zone of impact of this inward facing nozzle. What remains is the influence of the nozzle that is directed outwards. In a static setting this nozzle does not have an effect at all (we will see later that the opposite holds true for a rotating setting). It is evident from arrow **N5** that no zone of impact was developed by this nozzle.

What essentially happened, is that the nozzles could only penetrate the soil right under their point of impact, without removing any soil due to wall failures. In short, only cavities with a range of $Z_c = 0.5 - 3\ cm$ could be obtained; in which Z_c is inversely proportional to s_u. This made it impossible for the tool to move downwards, remaining in in its starting position. Both this observation as the small amount of soil removed (only from the cavities) resulted in a production that can be considered negligible

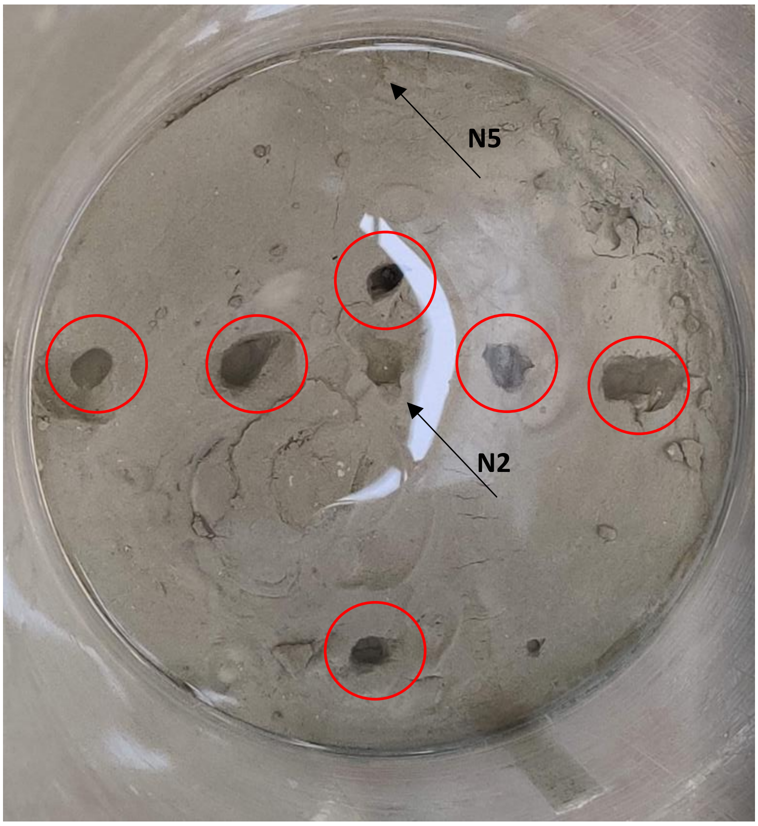

Figure 5-1: Top layer after a static test ($s_u = 60\ kPa, p_j = 30\ bar, D_n = 1.0\ mm$).

5.3 Rotating production

This section is divided into three subsections based on the order in which the experiments were performed in the lab. Each subsection deals with the results obtained for one jet water pressure installation. MP, HP, and LP consecutively.

All graphs addressed in this section describe two datasets belonging to measured values (Cutting and Total) which serve as base data. Derived data (Jetting) was computed from this base data afterwards:

1. Cutting: contribution to the progress rate production exclusively by mechanical excavation. Jets are not operational during these tests.
2. Jetting: contribution to the progress rate production by hydraulic excavation. Calculated value rather than a measured value.
3. Total: combined contribution of cutting and jetting to the overall progress rate production. Jets are operational during these tests.

Both the total production as the production by cutting were obtained during the experiments by either turning the jet water distribution system on or off. The production generated by hydraulic jetting therefore is assumed:

$$v_p(jetting)^4 \approx v_p(total) - v_p(cutting) \tag{5.1}$$

[4] $v_p(jetting)$ describes the vertical progress rate of the tool in $[cm/min]$. This value is NOT equal to the actual jet production (see Chapter 6).

Due to various processes that take place inside the pile, predominantly mixing and suction, the equation given in Eq. 5.1 is not exact. Rather it gives an indication of what the contribution of the jets is.

Finally, two ratios are introduced that play an important role in the theoretical and physical explanation of the processes that take place during the experiments. This involves the Cutting Ratio (CR) and the Jetting Ratio (JR).

$$CR = \frac{v_p(cutting)}{v_p(total)} * 100\% \tag{5.2}$$

$$JR = \frac{v_p(jetting)}{v_p(total)} * 100\% \tag{5.3}$$

For cutting an assumption was made that an increase x times n will result in an (almost) linear increase in progress rate production:

$$x \cdot n \propto x \cdot v_p(cutting) \tag{5.4}$$

This assumption was based on the notion that the cutting energy per unit of time is directly proportional to the (rotational) velocity (Miedema, 2019). Simply put, if you rotate twice as fast, you will loosen twice as much soil by cutting.

Combining both Equations (5.4) and (5.1) results in an increased cutting ratio in the total production hence a decrease in jetting ratio when the rotational speed is increased.

5.3.1 Medium pressure tests

The medium pressure tests were performed at a pressure $p_j = 30\ bar$.

$\boldsymbol{s_u = 20\ kPa}$

The production for a soil with a shear strength $s_u = 20\ kPa$ is given Figure 5-2. As described in Chapter 4, this was one out of two batches in which no data was recorded for $n = 1.5\ rpm$

Nevertheless, still something can be said about the influence of the different excavation methods. One thing that becomes clear is that the total production and thus average vertical velocity of the tool increases with an increase in rotational speed. The same holds for cutting and jetting. For jetting however this increase in production is significantly smaller; 6% compared to 84 % for cutting. This is contrary to what can be expected for the actual jetting production. The relatively low rotational speeds in this study do not affect the cavity depth Z_c that can be obtained by the jets. Therefore, it is assumed that by increasing the rotational speed, Z_c stays constant and the jetting production will increase linearly (Nobel, 2013). This actual production however cannot be measured, as was previously stated. The small increase in progress rate in Figure 5-2 (i.e. small portion of excavated clay) is attributed to the failure mechanism of the soil instead of the jetting process that takes place.

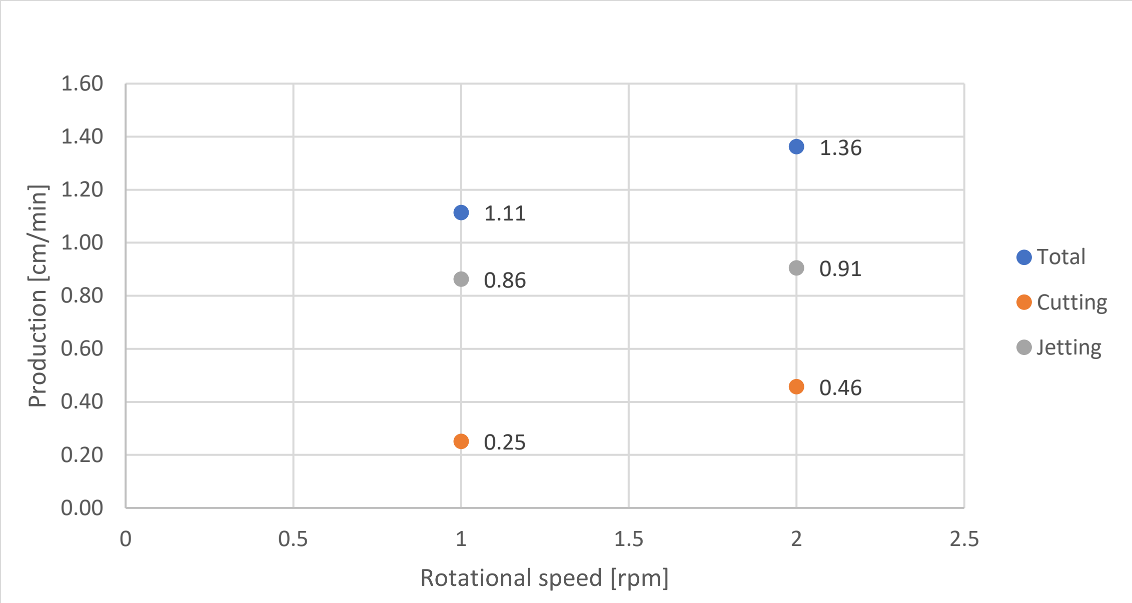

Figure 5-2: Correlation between rotational speed and production for $p_j = 30\ bar$ *and* $s_u = 20\ kPa$

Compared to the other soil strengths discussed in this section, this lower strength soil with $CSR = 23.3\%$ displayed a different physical behaviour. What stood out was not so much the production that could be achieved, but how this production was achieved. After the first rotational test two large ''pits'' were formed at the wall of the pile that gradually decrease. The least deep pit extended from the horizontal surface to a depth of $4.5\ cm$. The deepest pit had a range leading up to a maximum depth of $7.5\ cm$. An additional smaller pit with a uniform depth of $1\ cm$ was formed around the centre. These distinctive features, only observed for the aforementioned CSR are given in Figure 5-3 and 5-4.

Figure 5-3: Top view of clay surface

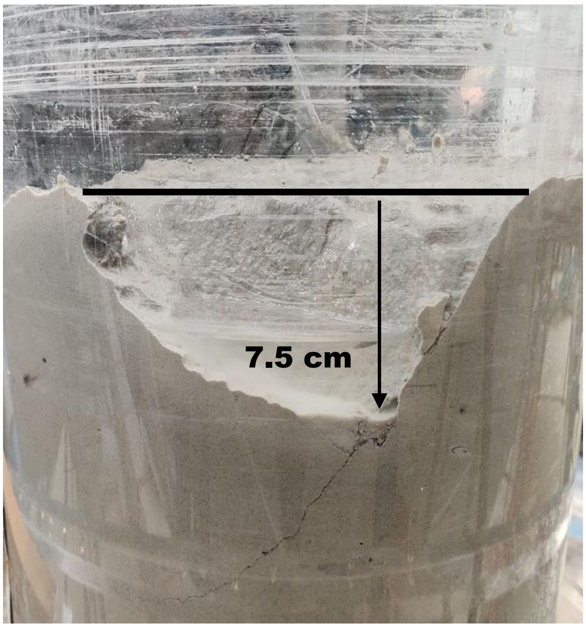

Figure 5-4: Side view of clay column

In Figure 5-4 another fracture line was already observed underneath the initial cut. The only reason this volume of clay was not removed prior, is of the weight of the soil that was still present at both sides of the gap.

$s_u = 60\ kPa$

The production for a soil with a shear strength $s_u = 60\ kPa$ is given Figure 5-5. This graph is noticeable different to the one given in Figure 5-2. This clay is 3 times stronger than the softest clay used in this study and has a $CSR = 56.7\%$.

The dataset for cutting displays the same trend as derived from Eq. 5.2; a nearly linear gradient. For all three datapoints given here the CR is proportional to the rotational speed, while JR is inversely proportional to the rotational speed. This holds true throughout the entirety of this study.

Another trend that can observed, related to both cutting and jetting has to do with the undrained shear strength. Increasing the shear strength while keeping other operational parameters constant (p_j and n) will lead to a higher CR and a lower JR. A more thorough explanation is given in Section 5.4.

Even though, the absolute values of the progress rate of the tool decrease with an increase in soil strength and given that for a single rotational speed the datapoints lie much closer to one another a new phenomenon occurs.

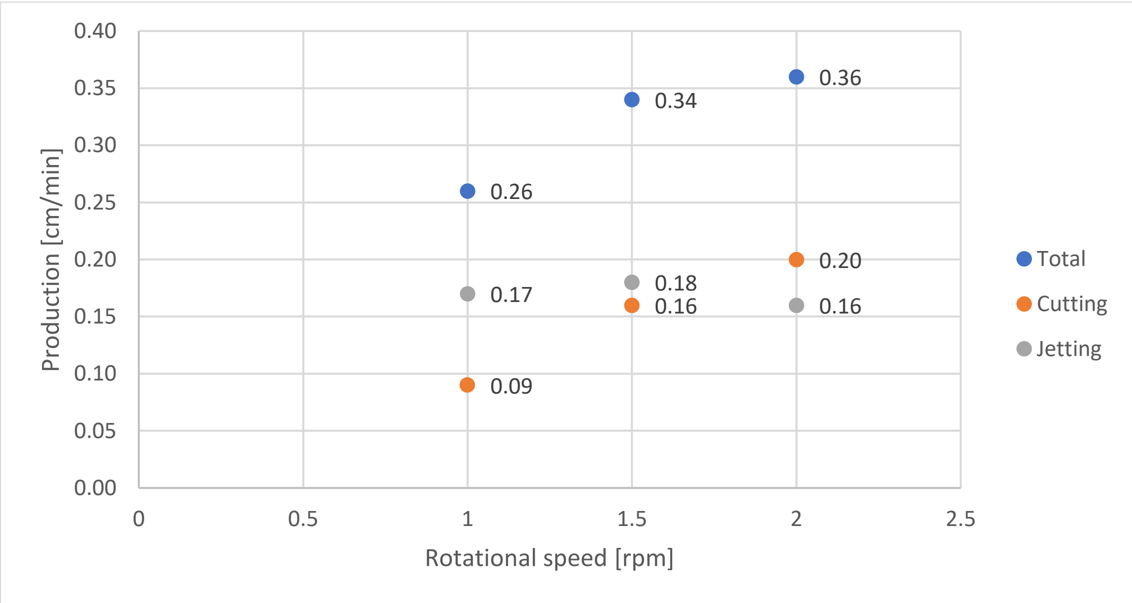

Figure 5-5: Correlation between rotational speed and production for $p_j = 30\ bar$ and $s_u = 60\ kPa$

$s_u = 100\ kPa$

The production for a soil with a shear strength $s_u = 100\ kPa$ is given Figure 5-6. As described in Chapter 4, this was one out of two batches in which no data was recorded for $n = 1.5\ rpm$.

Applying a jetting tool to this soil plug hardly led to any production. The jets were unable to penetrate the soil to such an extent that production by jetting was almost impossible. The mixture that was developed and on which tests were performed is given in Figure 5-7. This figure displays the soil plug right before the start of the first test. This mixture was very brittle and non-plastic. The most obvious explanation for this occurrence is the applied value of $CSR = 83.3\%$.

The relatively small amount of bentonite in comparison to the overwhelming quantity of cement, gives rise to properties that closely resemble that of concrete rather than a stiff clay.

During testing of the lower strength clays, it was always feasible to form a circular trench by jetting that would later collapse under a combination of gravity (i.e. weight of the tool) and the abrasion going on due to cutting. In this case however, the top layer of the clay mixture was only ''engraved'' so to speak, as indicated in Figure 5-8. This will be further elaborated upon in Chapter 6.

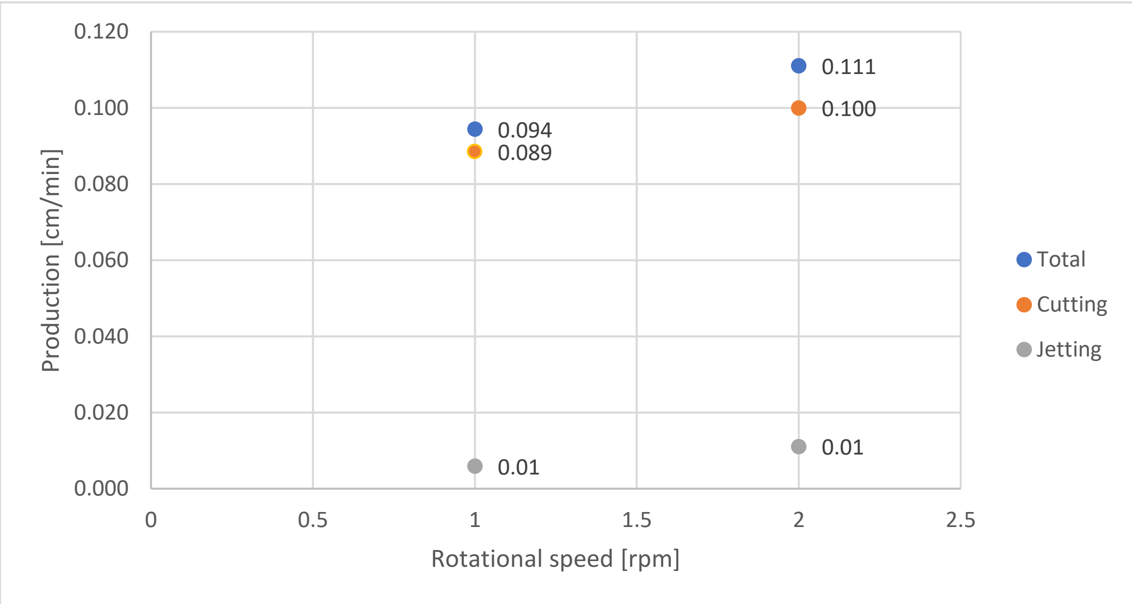

Figure 5-6: Correlation between rotational speed and production for $p_j = 30\ bar$ and $s_u = 100\ kPa$

In line with the discussion above about ratios (see Table 5-1), the value for JR is almost negligible. The production by cutting has a contribution to the total production in the range of $CR = 90 - 94\%$. Since jetting production is not measured separately (see explanation Eq. 5.1) the present range of $JR = 6 - 10\ \%$ can be explained as follows: it is not necessarily soil loosened by the jets, rather mechanically excavated soil parts in suspension that are assisted by the water jets towards the suction pipe.

Figure 5-7: Top view of soil plug at $t = 0$

Figure 5-8: Top view of ''engraved'' stiff clay

Combined

An overview of the total production for different soil strengths for MP tests is given in Figure 5-9. This graph clearly shows the fast decay in production levels between lowest strength and medium strength clay.

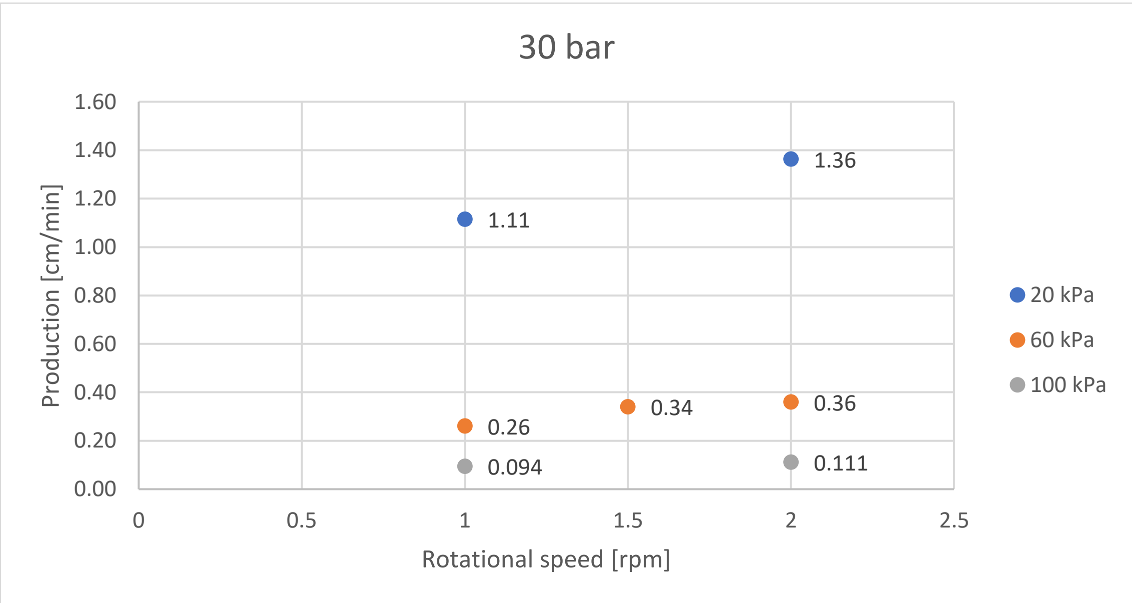

Figure 5-9: Correlation between rotational speed and production for $p_j = 30\ bar$

5.3.2 High pressure tests

The high-pressure tests were performed at a pressure $p_j = 130\ bar$

$\boldsymbol{s_u = 20\ kPa}$

The production for a soil with a shear strength $s_u = 20\ kPa$ is given Figure 5-10. It is clear from the method described in the previous subsection, that one dataset should remain constant. This is the dataset containing the values for cutting production. This is in fact the only dataset in which no parameters were altered compared to the MP tests from Subsection 5.3.1. These datasets served as a first step towards reproducibility testing.

Comparing Figure 5-10 and 5-2, the ranges in which the cutting production falls are the same for both MP and HP. An additional benefit of repeating all the cutting tests is the acquirement of missing datapoints as encountered in the previous subsection.

One important point that could be taken out of this graph is the increase in jetting production while increasing p_j and keeping all other parameters the same (s_u and n). A more detailed explanation is given in Section 5.4.

Another parameter that needs to be kept constant in order to quantify the effect of jet pressure is the jet momentum I_o. The reason for this is that the production is affected by the flow rate (i.e. nozzle discharge) and the flow velocity (i.e. exit velocity), see Eq. 2.20. This study specifically deals with the momentum flux that describes the rate of transfer of momentum across an area (i.e. nozzle area).

Nevertheless, by reducing the flow rate with more than 50% and increasing the exit velocity substantially the effect on the amount of soil excavated due to jetting is $1.6 - 2.8$ times bigger than was the case for a MP system.

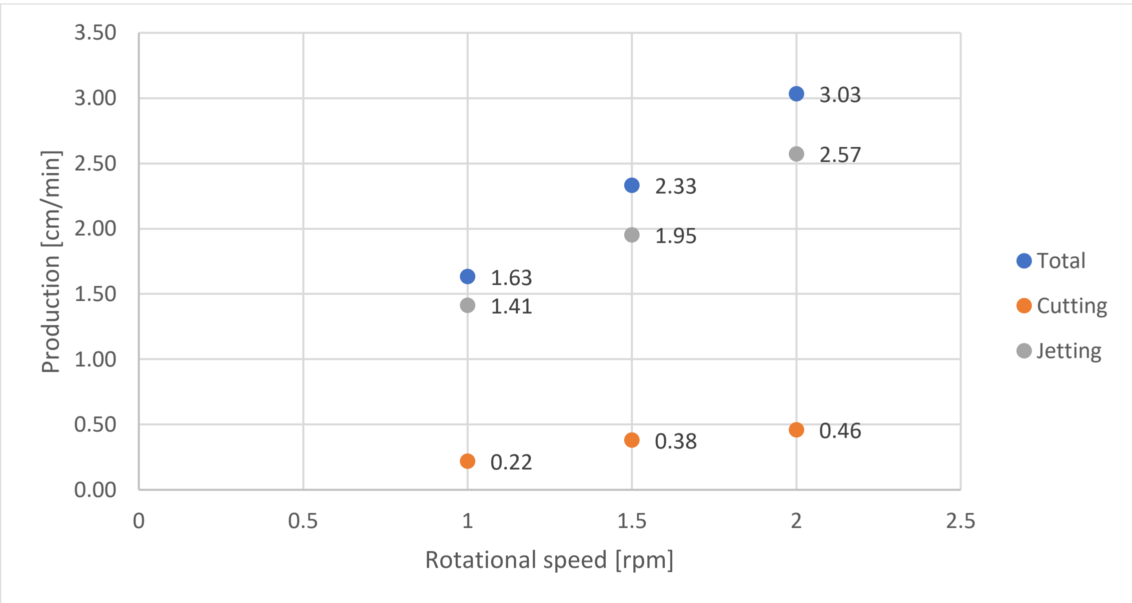

Figure 5-10: Correlation between rotational speed and production for $p_j = 130\ bar$ and $s_u = 20\ kPa$

The exit velocity in particular contributes to this faster excavation that was observed here. Figure 5-11 gives an idea of what was discussed above. The highly irregular surface seen here was obtained after a rotating test. Different pits, broken trenches, large lumps and small fragments of clay are scattered over the entire surface. The deepest sections encountered near the centre as across the wall have depths ranging from $2 - 3\ cm$.

Figure 5-11: Top view after rotating test ($n = 1.5\ rpm$)

Figure 5-12: Side view of the pile

Another detail is revealed from Figure 5-12. Presumably because of the more concentrated jet (smaller D_n) and the higher exit velocities through the nozzle plus taking into account that this concerns the softest clay type, a sort of settling mechanism (as seen in granular materials like sand) can be observed right after a test was finished. It took roughly $3 - 4\ min$ for all ''particles'' to settle. This was the only batch in which this phenomenon occurred.

$s_u = 60\ kPa$

The production for a soil with a shear strength $s_u = 60\ kPa$ is given Figure 5-13. The trends found in this graph are nearly identical to the ones encountered for $s_u = 20\ kPa$. A big difference with respect to the MP tests are CR values which stay nearly constant, while increasing the shear strength from $20\ kPa$ to $60\ kPa$. In other words, the influence of jetting does not decrease with an increase in shear strength. This can be contributed to the increase in exit velocity as was described above.

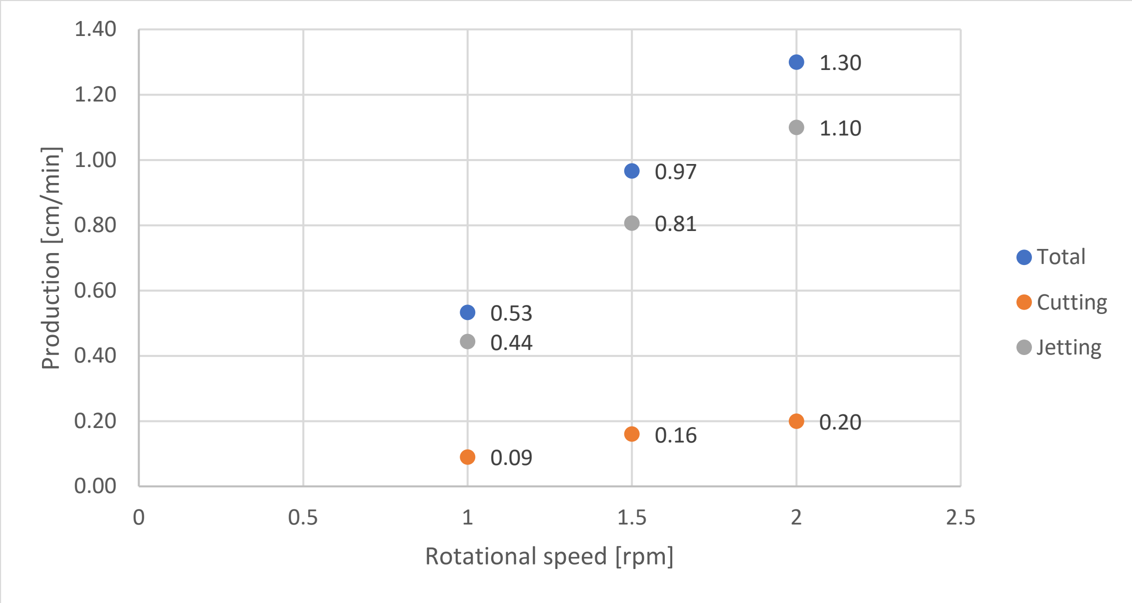

Figure 5-13: Correlation between rotational speed and production for $p_j = 130\ bar$ *and* $s_u = 60\ kPa$

Next to the delivered production determined with measuring tape, another method of comparing the different test setups is by looking into the chunks of clay that are excavated by nozzle $N5$ (the nozzle directed outwards in the direction of the wall). This nozzle was essential to the purpose of getting a better understanding about the processes that place inside the pile through a simple observation. The other nozzles were not visible during testing due to the nature an orientation of the jetting head on top of the soil plug. This distinction can easily be made based on a video recording.

$s_u = 100\ kPa$

The production for a soil with a shear strength $s_u = 100\ kPa$ is given Figure 5-14. As was the case for MP, now too $CR > JR$. Most of the clay excavated is due to the cutting that takes place and not so much due to jetting. Although jetting cannot be neglected entirely in this case. As discussed before, the jets tend to ''engrave'' the top layer without penetrating it. This is only partially right for HP. The outer ring of nozzles was not able to penetrate the soil and therefore return the same engraved surface as in Figure 5-8. The inner nozzles however did penetrate the soil. This seems to not add up. A reason could be an increased effect of the suction inlet near the centre. Another more understandable explanation could be presence of fracture lines that started expanding once the tool was lowered and/or jets were initiated.

Figure 5-15 sees the top view of the mentioned batch. The depth of pipe around the suction inlet is $3\ cm$. A large lump of clay can also be seen located inside the pit. This lump certainly was broken off somewhere near the centre. After all, there are no holes/pits across the surface, rather than around the centre. This lump measure $6 \cdot 4\ cm$. This could confirm the initial reasoning of existing fracture lines in materials as brittle as this stiff clay.

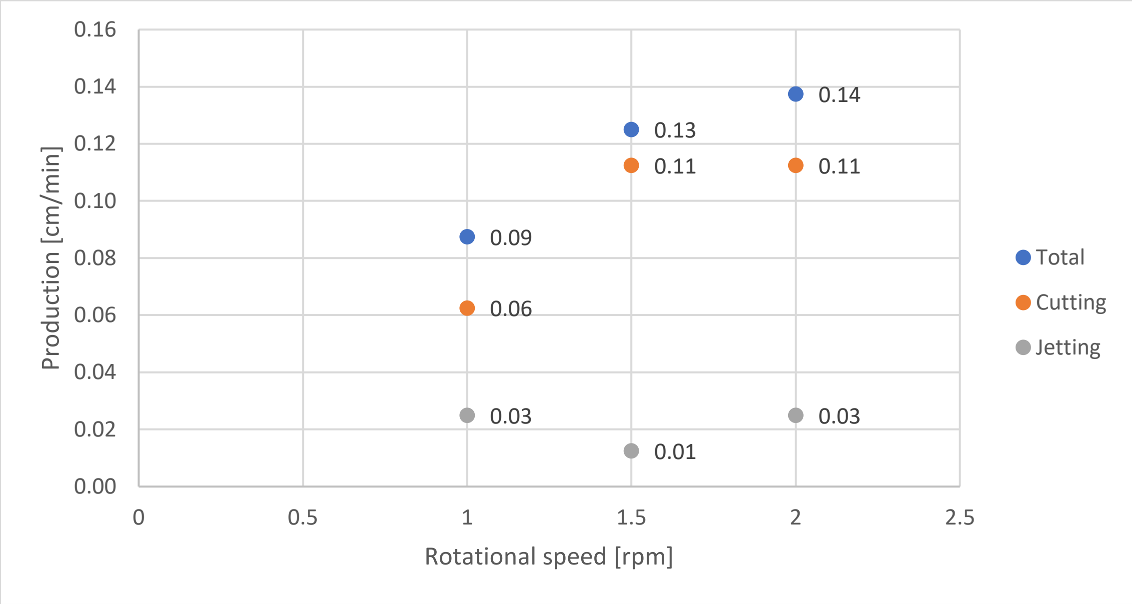

Figure 5-14: Correlation between rotational speed and production for $p_j = 130\ bar$ and $s_u = 100\ kPa$

Figure 5-15: Top view of most stiff clay, partially engraved and partially trenched

Combined

An overview of the total production for different soil strengths for HP tests is given in Figure 5-16. This graph clearly shows the fast decay in production levels between lowest strength and medium strength clay.

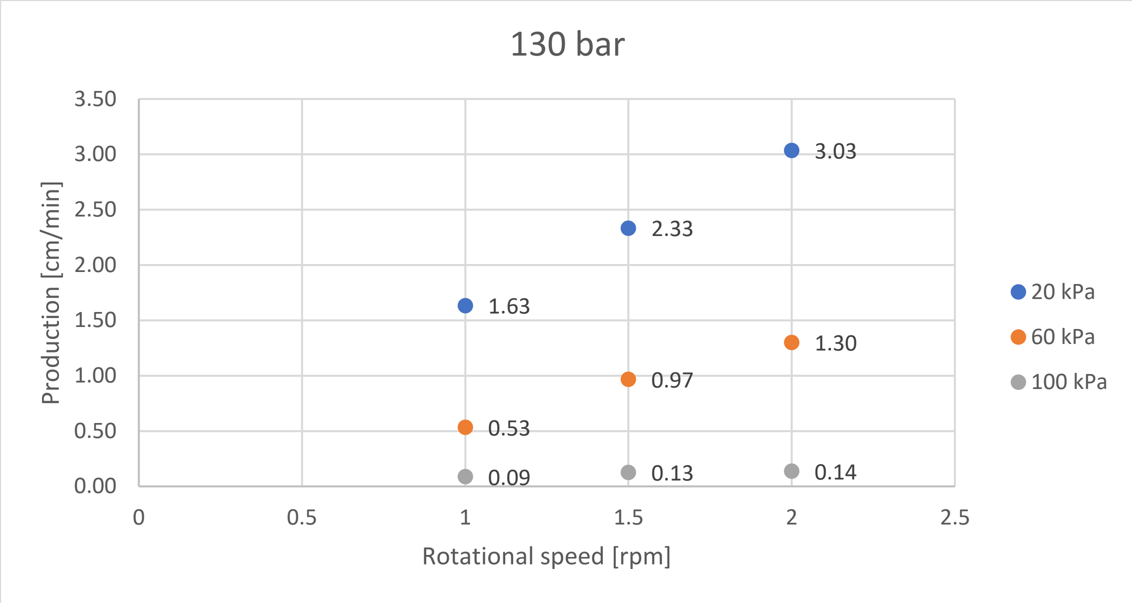

Figure 5-16: Correlation between rotational speed and production for $p_j = 130\ bar$

5.3.3 Low pressure tests

The low-pressure tests were performed at a pressure $p_j = 3\ bar$. First a batch of medium strength clay was prepared for the experiments carried out with LP test setup. This approach led to dropping the high strength clay (i.e. $s_u = 100\ kPa$) experiments out of this study. Eventually only low strength clays were added to the mix.

$\boldsymbol{s_u = 20\ kPa}$

The production for a soil with a shear strength $s_u = 20\ kPa$ is given in Figure 5-17. Compared to MP and HP testing the cutting production is totally different.

There is a structural difference in the tool used for LP (besides jet distribution system). In Figure 3-20 a wooden disk was introduced and mounted on top of the jetting head to protect the nozzles from physically interacting with the soil underneath. Hence resulting in an $SOD = 15\ mm$. For LP, a simple jet water distribution system was designed and installed. This could be done without needing special nozzle mounts; therefore, it was possible to place the nozzles exactly level with the slot openings, constraining the nozzles inside the plate work. Effectively removing the wooden disk for the LP experiments and realising an $SOD = 0\ cm$. The only part of the tool that comes in direct contact with the clay layer is the smooth bottom plate made of steel.

This difference in material used (robust wooden disk vs. smooth steel plate) resulted in lower cutting production values as given in Figure 5-17.

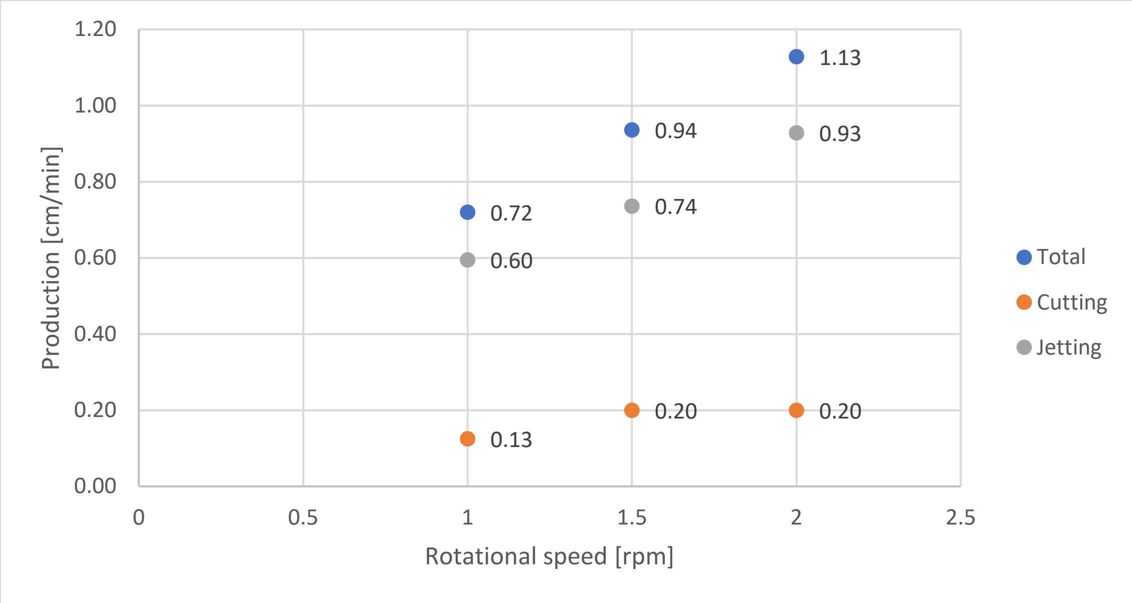

Figure 5-17: Correlation between rotational speed and production for $p_j = 3\ bar$ *and* $s_u = 20\ kPa$

The total and jetting production follow the same linear trend as was encountered for MP and HP. The absolute vales, on the other hand, are lower for this jetting head. Already something can be said about which trend is expected for a varying jet pressure, see Subsection 5.4.2.

$s_u = 60\ kPa$

The production for a soil with a shear strength $s_u = 60\ kPa$ is given Figure 5-18. Comparing these results with the ones given for MP and HP, clearly shows in the amount of soil that was excavated. Keeping in mind the already low to very low jetting production levels encountered in the previous subsections it was not convenient to further investigate a very stiff clay (i.e. $100\ kPa$) under these new circumstances.

The trends in this graph nearly all correspond to the trends as given for the HP system, which is the other extreme present in this study. There is a striking resemblance for both ratio factors as for the (inverse) proportionality between production and rotational speed (assuming $s_u = constant = 60\ kPa$).

Another clear observation is the difference in absolute values for cutting production. In the previous subsections these values were nearly identical for MP and HP, as they should be since jetting is excluded from these experiments. For the LP however a different jet distribution system was attached to the jetting head. The previous system was only suitable for MP and HP. The jetting tool therefore had to be converted to resemble a low-pressure SPRT system like the inhouse tool from *Boskalis*, see Table 1-1.

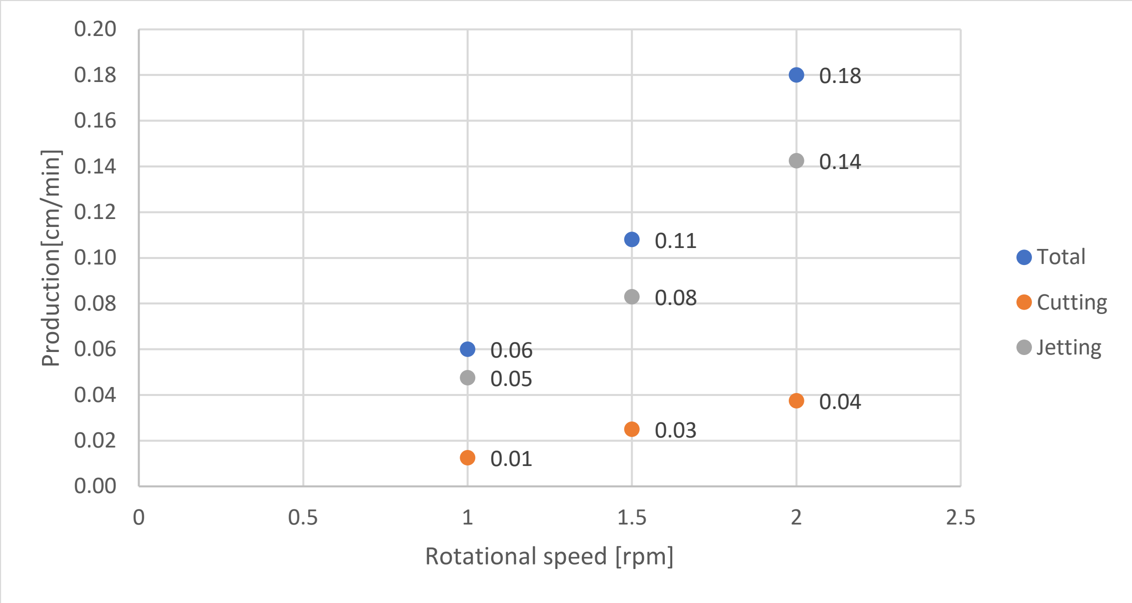

Figure 5-18: Correlation between rotational speed and production for $p_j = 3\ bar$ *and* $s_u = 60\ kPa$

Combined

An overview of the total production for different soil strengths for LP tests is given in Figure 5-19.

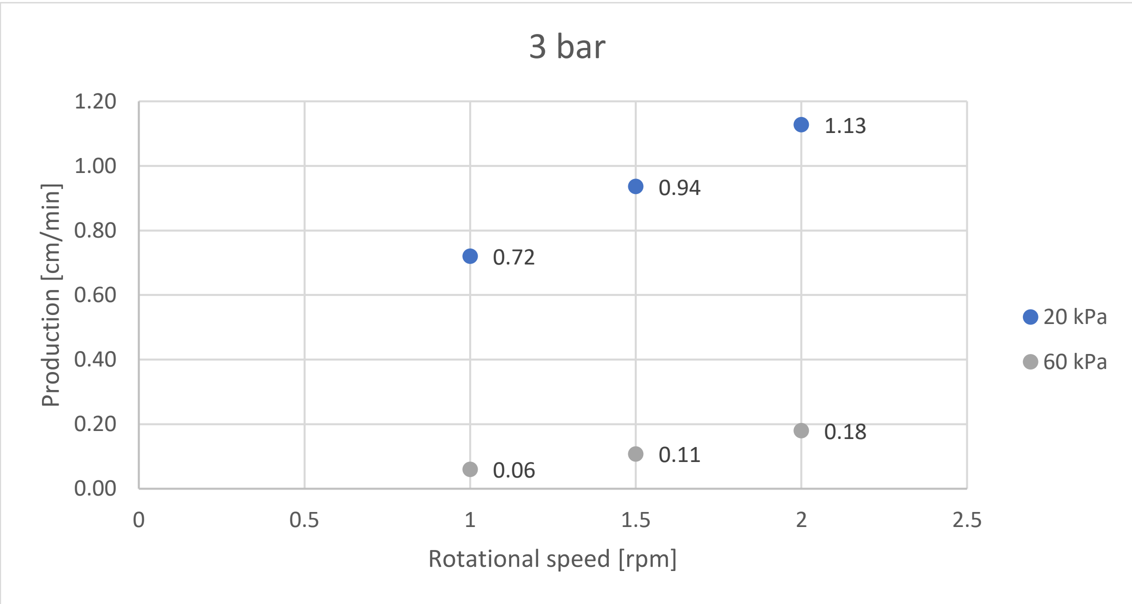

Figure 5-19: Correlation between rotational speed and total production for $p_j = 3\ bar$

5.4 Influence of shear strength and jet pressure

This section discusses the influence of the shear strength and jet pressure. The production in terms of progress rate is set out as a function of either one of these parameters, in the same way as was done for the rotational production in Section 5.3. The results mentioned in this section are given for one rotational speed, namely $n = 2\ rpm$.

5.4.1 Undrained shear strength

The effect of the undrained shear strength is given in Figure 5-20. The progress rate production for all jet pressures drops when s_u is increased. Another observation that follows from this figure is that the absolute difference in production measured at one s_u becomes smaller for each increase in shear strength to the point that it is almost equal for $s_u = 100\ kPa$ once the shear strength is increased.

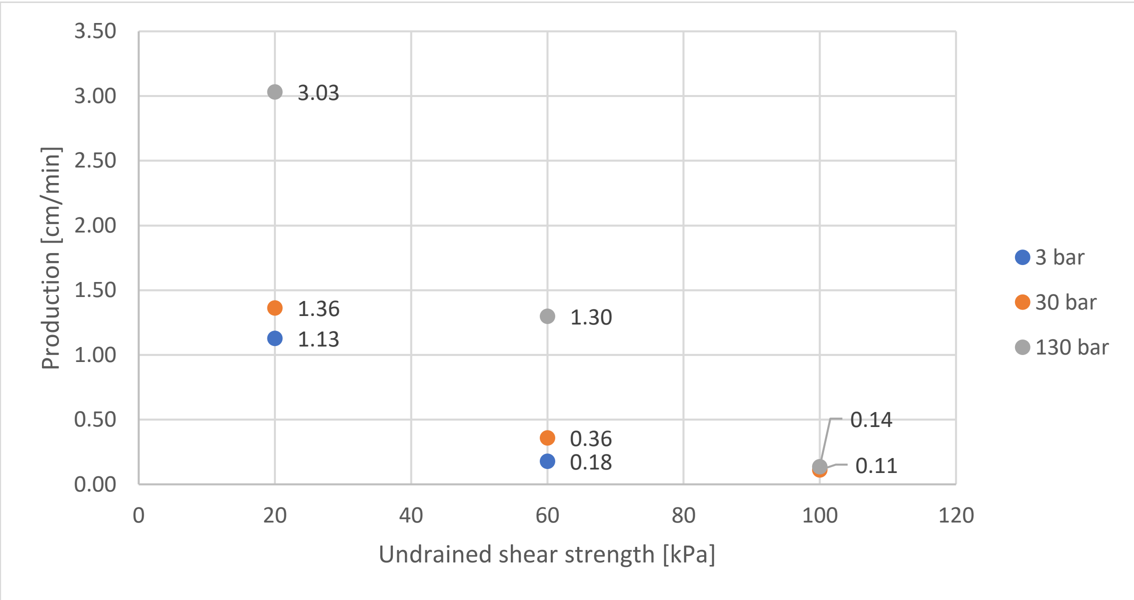

Figure 5-20: Correlation between undrained shear strength and total production at $n = 2\ rpm$.

This graph however does not indicate what part of the total production is due to cutting or jetting. The absolute values were already given across the figures in Section 5.3. Plotting these values in Figure 5-20 would have made the graph confusing and hard to interpret. For this reason, Figure 5-21 is added in which CR and JR are plotted against s_u. This way also insight into additional information is given that cannot be seen from the absolute values. The values were only plotted for $p_j = 30\ bar$ and $p_j = 130\ bar$. The dataset for $p_j = 3\ bar$ is missing the values for $s_u = 100\ kPa$ and on top of that cannot be compared to the other datasets due to different setup of the jetting head (see Chapter 3).

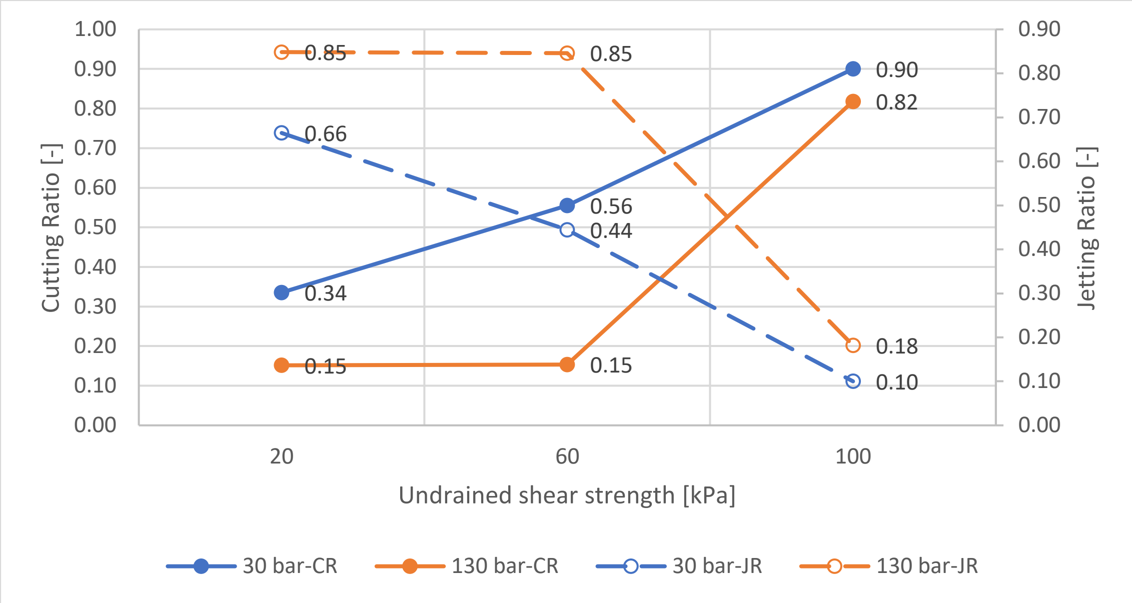

Figure 5-21: Correlation between undrained shear strength and CR & JR at $n = 2\ rpm$.

For $s_u = 20\ kPa$ and $s_u = 60\ kPa$ at $p_j = 130\ bar$ more than half of the production can be related to jetting. The ratios are the same for these shear strengths (absolute values are not). After a gradual rise CR becomes larger than JR for $s_u = 100\ kPa$. In other words, the influence of the jets is significantly reduced at higher shear strengths. Since only three shear strengths and rotational speeds were implemented in this research it is impossible to determine the exact tipping point. For $p_j = 30\ bar$ for instance, this tipping point is already reached before $s_u = 60\ kPa$. Nevertheless, the following relations can be determined with almost full certainty, see Table 5-4.

Table 5-1: CR and JR relation depending on s_u

$s_u\ (kPa)$	Relation $(-)$
$\ll 60$	$CR < JR$
$\gg 60$	$CR > JR$

As regards to the constant values for JR and CR for the two lowest shear strengths; this cannot be considered an undisputed fact rather a coincidence. It is clear however, see provided data in Appendix C, that any difference arising between these ratios for the lower shear strength is relatively small, compared to the same ratios corresponding to the largest shear strength.

5.4.2 Jet pressure

The influence of the jet pressure is displayed in Figure 5-22. It can be seen immediately that all forms of production are directly proportional to jet pressure. Furthermore, a larger amount of production is generated for the softest clays under the same jet regime. This trend is particularly distinctive for $p_j = 130\ bar$. Yet again, for $s_u = 100\ kPa$ the differences are relatively small. Increasing the jet pressure more than 4 times will only lead to a difference of $0.03\ cm/min$.

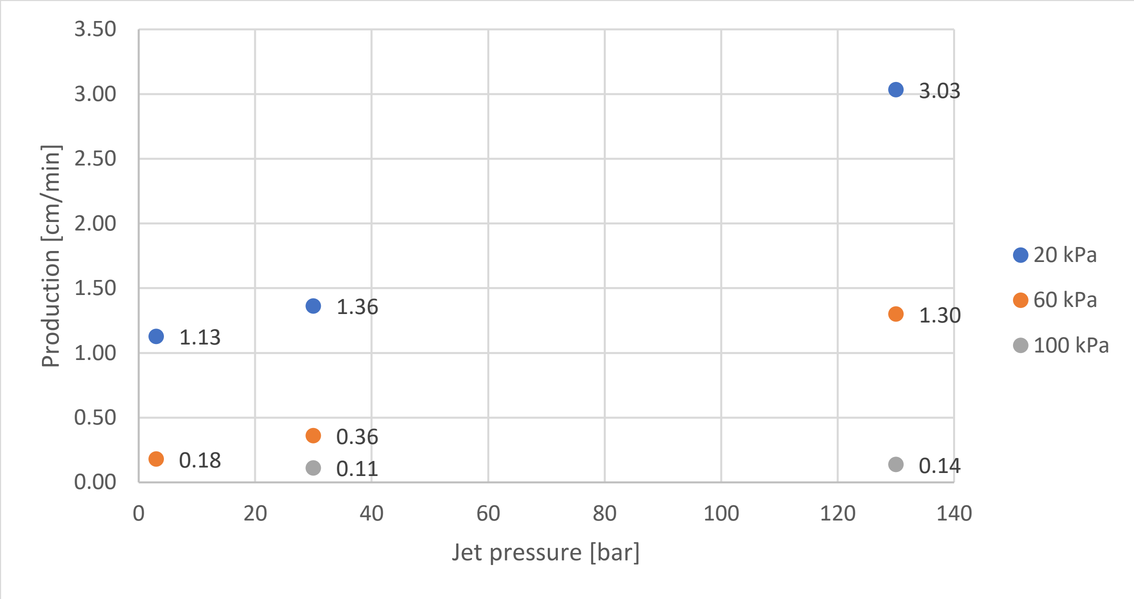

Figure 5-22: Correlation between jet pressure and total production at $n = 2\ rpm$.

There is a contribution of jetting to the values given in Figure 5-22. This is not the case for cutting production, because cutting is not a function of jet pressure. As explained at the beginning of this chapter, the datasets belonging to cutting production are obtained by turning the jet water distribution system off and hence jet pressure is not measured. In order to say something about the influence of jetting, the cutting production must be constant for changing p_j while keeping s_u and n constant (see Table 5-2).

Table 5-2: cutting production for MP&HP for $n = 2\ rpm$

	$\boldsymbol{Shear\ strength\ (kPa)}$		
$\boldsymbol{Jet\ pressure\ (bar)}$	**20**	**60**	**100**
30	0.46	0.20	0.10
130	0.46	0.20	0.11

It is clear that the absolute values for the cutting production for the MP and HP pump system stay constant while p_j is altered, as was expected. The normalised values for jetting production are given in Figure 5-23.

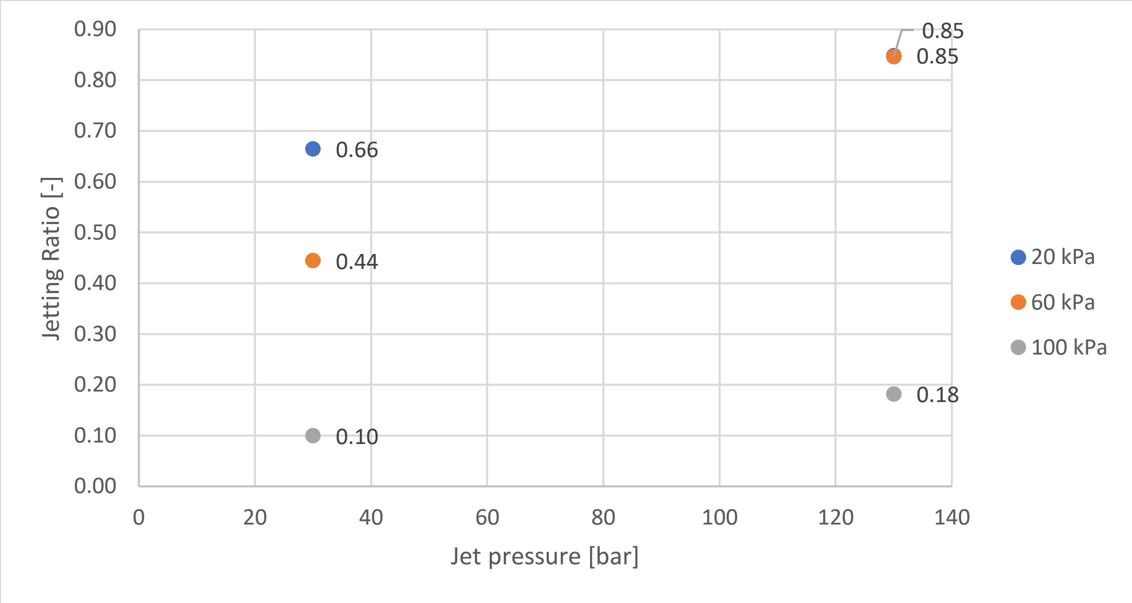

Figure 5-23: Correlation between jet pressure JR at $n = 2\ rpm$ *for* $p_j = 30\ bar$ *and* $p_j = 130\ bar$.

The JR increases proportionally with the jetting pressure. Although this is true for all values given in this graph, there is a noticeable deviation from the expected trend. For $p_j = 130\ bar$ the share of JR is equal for $s_u = 60\ kPa$ and $s_u = 100\ kPa$. This was already encountered in Figure 5-21 and is further elaborated upon in the analysis in Chapter 6.

5.5 Other results

5.5.1 Stepwise rotation

In dredging practice, the jetting head is either static or rotating while it is operating. The tool developed by *Claxton* is listed as static. This is in fact only true while it is jetting a particular part of the clay. The tool is not operated continuously, rather it jets one part, is turned off, rotated by 30° and then turned on again to jet the next segment. This process is repeated in the same incremental steps of 30° until a full rotation is made. This sequence is added to the experiments that were carried out and to distinguish it from the continuously rotating concepts employed by *Deco* and *Deep C* it is listed as stepwise rotation.

In the end three datasets were obtained, each one corresponding to a specific jet pressure system. The production by stepwise rotation is plotted against the undrained shear strength, see Figure 5-24.

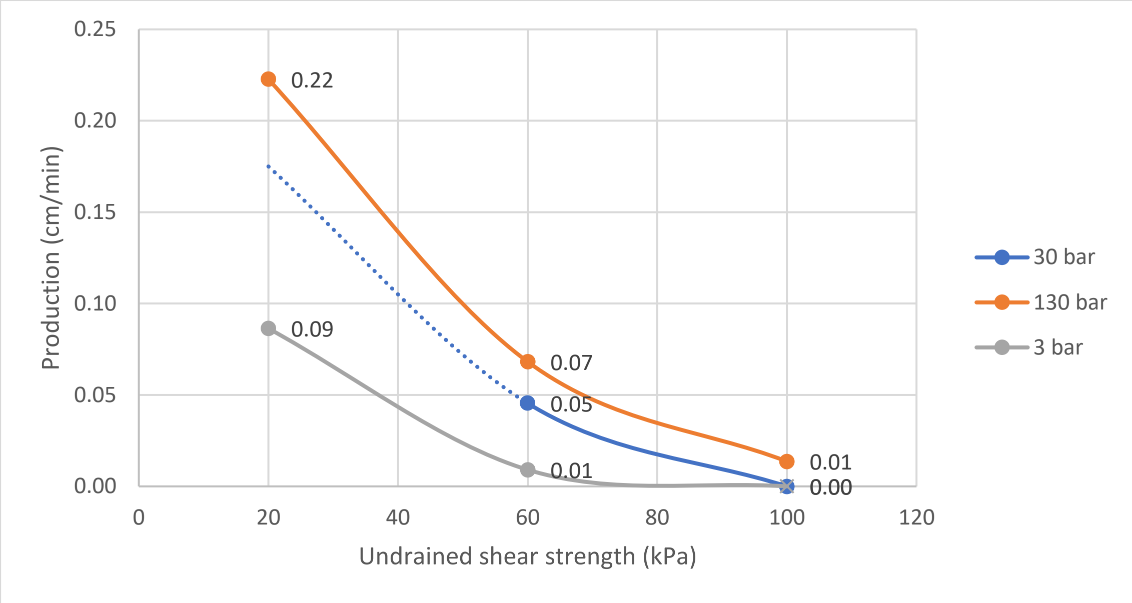

Figure 5-24: Correlation between stepwise production and undrained shear strength for LP, MP and HP.

Reading the graph from left to right a negative exponential trend can be discovered. Two datapoints were missing in this study. As mentioned in Subsection 5.3.3 no LP tests were performed on the stiff clay. A production of $0{,}00\ cm/min$ was assumed for LP at $s_u = 100\ kPa$. This assumption is based on the other datapoints presented here that are related to the same shear strength and also due to the nature of the experiments performed for stepwise rotation (production is higher compared to the static case, but lower than for the continuous rotating case).

The other datapoint for which no data was returned during the test phase is for the MP tests on soft clay and marked with a dotted line that follows the same trend as given by the HP test. This was assumed since the first part of the line between 60 and $100\ kPa$ already follows the same trend and on top of that MP and HP use the same jet water distribution system. Considering all the other data, an error margin of $\sim 14\%$ must be applied to the dotted line (based on the average of the extremes present in this graph).

5.5.2 Set down pressure

The jetting tool is supposed to rest on top of the clay layer and will move downwards based on gravity while being secured inside a guiding frame. Alongside the parameters that were discussed prior to this discussion, the effect of the pressure exerted by the pile on the soil while in operation should also contribute to the production that can be achieved during excavation. The following plan was set in motion to define this effect:

1. This test could only be performed by at least two people
2. Person 1 controls the crane remote and keeps a close eye on the real-life date returned by the loadcells that measure the weight of the pile and its contents. Based on this data the crane should be either lifted or lowered using the crane
3. Person 2 takes on the remaining proceedings that need to be followed during a test (see Appendix D). Reliable data can only be obtained by keeping the water content inside the pile at a constant level. Person 2 performs this task by making sure that a steady supply of water is guaranteed using the overflow of the pile.

Once the pile was totally filled with water the mass of the tool m_T was determined as follows:

$$\begin{aligned} m_T &= m_{total} - m_{pile+c} \\ &\approx \ 125 \ - \ 75 \\ &\approx \ 50\,kg \end{aligned} \tag{5.5}$$

In which m_{total} is the total mass present on top of the loadcells (pile, clay column, water column and jetting tool) and m_{pile+c} is the combined mass of the pile and its contents (i.e. clay and water).

This means that the tool can add a maximum of $50\ kg$ to the setup if fully submerged and rested on top of the bed. In this test the decision was made to perform measurements with a value of $0.3 \cdot m_T \approx 15\ kg$. The total mass that should be kept constant can now be determined by Eq. 5.5 and returned a value of $m_{total} \approx 90\ kg$ (reading from loadcell logging and anticipating on fluctuations due to excavated material that is continuously removed from the pile).

This test was caried out for a clay with $s_u = 60\ kPa, p_j = 130\ bar$ at $n = 2\ rpm$. This test is compared to a test in which all parameters were kept constant except the set down pressure. The results are given in Table 5-3.

Table 5-3: Effect of set down pressure on production for $s_u = 60\ kPa$

$Test$	$m_T\ (kg)$	$Set\ down\ pressure\ (kPa)$	$Production\ (cm/min)$
1	50	8.57	0.48
2	15	2.57	0.07

Unfortunately, this was the only set down pressure test that was completed during testing. A lot of time was needed to perform all the other tests on a single batch of clay. Add to this all the peripheral work for the large test setup, made it not feasible. Especially if a helping hand is not available at that moment.

Nevertheless, the results in Table 5-3 give insight in the fact that set down pressure offers a big contribution to the production. Reducing this value automatically will also reduce the production that can be achieved. It is assumed that especially the loss in friction force between jetting head and clay layer will reduce the cutting production and thus the total production. Hence,

$$Production = f\ (set\ down\ pressure) \tag{5.6}$$

5.5.3 Moving nozzle – single water jet

The available tools on the market were introduced in Table 1-1. The *Deco* tool employs a mechanism in which the nozzles can move and rotate around their own axis. This mechanism was eventually not implemented in the designed jetting tool due to a lack of space inside the pile and the overcomplication it would give to the design. This was solved by performing a test using the spray lance of the high-pressure pump inside the pile.

After completing all relevant tests from the test matrix on a given batch of $s_u = 60\ kPa$ clay, still some material needed to be removed in order to clean the pile afterwards. This remaining clay column with a height $H_{clay} = 17.9\ cm$ was brought in suspension with the spray lance by rotating the nozzle and pushing it back and forth until all material was observed to be in suspension. The high-pressure pump was set to a pressure $p_{HPP} = 30\ bar$. It eventually took only $t = 3\ min$ to perform this task. This is translated to a production in cm/min to be able to compare it with the test as examined in Section 5.3, see Table 5-4.

Table 5-4: Production of a moving nozzle with $s_u = 60\ kPa$ and $p_{HPP} = 30\ bar$

$Test$	$Q_{pump}\ (l/min)$	$Production\ (cm/min)$
$Standard$	15.2	$0.5 \leq$
$Moving\ nozzle$	~ 10	6.0

A lot of assumptions were made in order to compare the standard tests with the test performed using a single jet moving nozzle. Even though the production for the moving nozzle is more than 12 times larger than the values encountered for the standard tests with the jetting tool it is likely to be even higher.

While the production for the standard tests was obtained by interpreting the difference in progress rate of the jetting tool, the test that was carried out with the moving nozzle (i.e. spray lance) did not involve any set down pressure, suction or efficient nozzle configuration.

Additionally, rather than removing the resulting slurry (suction pipe is integral part of the jetting tool) the column of clay was deemed fully removed when all the clay was in suspension. By not removing the developed mixture in the pile the suspension process is influenced by the remaining slurry hence takes longer than would be expected.

6 Analysis

6.1 Soil failure processes

This section gives an overview of all processes that play a role in progress rate production as given in Chapter 5. Mixture forming processes are challenging to study due the multitude of processes occurring simultaneously. This should be kept in mind when analysing individual processes and their effect on the production.

6.1.1 Normalised stagnation pressure

A dimensionless number is introduced to give better insight into the processes that take place. The normalized jet pressure p_j/s_u says something about the failure mode that can be expected. This holds true, because of the relatively small stand off distances SOD encountered in this study. Nevertheless, there is a difference in SOD between LP on the one hand and MP&HP on the other hand. This non-negligible difference stems from the fact that for MP&HP a wooden disk is added to the tool (see Section 3.6), which is not the case for LP. For the LP system the nozzles are exactly level with the slot openings, constraining the nozzles inside the plate work and effectively obtaining $SOD = 0\ mm$. Therefore $u_s \approx u_0$ and according to Eq. 2.27 $p_{stag} \approx p_j$. Table 6-1 gives an overview of all normalized jet pressure values encountered in this study.

Table 6-1: values for the jet ratio p_j/su

	$\boldsymbol{Jet\ pressure\ (bar)}$		
$\boldsymbol{s_u(kPa)}$	**3**	**30**	**130**
20	15	150	650
60	5	50	217
100	–	30	130

The assumption that the stagnation pressure equals the jet pressure does not hold for the MP&HP system due to the encountered $SOD_{MP\&HP} = 15\ mm$. For a non-cavitating jet, the stagnation pressure in the centre equals the jet pressure only up to a jet distance of $\sim 6.2D_n$. Simply put, the jet must travel a larger distance in ambient water before it interacts with the clay. This causes $u_s < u_0$ and $p_{stag} \neq p_j$ for MP&HP. In order to truly compare the two systems to each other the values in Table 6-1 need to be corrected for this difference in SOD by introducing the normalized stagnation pressure p_{stag}/s_u.

The stagnation pressure can be determined according to Eq. 2.27 for a non-cavitating jet and Eq. 2.32 for cavitating jets. To determine for which experiments in the present study conditions of cavitation occurred, results obtained in an experimental set-up designed by (Nobel, 2013) were examined and listed in Table 6-2. These tests were performed at an ambient pressure $p_{a0} = 1.3\ bar$ and at a jet distance $s = 12\ D_n$.

Table 6-2: Jet pressure for cavitation cone development and the corresponding cavitation number for the three nozzle diameters ($p_{a0} = 1.3\ bar, s = 12\ D_n$).

$D_n\ \ (mm)$	$p_{cav}\ \ (bar)$	$\sigma_d\ \ (-)$
7	20	0.065
5	24	0.054
3	26	0.050

The experiments in the present study were performed under slightly different circumstances. The nozzles used were smaller and jet distances were either a factor larger or smaller. All mentioned parameters are given in Table 6-3. All tests were caried out at an initial ambient pressure between $p_{a0} = 1.0 - 1.1\ bar$. The values for p_{cav} were determined by extrapolating the values as given in Table 6-2 and by introducing the following properties based on trends that link a change in a specific parameter to a change in p_{cav}.

1. p_{cav} increases with a decrease in D_n
2. p_{cav} decreases with a decrease in p_{ao}
3. p_{cav} decreases with an increase in s

Table 6-3: Jet pressure for cavitation cone development and cavitation occurrence ($p_{a0} = 1.0 - 1.1\ bar$).

$Pump\ system$	$D_n\ \ (mm)$	$SOD\ (mm)$	$p_j\ \ (bar)$	$\sim p_{cav}\ \ (-)$	$p_j > p_{cav}$
LP	2.3	$0D_n$	3	> 26	NO
MP	1.0	$15D_n$	30	$28 \leq$	YES
HP	0.5	$30D_n$	130	$26 - 30$	YES

The first mentioned trend is essentially already seen in Table 6-2, and thus part of the mentioned extrapolation. Taking the two other trends into account, the possible ranges for p_{cav} are given in Table 6-3. Cavitation occurs when the jet pressure exceeds the jet pressure for cavitation cone development $p_j > p_{cav}$. This is the case for both the MP and HP system. The corresponding cavitation number for is assumed to be $\sigma_d \approx 0.036$, based on an average value $p_{cav} \approx 28\ kPa$.

The reason for both systems to have a corresponding cavitation number is traced back to the change in parameters with respect to the smallest nozzle diameter from Table 6-2. For HP the SOD is 2.5 times larger while D_n is 6 times smaller. For MP on the other hand, the SOD is just 1.25 times larger and D_n is 3 times smaller. This returns a median value that should be close to the mentioned cavitation number.

This analysis is concluded by stating the correct normalised stagnation pressures p_{stag}/s_u in Table 6-4.

Table 6-4: values for the jet ratio p_{stag}/s_u at $s = SOD$

	$\boldsymbol{Jet\ pressure\ (bar)}$		
$\boldsymbol{s_u (kPa)}$	$\mathbf{3\ (p_{stag} = 3.0)}$	$\mathbf{30\ (p_{stag} = 5.3)}$	$\mathbf{130\ (p_{stag} = 12.0)}$
20	15.0	26.7	60.2
60	5.0	8.9	20.1
100	–	5.3	12.0
	$s < s_{dr}$	$s > s_{dr}$	$s > s_{dr}$

The value for $p_j = 3\ bar$ and $s_u = 100\ kPa$ in Table 6-1 and Table 6-4 is excluded. This is done because this test was not carried out during the experiments in the laboratory. The reason for this is the very low $p_{stag}/s_u = 3$ value indicative of jets that would be ineffective for soil excavation. This decision was justified by the very small jetting production values encountered in Chapter 5 for $s_u = 60\ kPa$ clay. This corresponds to the theory in (Nobel, 2013) that studies the excavation process of a horizontally moving vertical jet in a cohesive soil. Four different types of failure modes were distinguished based on the cavity dimensions and wall structure of the soil samples after conducting tests (see Chapter 2). The normalised jet pressure was found to be the decisive parameter to correlate the different cavity dimensions.

In the present study however, this is not possible because the SOD was varied. The corrected values in Table 6-4 were therefore used to correlate the different cavity dimensions. The minimum stagnation pressure needed for soil failure, is theoretically 6.2 times the undrained shear strength ($p_{stag,ss} \geq 6.2 \cdot s_u$). Not all normalised stagnation pressure values in Table 6-4 meet this requirement. The ones that do are highlighted in green (able to penetrate the soil surface) versus the ones in red (not able to penetrate the soil surface). This corresponds well with the observations in Chapter 5.

6.1.2 Jetting failure

The most important conclusion related to jetting are given in this subsection and are further discussed.

- Production decreases when soil strength s_u is increased (for a specific rotational speed n): stiffer clays have smaller p_{stag}/s_u values and it therefore is harder for the jet to penetrate the clay layer resulting in less production.
- Production increases when rotational speed increases: the main function of the jets is to loosen the soil; by increasing the n another feature of the jets becomes clearer, namely the tendency to accelerate particles of clay towards the suction inlet. This is directly proportional to the rotational speed.
- Contribution to the total production is more than half for low shear strengths and decreases rapidly for higher shear strengths: how stiffer the clay, how smaller p_{stag}/s_u becomes, meaning that the influence of the jets becomes smaller (cutting is not a function of p_j, see Subsection 6.1.3).
- Production increases exponentially with increasing jet pressure: Since the jet process for MP and HP is the same (i.e. I_0 is constant), the decisive process most likely be soil failure between trenches (see Section 6.1.4). Yet again for $s_u \gg 60\ kPa$ this increase is relatively small, meaning that no trenches were developed in very stiff clays (clays are only ''engraved'').

Jet cavity dimensions

Another difference between the present study and (Nobel, 2013) is the traverse velocity v_t; this parameter is replaced by rotational velocity of the tool v_r. The maximum value of the rational velocity is experienced at the outer edge of the pile and given here:

$$v_{r,max} = \omega \cdot R_p = \frac{\pi \cdot n}{30} \cdot \frac{D_p}{2} = 4.833 \cdot 10^{-3}\ \pi \cdot n \tag{6.1}$$

For $n = 1.0, 1.5, 2.0$ the corresponding maximum rotational velocity values are $v_{r,max} = 0.015, 0.023, 0.030\ m/s$.

The rotational velocities corresponding to each nozzle differ due to smaller radius. It is clear however that all velocities encountered in this study are relatively small and it always holds true that $v_r < 0.1\ m/s$. Based on this observation and the trenching theory as laid out before, an analytical model can be used to predict the cavity width W_c and cavity depth Z_c. In this model the entrainment of soil is neglected.

The cavity width is assumed to be equal to the jet diameter of the jet at the original soil surface ($W_c = D_{j,ss}$). This diameter follows from the equations for the free jet ($D_{j,ss} = 2 \cdot R_u$):

$$W_c = \sqrt{\frac{2}{k}} \cdot SOD + D_n, \qquad if\ SOD < s_{dr} \tag{6.2}$$

$$W_c = \sqrt{\frac{8}{k}} \cdot SOD, \qquad if\ SOD \geq s_{dr} \tag{6.3}$$

In which s_{dr} is the length of the flow development region $s_{dr} = \sqrt{k/2} \cdot Dn$ and R_u is the fictitious jet radius.

At the cavity bottom, the stagnation pressure of the jet p_{stag} is assumed to be equal to the bearing capacity of the soil q_{bc}. According to bearing capacity theory, the bearing capacity for cavities deeper than 1.6 times the jet load diameter is about $8.2 \cdot s_u$. It is assumed that for the penetrating jet the jet load diameter is equal to the cavity width ($D_l = W_c = D_{j,ss}$). This results in the following condition for the cavity depth:

$$p_{stag}(SOD + Z_c) = q_{bc} \approx 8.2 \cdot s_u \tag{6.4}$$

Substituting the stagnation pressure development into Eq. 6.4 results in the following equation for the cavity depth:

$$\frac{Z_c}{D_n} = a_1 \cdot \frac{p_{stag}}{s_u} + b_1 \tag{6.5}$$

The variables a_1 and b_1 are defined as follows:

For $Z_c + SOD < s_{dr}$:

$$a_1 = \sqrt{\frac{k}{2}} \cdot \frac{1}{N_{bc}(N_1 + 1)} \tag{6.6}$$

$$b_1 = -\sqrt{\frac{k}{2}} \cdot (N_1 + 1) \tag{6.7}$$

For $Z_c + SOD \geq s_{dr}$:

$$a_1 = \sqrt{\frac{k}{2}} \cdot \frac{1}{N_{bc} \cdot (2N_1 + 2)} \tag{6.8}$$

$$b_1 = -\sqrt{\frac{k}{2}} \cdot N_1 \tag{6.9}$$

In which $N_1 = SOD/s_{dr}$.

This model neglects the influence of cavitation (in the region of fully developed flow). For MP and HP however, the effects of cavitation are non-negligible; Eq. 6.3, Eq. 6.8 and Eq. 6.9 have to be rewritten in order to incorporate the effects of cavitation. This is done by substituting Eq. 2.31 in the mentioned equations. The cavity width is now determined by:

$$W_c = 4\alpha_{mom,cav} \cdot SOD,\ if\ SOD \geq s_{dr}\ and\ p_j > p_{cav} \tag{6.10}$$

The variables for cavity depth a_1 and a_2 now change to:

For $Z_c + SOD \geq s_{dr}\ and\ p_j > p_{cav}$:

$$a_1 = \frac{1}{2\alpha_{mom,cav}} \cdot \frac{1}{N_{bc}(2N_1 + 2)} \tag{6.11}$$

$$b_1 = -\frac{1}{2\alpha_{mom,cav}} \cdot N_1 \tag{6.12}$$

In Figure 6-1 the normalized calculated cavity depths, according to the analytical approach, are plotted as a function of the normalised stagnation ratio. A perfect linear trend with $R^2 = 1$ is found for the calculated values, as expected.

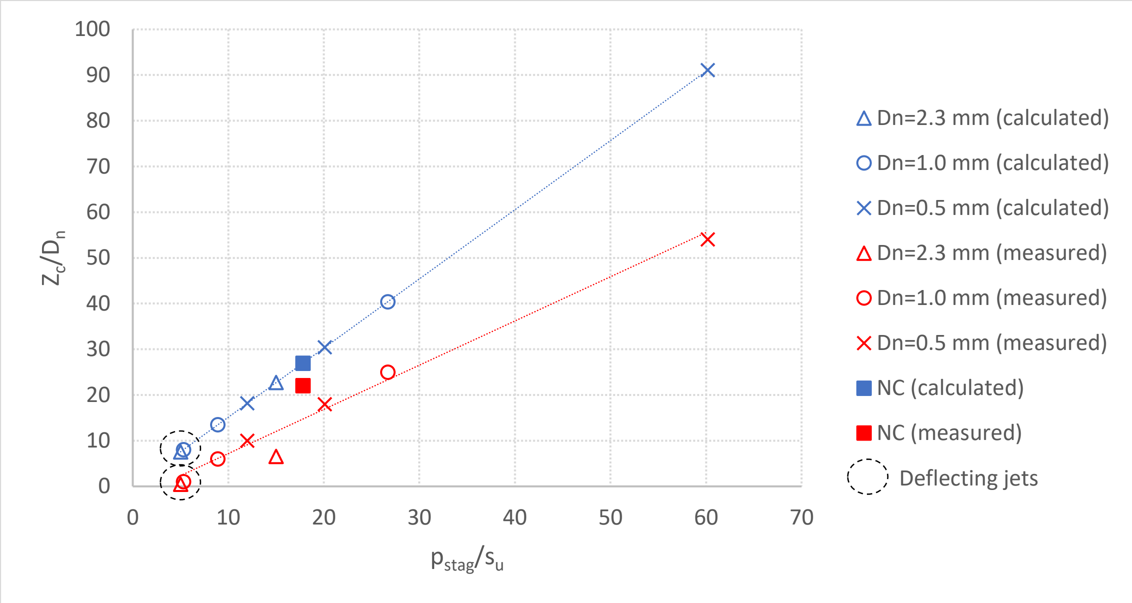

Figure 6-1: Calculated (analytical approach) and measured cavity depths Z_c normalized by the nozzle diameter D_n as a function of the normalised stagnation pressure p_{stag}/s_u.

Based on the graph in Figure 6-1 it is evident for the measured values that a direct proportionality between normalized nozzle diameter and stagnation pressure is present. The absolute values however deviate from the calculated ones. The measured values were obtained during the static tests (to exclude influence of cutting, rotating and plan failure). The method of measuring, using a tape measure, revealed to be challenging due to the location of the cavities inside the soil. The values for cavity depth Z_c were rounded and contain a margin of $\pm\ 5\ mm$. Nevertheless, the result is still underestimated, especially for the larger values of p_{stag}/s_u corresponding to the softest clay with a shear stress of $s_u = 20\ kPa$.

The two datapoints from Table 6-4 that were marked in red were also plotted in Figure 6-1. In theory these jets would not be able to penetrate the soil and would be considered deflecting or dispersing. The normalised stagnation pressure corresponding to these points however, deviates by only a small margin from the theoretical value of 6.2 (is in itself not a clear-cut boundary) that would imply soil penetration that leads to failure. Furthermore, it is mainly the cavity width W_c that deviates much form the theory rather than the cavity depth Z_c. Therefore both points were also incorporated into the analysis and are depicted in Figure 6-1 by the two most left datapoints (dashed circles). The difference between the measured values and theoretical values is substantial. The deflecting datapoints return a correlation of $6 - 12\%$ indicative of a very weak relationship while the other datapoints (i.e penetrating jets) hold a correlation which ranges between $45 - 62\%$ indicative of a moderate relationship.

The natural clay (NC) introduced in Section 4.3 was also added to this analysis. Represented by the solid square markers. It became clear that there is an improved correlation for natural clay, namely 82% which is indicative of a strong relationship between measured and calculated values. This implies that the natural clay, is more representative to clays on which the theory is based.

6.1.3 Cutting failure

As for jetting, this subsection starts with a brief introduction into the most important conclusion from the previous chapter.

- Production decreases linearly with increasing s_u: stiffer clay types indicate more frictional force must be exerted to achieve equal or more production. Since the set down pressure is kept constant throughout this condition is not met hence cutting is reduced.
- If the clay is softer (lower s_u), the jetting is tool is lowered more into the soil ensuring more material is peeled off from the top layer.
- Production increases when rotational speed increases: the frictional force developed by mechanical cutting is proportional to the velocity (for small velocities encountered here).
- Contribution to the total production is less than half for low shear strengths and increases rapidly for higher shear strengths: how stiffer the clay, how smaller jet ratio p_j/s_u becomes, meaning that the influence of the jets becomes smaller hence the influence of cutting becomes more dominant.

Specific cutting energy

In Section 2.3 two cutting mechanism were introduced (Miedema, 2019). The cutting mechanism encountered during the experiments resembles that of the Tear type. The specific cutting energy, which is the amount of energy, that has to be added to a volume unit of soil (e.g. clay) to excavate it is given by the following equation:

$$ESP_c = \lambda_s \cdot c \cdot \lambda_{HF} \tag{6.13}$$

In which λ_s is the strain rate factor average adhesion and cohesion (usually 2), c stands for cohesion and λ_{HF} is the horizontal cutting force coefficient. A couple of assumptions were made to determine the latter two:

- The cohesion c is assumed to equal the undrained shear strength s_u (based on Tresca theory).
- The horizontal cutting force coefficient is determined in (Miedema, 2019) through a figure as a function of the blade angle α and the ac ratio r (see Eq.2.44). Since there is no blade present in this study but rather a flat surface $\alpha = 0°$. The ac ratio gives the relation between the adhesion and cohesion. For very sticky clays (large adhesion) an ac-ratio of $r_{ac} = 2$ is mentioned. In the present study however the examined cement-bentonite mixture is less adhesive compared to natural clays with the same shear strength. A value of $r_{ac} = 0.10$ was deemed a reasonable estimate.

Concluding, for $\alpha = 0°$ and $r_{ac} = 0.10$ a value of $\lambda_{HF} \approx 0.7$ is read from the graph in (Miedema, 2019).

As given in Chapter 5, the jetting tool has a mass $m_T = 50\ kg$. This means that the tool can add a maximum of $50\ kg$ to the setup if fully submerged and rested on top of the bed, as was done for all experiments. A normal force of $F_v = m_T \cdot g = 490\ N$ is applied to the soil. Since the friction coefficient μ_F of either wood-on-clay and steel-on-clay is not known it is assumed that the resulting horizontal force $F_h = \mu_F \cdot F_v \approx F_v$. The specific cutting energy can now be determined according to:

$$ESP_c = \frac{F_h \cdot v_r}{prod_n} \tag{6.14}$$

In which $prod_n$ is the production obtained during one rotation for $n = 2\ rpm$.

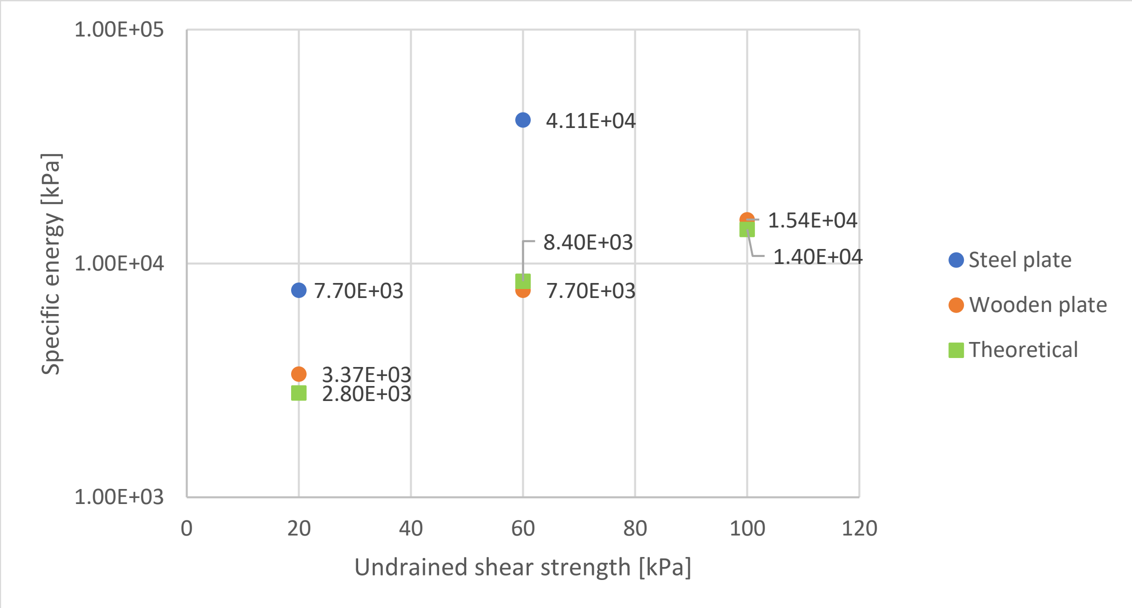

Figure 6-2: Calculated (cutting theory) and measured specific cutting energy ESP_c as a function of undrained shear strength for $n = 2\ rpm$.

The values for the steel plate are, compared to the wooden plate, higher for the same type of soil. There is more energy required to remove the same unit volume of clay, which implies less production as encountered in Chapter 5. The reason for this is that the wooden disk is not completely flat and therefore has a better cutting capability than the very flat steel plate. Another characteristic of the wooden plate is that one of the slots was cut open towards the end of the plate to enable nozzle $N5$ (outward facing nozzle) to reach the soil (it would hit the inner wall of the slot otherwise). This allows for an even larger ''scraping effect'' (see Figure 6-3 and Figure 6-4 for comparison of the two plates)

Figure 6-3: Top side of the Wooden nozzle plate

Figure 6-4: Bottom side of Steel nozzle plate

Looking at the values obtained from cutting theory gives quite good overlay with the measured values for the wooden plate. The same order of magnitude can be seen throughout. This is not the case for the steel plate. This may have to do with the assumed friction coefficient of $\mu_F = 1$. The theoretical values obtained with Eq. 6.13 can be implemented in Eq. 6.14 to determine if reliable friction coefficients μ_F could be returned. The expected values are given in Table 6-5.

Table 6-5: expected values for friction coefficient μ_F

s_u $[kPa]$	$Steel$	$Wood$
20	0.36	0.83
60	0.20	1.09
100	$-$	0.90
$\boldsymbol{\mu_{F,average}}$	$\mathbf{0.28}$	$\mathbf{0.94}$

The average values for the friction coefficient $\mu_{F,average}$ merely serve as a reference. Note, that this method only gives an indication of what sort of friction coefficients could be expected. They are certainly not precise, because that would imply that the theoretical approach would be exact. This of course is not the case, since this theoretical approach is built upon several assumptions.

6.1.4 Failure between jet trenches

This process occurs for the two softer clays in this study, $s_u = 20$ and $60\ kPa$. Comparing results for the same jet water distribution system of MP and HP a deep narrow trench ($p_j = 130\ bar$) or a wide shallow trench ($p_j = 30\ bar$) was obtained. Production in the form of jet momentum is assumed the same, but in which way the clay fails and/or the progress rate of the tool behaves is substantially different.

The failure that occurs between the trenches is also a function of the nozzle configuration (as seen in Figure 3.21). Due to the confined space in which all nozzles were mounted inside the jetting head and the required condition of operating a total of $n_j = 8$ nozzles a particular part of the clay surface between the inner and outer ring of nozzles was not fully covered. All vertical downward facing nozzles (i.e. represented as blue dots) are drawn into one quadrant (i.e. into one nozzle slot) in Figure 6-5.

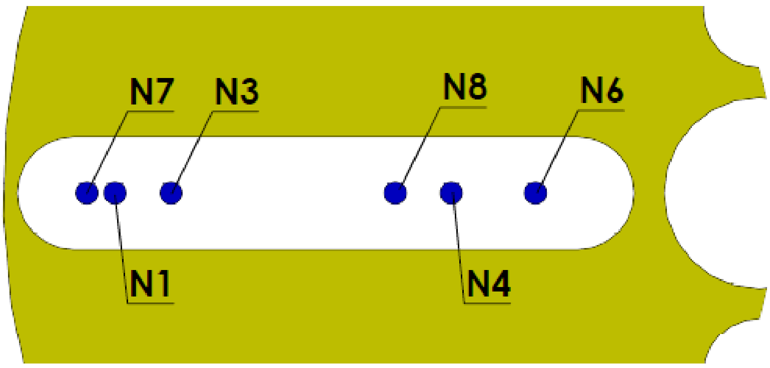

Figure 6-5: Nozzle configuration plotted in one quadrant.

It becomes clear from this figure that between nozzle $N3$ $(105\ mm)$ and $N8$ $(65\ mm)$ a gap of $40\ mm$ is present in which no nozzles are effectively working. Both nozzles mentioned here probably effected a small area of this gap close to the point of impact due to the diameter of the jet penetrating the soil, but were not capable of trenching this part of the surface area. This gap is clearly visible for the stiffest clay of $s_u = 100\ kPa$ (see Figure 5-15 for instance) due to the lack of large clay lumps and particles scattered over its surface and the lack of extreme slope failures which give an unclear image of the affected surface for more soft clay types.

6.1.5 Tool weight

The effect of set down pressure was presented in Section 5.5.2. It became clear that only utilizing 30% of the total gravitational force led to a production value that was ~ 7 times smaller than the one corresponding to maximum gravitational force of $F_{g,max} = 50 \cdot 9.81 \approx 500\ N$. A phenomenon that could describe why the difference in production is so large is given in Figure 5.4. This photo was taken during a regular experiment in which the total weight of the tool was put on top of the clay. The resulting $7.5\ cm$ deep pit originates only in this test because of one distinctive characteristic: the undrained shear strength.

A clay mixture with $s_u = 20\ kPa$ is prepared for this batch. This is categorised as a soft clay. Putting the full weight of the jetting tool on top of the clay bed and also introducing rotation will lead to shearing and the ability of the tool to break off big lumps of clay along unique fracture lines. The places where these fracture planes occur are difficult to predict, due to all the other processes that take place. A possible explanation could be that the fracture follows a path of least resistance; a path that occurs due to irregularities within the prepared cement-bentonite mixture.

This process mainly plays a role for soft clays. This does not mean however that the set down pressure will not affect stiffer clays. Nonetheless, for hard clays such as $s_u = 100\ kPa$, this process of large failure slopes was not observed at all.

In the undrained case shear planes/surfaces are formed in the soil. The shear stresses along these shear surfaces are equal to the undrained shear strength s_u. When a (jet) load exceeds the resistance in these shear surfaces, the soil will fail. For a vertical load on a flat horizontal soil surface the shear resistance is called the bearing capacity q_{bc} and can be calculated with the bearing capacity theory. The bearing capacity for a circular load at the soil surface:

$$q_{bc} = N_{bc} \cdot s_u \approx 6.2 \cdot s_u \tag{6.15}$$

In which N_{bc} is the bearing capacity factor. When the soil surface is not completely flat the bearing capacity factor will decrease. Theoretically N_{bc} can decrease to a value of 2. The weight of the tool is divided over a round surface and can therefore be seen as a circular load. The top layer of the clay resembles a horizontal clay bed, although some irregularities are present occasionally. For convenience the following bearing capacity factor is assumed in this study: $N_{bc} \approx 5 - 6$.

The surface area over which the tool acts does not cover the entire surface of the tool. It is certainly smaller because parts where jets penetrate the surface can be excluded. This depends of course on the type of nozzle and type of clay. It can be said with certainty that the $40\ mm$ gap between $N3$ and $N8$ is not influenced by jets and therefore has a larger height than surrounding clay, meaning that the tool will rest on this clay surface hence creating a sliding surface.

The surface area of the clay affected by the tool weight is determined as follows:

$$A_{tw} = \frac{\pi}{4} \cdot (D_{N3}^2 - D_{N8}^2) = 0.021 \tag{6.16}$$

The set down pressure p_{sd} of the tool has a constant value throughout the test program and is determined as follows:

$$p_{sd} = \frac{F_{g,max}}{A_{tw}} = 23\ kPa \tag{6.17}$$

Soil failure can only occur if $p_{sd} > q_{bc}$. This analysis returns that neither of the soils discussed in this study fail completely over the surface stated here due to set down pressure of the tool. It can be concluded that the set down pressure still contributes to soil production in the form of a variation in progress rate of the tool. In short, increasing p_{sd} will lead to the ability of loosening larger slices of clay.

Nevertheless, lumps of clay can still be removed under influence of set down pressure, due to the smaller surface area over which the tool acts in this case. For example, the lump removed from the $s_u = 20\ kPa$ clay in Figure 5.3. The triangular area is approximately $A_{lump} = \frac{1}{2} \cdot 10 \cdot 5\ cm = 25\ cm^2$. This returns a set down pressure of $p_{sd} = 200\ kPa$. The bearing capacity is approximated at $q_{bc} = 5.0 \cdot 20\ kPa = 100\ kPa$. In this case $p_{sd} > q_{bc}$ hence soil failure is initiated under influence of set down pressure.

6.2 Jetting model and specific energy

The power that is required to excavate a certain volume of soil is called the specific energy ESP. The methods of excavation in this study are characterised as mechanical i.e. cutting or hydraulic excavation i.e. jetting. In cohesive soils cutting is more efficient than jetting. Strictly speaking, in cohesive soils the specific energy for jetting is an order of magnitude higher than for cutting. The influence of cutting encountered in Chapter 5 plays an important role on the entire process that takes place inside the pile, of course to a greater or lesser extent depending on the parameters concerned.

A more fundamental approach regarding the progress rate of the tool attributed to jetting is implemented in this section. As was explained in Chapter 2 the jet momentum flux (see Eq. 2.20) is kept constant for the different jet regimes in order to compare different results to each other. Even though the product of u_0 and Q_o that make up I_0 is constant; the influence of the two separate parameters is not removed in this way. This problem is resolved by analysing the results in Chapter 5 as specific energy values. These E_{sp} results are independent of jet pressure p_j and discharge Q_0.

Water jetting is a function of pressure difference Δp and is not dependent on water depth. (Miedema, 2019) introduced a model in which the jetting process is worked out along the lines of the cutting process in a drag head. Not all parameters encountered in cutting are applicable for water jetting. Parameters used to determine ESP for drag heads like blade width and layer thickness are replaced by tool diameter D_T and cavity depth Z_c, respectively. Cutting velocity equals the rotational velocity v_r (see Eq. 6.1).

Permeability k and porosity (dilatation ε) can be neglected for cohesive soils (see Chapter 2); only the undrained shear strength s_u is of importance for the process. Blade height, blade angle and friction angles are not present for the water jetting process and will become part of a calibration constant C_1. On the other hand, jet pressure (difference) Δp and volume flow Q_0 are not part of the cutting process but will be part of the jetting model.

Resuming, a water jetting model for a drag head is developed, based on jet pressure and flow, drag head width and trailing speed and sand permeability, resulting in the penetration depth. The specific energy resulting from the model is calibrated on a cutting configuration and model tests.

The jet power depends on the product of the differential pressure (i.e. jet pressure) and the flow through the nozzle.

$$P_0 = p_j \cdot Q_0 \tag{6.18}$$

Substituting Eq. 2.23 and Eq. 2.24 into Eq. 6.18 gives the following:

$$P_0 = \Delta p \cdot c_d \cdot \frac{\pi D_n^2}{4} \cdot \sqrt{\frac{2\Delta p}{\rho_w}} \tag{6.19}$$

The efficiency of the pumps also needs to be taken into account. An efficiency of $\eta_{pump} \approx 0.9$ is assumed here for both pumps. The installed jet pump power for the jetting tool containing $n_j = 8$ nozzles is therefore determined according to:

$$P_j = \frac{\Delta p \cdot c_d \cdot \frac{\pi D_n^2}{4} \cdot \sqrt{\frac{2\Delta p}{\rho_w}} \cdot n_j}{\eta_{pump}} \tag{6.20}$$

The effect of the tool weight also had to be considered. The corresponding power required to establish jet trench failure under influence of the set down pressure p_{sd} is given as:

$$P_{tw} = F_h \cdot v_r \tag{6.21}$$

In which F_h is the resulting horizontal force and v_r is the rotational velocity of the tool assumed at $n = 2\ rpm$.

In this way the combined specific energy can be determined according to:

$$ESP_{com} = \frac{P_j + P_{tw}}{prod_{com}} \tag{6.22}$$

In which the values for combined production $prod_{com}$ are given throughout Section 5.3 and Appendix C.

The specific energy is set out against shear strength in Figure 6-6. The vertical axis is logarithmically scaled and has a range $1 \cdot 10^4 - 1 \cdot 10^7$ in which all aforementioned points fall. The specific energy has the same unit as pressure.

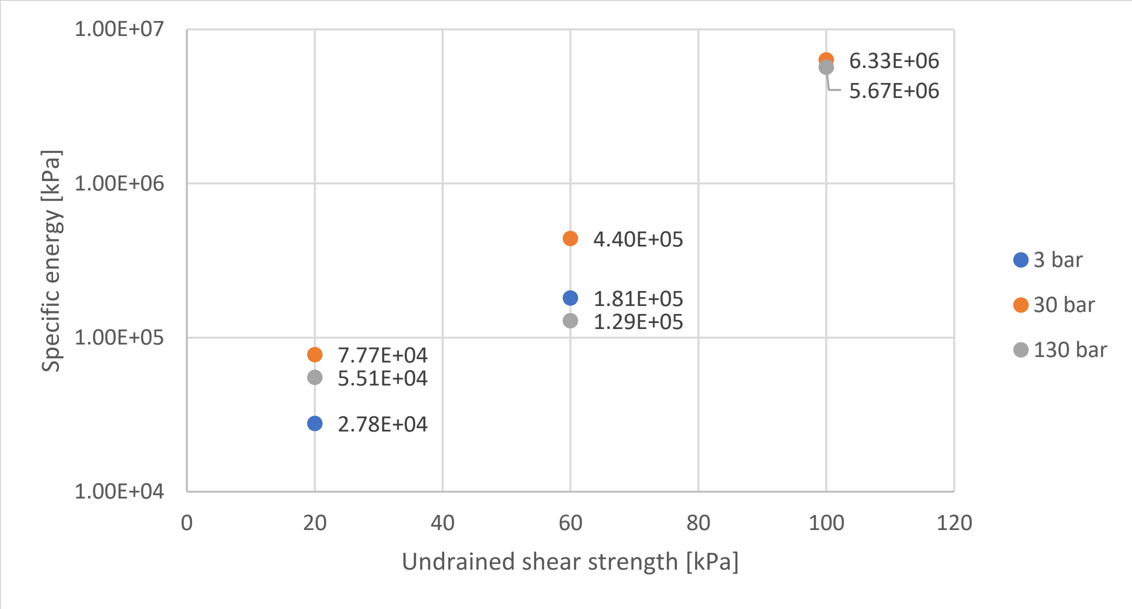

Figure 6-6: correlation between specific energy and undrained shear strength for combined production.

It follows from theory that a certain amount of energy is required to jet, but this is an order of magnitude lower than shown in Figure 6-6. Because in this case a lot of energy is also used in the soil failure between jet trenches (see Subsection 6.1.4). In short, the values given in this graph belong to the $combined\ production = jetting\ production + jet\ trench\ failure$. This explains why the values for ESP_{com} are so much higher than for jetting alone (i.e. the clay in between $N3$ and $N8$ is not touched by the jets).

It becomes clear from this graph that by increasing the shear strength by $40\ kPa$ the specific energy becomes an order of magnitude larger. Simply put, roughly 10 times more energy is needed for a 3 times stronger soil and 20 times more energy must be put into a soil that is 5 times stronger in order to excavate the same volume of clay.

The actual jetting production is in fact the soil excavated from the developed trenches. This parameter however is not known. This production can be calculated in accordance with the analytical model introduced in Subsection 6.1.2. In this way the cavity depth Z_c can be determined by simply multiplying the normalised cavity depths by the diameter of the specific nozzle in question. The related calculations are mentioned in Appendix C. The final result is shown in Figure 6-7.

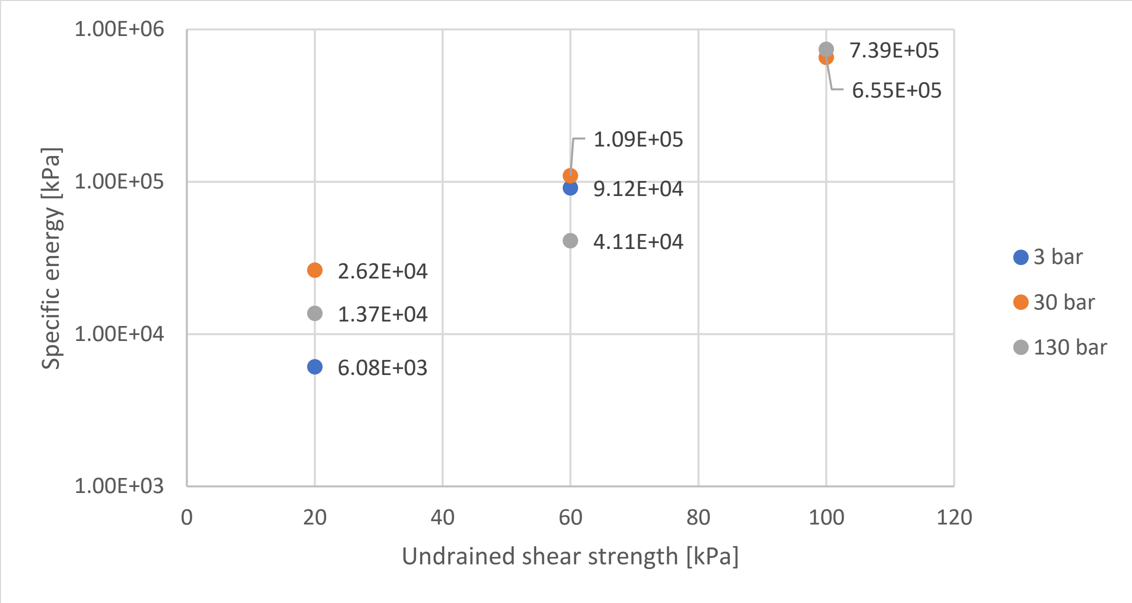

Figure 6-7: correlation between specific energy and undrained shear strength for (theoretical) jetting production.

This approach makes it feasible to determine how much energy is needed to attain a certain production and thus calculating the pump power. This power can now be varied beforehand by varying the share of jet pressure or jet discharge, while keeping the jet momentum flux constant.

A linear trend is clearly displayed in Figure 6-7 between specific jetting energy ESP_j and shear strength for a certain jet pressure.

The values for specific energy obtained by jet trench failure ESP_{tf} can now be determined in the following way:

$$ESP_{tf} = ESP_{com} - ESP_j \tag{6.23}$$

All specific energy values encountered in this chapter are now put together in Figure 6-8 to get an estimate of the total specific energy that was required during these experiments.

The labels underneath each bar must be read as follows:

- $LP, MP, HP = Low\ Pressure, Medium\ Pressure, High\ Pressure$
- $20, 60, 100 = undrained\ shear\ strength\ in\ kPa$

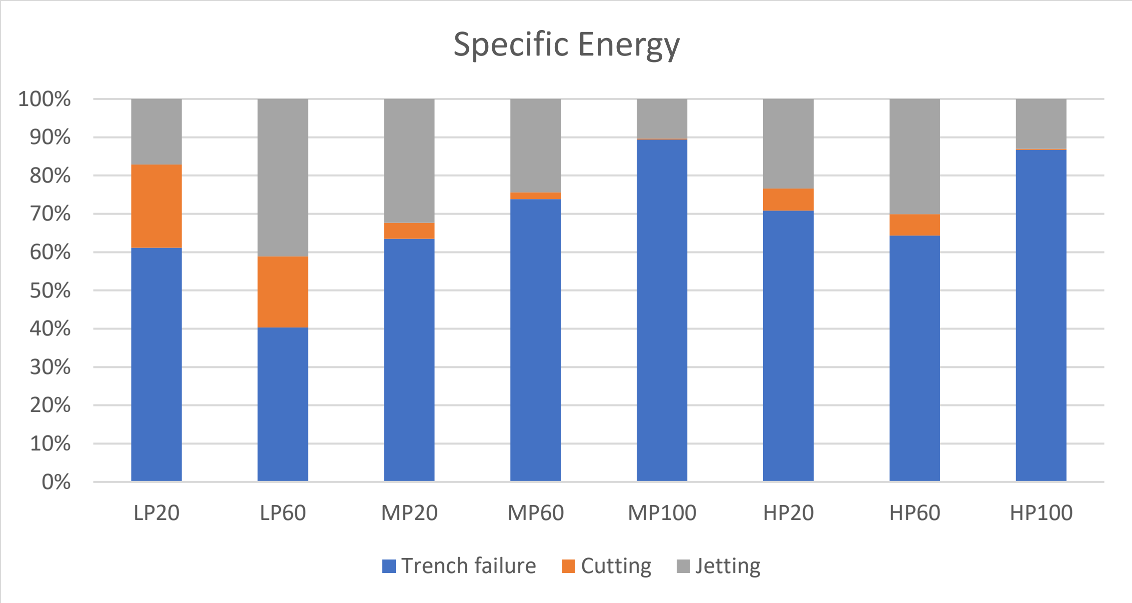

Figure 6-8: stacked bar chart representing the fractional contribution of jetting, cutting and trench failure to the specific energy

Since this figure represents the specific energy; higher ESP values mean there is more energy required to remove the same unit volume of clay, which implies less production.

An overall trend that can be observed is that the percentage of jetting and cutting is low compared to trench failure. Meaning that the contribution to the excavation production is larger for jetting and cutting. Also noticeable is that for the low-pressure system (steel plate) cutting plays a minor role compared to MP&HP (wooden plate), as was already seen in Subsection 6.1.3.

Another remarkable feature is that for the stiffest clay present in this study $s_u = 100\ kPa$ trench failure almost does not contribute to the production at all. This actually corresponds to the observations from Chapter 5. The clay is only ''engraved'' by the jets and small pieces of soil are peeled of under influence of cutting. So even though production in absolute values for jetting and cutting is low, trench failure almost does not occur at all. This is better seen in Figure 6-9, which displays the contribution of each failure type to the production.

As mentioned before, for both MP and HP systems the same wooden plate was used. This wooden plate came in contact with the soil surface since it was attached to the jetting head. Experimental results from Chapter 5 showed the same production for both systems. The fraction of cutting for one system stays almost equal. An explanation for this is that the fraction of jetting also stays the same and that is an obvious result from the previous chapter. When the shear strength increases, both cutting and jetting will decrease (i.e. it is harder to achieve soil failure under the same jetting and cutting conditions) retaining an equilibrium throughout.

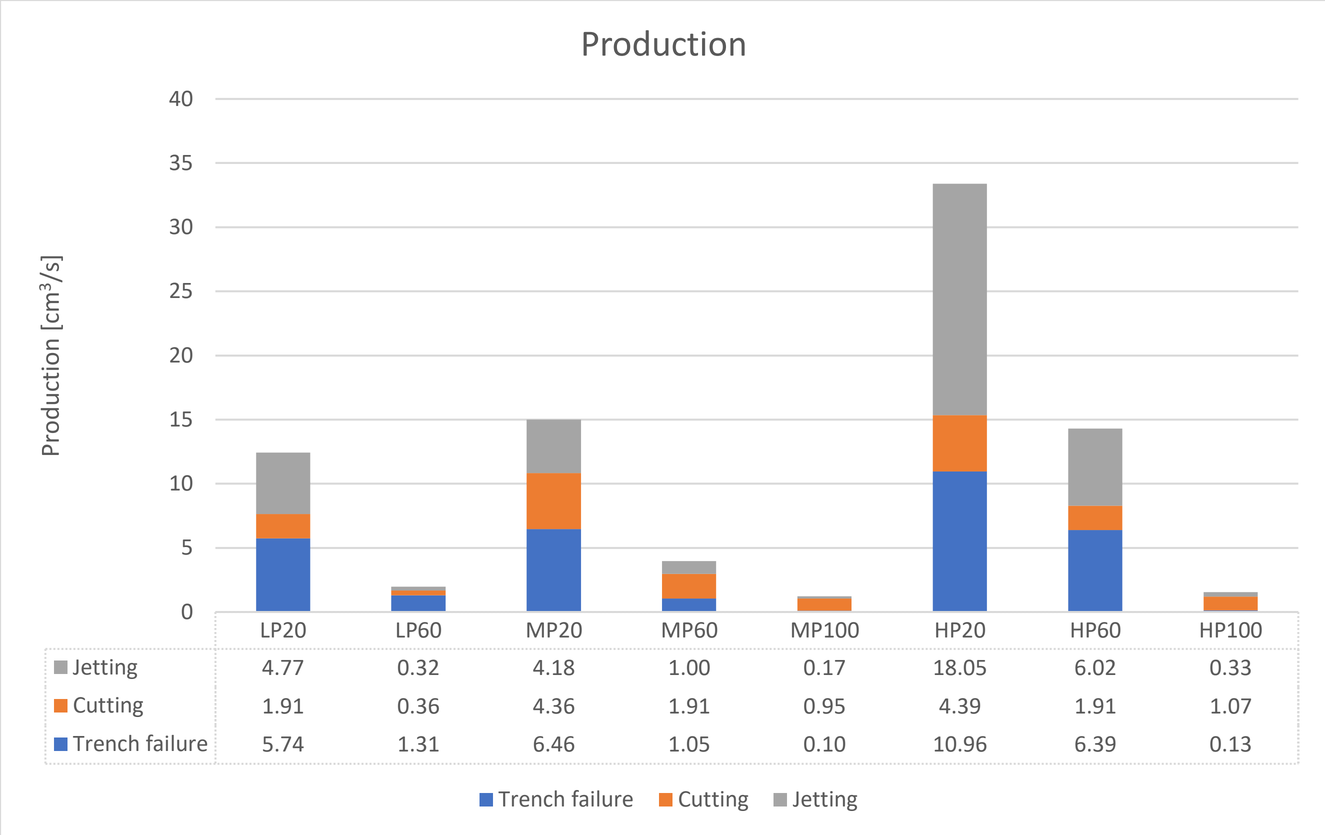

Figure 6-9: bar chart representing the contribution of jetting, cutting and trench failure to the total production.

The production values incorporated in the table in Figure 6-9, can now be translated back to values that can be expected in dredging practice. In doing so, several other model parameters need to be scaled as well. Recall from Section 3.3 that a scale of $1:5$ was applied to the scale model. This implies a scale factor (SF) of $\boldsymbol{n_L = 5}$ for the length scale. The other parameters scale according to the *Froude scale model* and are all listed in Subsection 2.5.3 as a function of the length scale n_L.

The translation from model values to prototype values can be seen in Table 6-6. The excavating production values (i.e. jetting and total production) are listed here together with parameters that serve as a starting point for their computation. The table is dived in three parts:

1. Model: provides the obtained values during the experiments
2. SF: shows the scale factor belonging to the parameter described in the same column
3. Protype: provides the values that can be expected in dredging practice

The model jet flow rate values in Table 6-6 correspond to the ones listed in Table 3-11 and the jet power values are calculated as the product of the jet pressure and this jet flow rate. The model production values can be obtained from the table in Figure 6-9 and are expressed here in m^3/h.

All prototype values in Table 6-6 are obtained by rewriting Eq. 2.63:

$$x_p = n_x \cdot x_m \tag{6.24}$$

In which x_p is the prototype value, n_x is scale factor and x_m is the equivalent model value.

Table 6-6: starting points for determination of jet and total production for $n_L = 5$

	Jet pressure $p_j\ (bar)$	**Shear strength** $s_u\ (kPa)$	**Jet flow rate** $Q_0\ (l/min)$	**Jet power** $P_0\ (kW)$	**Jetting production** $P_r\ (m^3/h)$	**Total production** $P_r\ (m^3/h)$
Model (x_m)	3	20 60	53.8	0.27	0.017 0.001	0.045 0.007
	30	20 60 100	15.2	0.76	0.015 0.004 0.001	0.054 0.014 0.004
	130	20 60 100	7.1	1.55	0.065 0.022 0.001	0.120 0.052 0.006
$SF\ (n_x)$	n_L	n_L	${n_L}^{5/2}$	${n_L}^{7/2}$	${n_L}^{5/2}$	${n_L}^{5/2}$
Prototype (x_p)	15	100 300	3007	75	0.96 0.06	2.50 0.40
	150	100 300 500	849	212	0.84 0.20 0.03	3.02 0.80 0.25
	650	100 300 500	399	432	3.63 1.21 0.07	6.72 2.88 0.31

By analysing the production values in Table 6-6 it becomes clear that that applying a larger jet power will lead to the removal of a larger volume of soil per unit of time. Even though this sounds as a logical consequence, it is not necessarily always true. (Nobel, 2013) for example showed the opposite. It should be noted however that he kept the jet momentum flux I_0 the same in all experiments (the flow is kept constant in this way). As was mentioned in Subsection 2.5.3; I_0 is kept constant in the present study as well to make a proper comparison between the three jet pressure regimes. Nevertheless, the obtained trend differs from the one obtained by (Nobel, 2013). The difference lies in the addition of excavation methods only encountered in the present study, like cutting and the influence of the tool weight.

The jet momentum flux values applied during the experiments can be seen in Table 6-7 and are calculated according to Eq. 2.20.

Table 6-7: Jet momentum flux for the three jet pressure regimes encountered during testing

Jet pressure $p_j\ (bar)$	**Jet flow rate** $Q_0\ (l/min)$	**Nozzle exit velocity** $u_0\ (m/s)$	**Jet momentum flux** $I_0\ (N)$
3	53.8	21.6	19.4
30	15.2	77.0	19.5
130	7.1	189.7	19.2

7 Conclusions and recommendations

It has been proved to predict the production for a Low Pressure (LP), Medium Pressure (MP) and High Pressure (HP) jetting system that is part of Soil Plug Removal Tool (SPRT). Based on specific energy ESP values that were either measured or theoretically calculated insight is given in the failure mechanisms present in pile dredging. This study focused mainly on hydraulic jetting, even though this is not the only process that takes place inside the pile while excavating. Mechanical excavation, jet trench failure (under influence of tool weight) and suction were also encountered.

The main research question was formulated as follows: **How much hydraulic excavation production can be achieved for a cohesive soil in small diameter piles, under different conditions, keeping the jet impulse flux equal?**

The expected production for tools in dredging practice is given in Table 7-1. Based on scaling theory, the values given here could be achieved with a tool that weighs roughly $m_T = 6250\ kg$.

Table 7-1: Expected maximum excavation production in dredging practice when rotating

Jet pressure $p_j\ (bar)$	**Clay type** $s_u\ (kPa)$	**Jet flow rate** $Q_0\ (l/min)$	**Jet power** $P_0\ (kW)$	**Jetting Production** $P_r\ (m^3/h)$	**Total Production** $P_r\ (m^3/h)$
$LP\ (15)$	$Stiff\ (100)$ $Very\ stiff\ (300)$	3007	75	0.96 0.06	2.50 0.40
$MP\ (150)$	$Stiff\ (100)$ $Very\ stiff\ (300)$ $Hard\ (500)$	849	212	0.84 0.20 0.03	3.02 0.80 0.25
$HP\ (650)$	$Stiff\ (100)$ $Very\ stiff\ (300)$ $Hard\ (500)$	399	432	3.63 1.21 0.07	6.72 2.88 0.31

7.1 Conclusions

Artificial clay

- Model soils can be prepared by mixing powdered bentonite and cement to produce an artificial clay. Undrained shear strengths of $s_u = 20\ , 60, 100$ can be obtained using cement-soil mass ratios CSR of $23.3\%, 56.7\%$ and 83.3% for curing times of approximately $19 - 24\ hr$.

Jetting head movement

- During static jetting hardly any soil is excavated (soil is only removed from the jet cavities with depths ranging from $Z_c = 0 - 3\ cm$). The tool remains in the starting position and does not progress downwards. This process is independent of shear strength s_u and jet pressure p_j.

- Stepwise rotation production decreases linearly when shear strength is increased up to a point where the trend flattens to zero. This regime change starts at $s_u > 70\ kPa$ for LP and increases further for larger jet pressures. The absolute values are only a fraction of the production obtained by continuous rotation. This fraction ranges from $10 - 20\%$ for the lowest rotational speed of $n = 1\ rpm$. For increased rotational speeds this fraction decreases further. Making rotational production far superior to stepwise production under the same conditions mentioned in this study.

- A random moving single water jet nozzle returns a production that is roughly 12 times higher than for the jetting tool (containing 8 nozzles) rotating at maximal speed of $n = 2\ rpm$. It should be noted however that this specific test (loosening clay soil with a spray lance rather than with a jetting tool) did not involve any set down pressure, suction or nozzle configuration. Additionally, rather than removing the resulting slurry the column of clay was deemed fully removed when all the clay was in suspension. Despite these differences in working method, it can be concluded that this random moving nozzle is more efficient than multiple fixed nozzles placed inside a jetting head under the condition of an identical jet momentum flux I_0.

Excavation method and failure mechanisms

- Cutting production is directly proportional to the (rotational) velocity, which is in accordance with the theory of (Miedema, 2019) that states that the cutting energy per unit of time is directly proportional to the velocity. Thus, the frictional power required for mechanical cutting is proportional to the velocity. This linear relation only holds true if the frictional force is constant, which is the case here since the set down pressure of tool is not varied.

- Another failure mechanism is present besides jetting and cutting. Trench failure between jet walls is initiated under influence of the weight of the jetting tool and sliding surfaces with respect to removed soil by other failure mechanisms.

- Deep narrow trenches were attained for HP and wide shallow trenches for MP. This corresponds well with larger production attained by trench failure for HP. Provided that enough material is excavated by the jets, notably exhibited by soft clays $s_u = 20$ and $60\ kPa$.

- The softest clay encountered $s_u = 20\ kPa$ fails under influence of the weight of the tool. The set down pressure of the tool exceeds the bearing capacity $p_{sd} > q_{bc}$ for affected surface areas (facilitated by existing jet trenches).

- Very stiff clays $s_u = 100\ kPa$ are only ''engraved'' by rotating jets; actual trenches are not present hence jet trench failure is not encountered. Most of the production is related to cutting (in absolute sense of course lower than for the softer clays). Roughly $80 - 90\%$ is production by cutting. The jets are most likely contributing to the total production by efficiently transporting the mechanically excavated material towards the suction pipe, increasing progress rate of the tool in the meantime. This last process also holds true then for the other shear strengths, although not directly noticeable as for very stiff clays.

Production

- Total production is inversely proportional to shear strength and direct proportional to jet pressure. Jet momentum flux I_0 is kept constant throughout the experiments implying a constant value for production when varying jet pressure p_j. (Nobel, 2013) encountered the exact opposite process: lower pressure implies larger nozzles hence shallow but wider trenches; making it easier to initiate jet trench failure. In short, larger production for low pressure jets is expected. As the pressure increases the production should decrease, because of narrower/deeper trenches making it more difficult for the soil to fail in between trenches. The difference between (Nobel, 2013) lies in the addition of excavation methods only encountered in the present study. One remarkable point is the increase in cutting production between LP (steel plate) and the MP&HP system (nozzle plate). This contributes to an increase in total production while increasing p_j.

- The jetting production can be estimated by an analytical model when $v_r < 0.1\ m/s$.

- Production is increased towards the pile wall (also cleaning effect) and towards the centre of the pile by oblique impinging jets under an angle of $45°$. The increased production stems from the fact that a larger area can be excavated by inclined jets (surface affected is increased rather than a single trench for downfacing nozzles).

- Slurry removal (using a suction tube) is a process that also influences progress rate of the tool. With steady removal rates between $50 - 80\ l/min$, no pipe blockages were encountered during testing (this is confirmed by logging data and visual observations)

- The inlet of the suction pipe should be mounted at least $10\ mm$ above the bottom plate of the jetting head to prevent blockage of the opening.

7.2 Recommendations

This study represents a first step in defining the hydraulic excavation mechanism in cohesive soils for a Soil Plug Removal Tool (SPRT) based on scale tests combined with fundamental theories in hydrodynamics and soil mechanics. The scope of the present research has been confined in order to focus on the fundamental issues and achieve the goals within a reasonable time frame.

The following recommendations are offered for further study:

Artificial clay

- The strength and deformation properties of the artificial clay are important with respect to the behaviour of the SPRT. Research should be carried out to study the effect of different jetting parameters on the engineering properties of the artificial clay. Samples can be taken from the cement-bentonite mixture and subjected to laboratory tests to obtain the stress-deformation, strength characteristics and properties like adhesion. There was a noticeable difference between the artificial clay and natural modelling clay tested in this study. They were solely compared based on shear strength. This discrepancy in measured values is not well understood. In particular, an investigation on the effect of the brittle nature of a clay to which cement is added would be of interest.

Jetting tool and test setup

- The transport production was eventually not measured in this study. The derived conclusions are only based on excavation production. Nevertheless, the excavation production already gives insight into what production can be expected for which parameter set. To further improve on this, it will be crucial to measure the vacuum at the inlet of the suction pipe. Acquiring this vacuum will lead to a better understanding of the discharge values measured by the discharge meter hence obtaining a more thorough and better understanding of the realized production while at the same time acquiring the transport production.

- Improve the jetting tool by fixating the SOD to a single value. Nozzles should be in line with the slots of the nozzle plate. In this way, adding a new disk (i.e. wooden disk) will become obsolete making production better relatable to variations in specific parameters.

- In order to obtain a better value for the friction coefficient for tool-soil interaction it is proposed to add a device to measure the torque applied to the jetting tool (i.e. power consumption). In this way more the specific energy can be calculated.

- Improve the distribution of the nozzles inside the jetting head to further increase the jet impingement on the clay surface.

Research

- Due to time restrictions, it was eventually not possible to measure the influence of different nozzle angles. As mentioned before, only two nozzles were placed under an angle. This opens the way for further investigation into applying different nozzle angles (i.e. it is possible to attain nozzle angles of $30°$ with the current jetting tool next to the aforementioned $45°$ angle).

Bibliography

Albertson, M. (1950). Diffusion of Submerged Jets. *Transactions of the American Society of Civil Engineers, 115(1)*, 639-664.

Ambrose, S. (2015). *The rise of Taylor bubbles in vertical pipes.* Thesis.

Beltaos, S. (1976). Oblique impingement of circular water jets on a plane boundary. *Journal of Hydraulic Research, 14(1)*, 17-36.

Casagrande, A. (1948). Classification and Identification of Soils. *Transactions of the American Society of Civil Engineers*, 901-930.

Cengel, Y. (2006). FLUID MECHANICS FUNDAMENTALS AND APPLICATIONS. In *Nondimensionalized Equations of Motion* (pp. 473-476). New York: McGraw-Hil.

Dayal, U., & Allen, J. (1975). The Effect of Penetration Rate on the Strength of Remolded Clay and Sand Samples. *Canadian Geotechnical Journal Vol. 12 (3)*, 336-348.

Fischer, H. (1979). *Mixing in Inland and Coastal Waters.* Academic Press, INC.

Giles, R. (1962). *Schaum's Outline of Theory and Problems of Fluid Mechanics and Hydraulics.* New York: McGrawHill Book Company.

Govier, W., & Aziz, K. (1972). *The Flow of Complex Mixtures in Pipes.* New York: van nostrand.

Hatamura, Y., & Chijiiwa, K. (1977). Analyses of the mechanism of soil cutting, 5th report. *Bulletin of the JSME, 20(141)*, 388-395.

Ho, C. (2005). *Turbulent Fluid Jet Excavation in Cohesive Soil with.* Cambridge, Massachusetts: Massachusetts Institute of Technology, Ph.D. Thesis.

Jalil, A., & Rajaratnam, N. (2006). Oblique impingement of circular water jets on a plane boundary. *Journal of Hydraulic Research, 44(6)*, 807-814.

Kulhawy, F., & Mayne, P. (1990). *Manual on estimating soil properties for foundation design.* Stockholm: Electric Power Research Institute.

Miedema, S. (1992). New developments of cutting theories with respect to dredging, the cutting of clay. *WODCON XIII.* Bombay, India: World Dredging Association (WODA).

Miedema, S. (2019). Dredging Engineering Special Topics. In *The Pump/Pipeline System* (pp. 199-228). Delft: Delft University of Technology.

Miedema, S. (2019). *The Delft Sand, Clay & Rock Cutting Model, 3rd Edition.* Amsterdam: IOS Press.

Mitchell, J. K., & Soga, K. (2005). 4. Soil Composition and Engineering Properties. In *Fundamentals of Soil Behavior (3rd Edition)* (pp. 83-108). Hoboken, New Jersey: John Wiley & Sons.

Nicklin, D. (1963). The Air-Lift Pump: Theory and Optimization. *Transactions of the Institution of Chemical Engineers, Vol 41*, 29-39.

Nobel, A. (2013). *On the excavation process of a moving vertical jet in cohesive soil.* Delft: Delft University of Technology.

numeric-GmbH. (2015, March 3). *numeric-GmbH* . Retrieved from https://www.numeric-gmbh.ch/posts/discharge-coefficients-in-aircraft-decompression-simulations.html

Rajaratnam, N. (1976). *Turbulent Jets. Developments in water science.* Amsterdam: Elsevier.

Rao, G. (2009). *Heat transfer characteristics of a multiple jet impingement system.*

Reinemann, D., & Timmons, M. (1987). *An Interactive Program for the Design of Airlift Pumping and Aeration Systems.* Ithaca, NY: Department of Agricultural Engineering, Internal Report, Cornell University.

Skempton, A. (1948). The φ=0 Analysis of Stability and Its Theoretical Basis. *2nd International Conference on Soil Mechanics and Foundation Engineering*, (pp. 72-78). Rotterdam.

Soga, K., & Mitchell, J. (1996). Rate-dependent Deformation of Structured Natural Clays. *Measuring and Modeling Time Dependent Soil Behavior* (pp. 243-257). New York: ASCE.

Terzaghi, K. (1925). "Principles of Soil Mechanics: I—Phenomena of Cohesion of Clays,". *Engineering News-Record, Vol. 95, No. 19*, 742-746.

Terzaghi, K. (1936). "Relation Between Soil Mechanics and Foundation Engineering: Presidential Address". *Proceedings, First International Conference on Soil Mechanics and Foundation Engineering*, (pp. 13-18). Boston.

Terzaghi, K. (1943). *Theoretical Soil Mechanics.* New York: John Wiley & Sons, Inc.

Trevisanut, S. (2020). Decommissioning of Offshore Installations: a Fragmented and Ineffective International Regulatory Framework. In *The Law of the Seabed* (pp. 431-453). Leiden: Brill Nijhoff.

van der Schrieck, G., & van Rhee, C. (2010). Physical scale modeling of dredging processes in sand and gravel. *WODCON XIX: "Dredging makes the World a better place" -.* Beijing, China.

Verruijt, A. (2004). *Soil Mechanics.* Delft.

Wahls, H. (1983). Undrained Shear Strength of Saturated Clay. (pp. 5-9). Transportation Research Board.

White, F. (2011). Dimensional Analysis and Similarity. In *Fluid Mechanics, seventh edition* (pp. 293-346). New York: McGraw-Hill.

Winterwerp, J., & van Kesteren, W. (2004). Developments in. In *Introduction to the Physics of Cohesive Sediment Dynamics in the Marine Environment.* Amsterdam: Elsevier.

Yong et al., R. (2012). *Environmental Soil Properties and Behaviour.* Boca Raton: CRC Press.

Zhang et al., S. (2016). Experimental Research on Trenching in Stiff Clay by Submerged Vertical Traveling Jets. *Journal of Coastal Research, 32(2)*, 365-373.

Appendix A

Laboratory Test Setup

A.1 Medium and High Pressure system

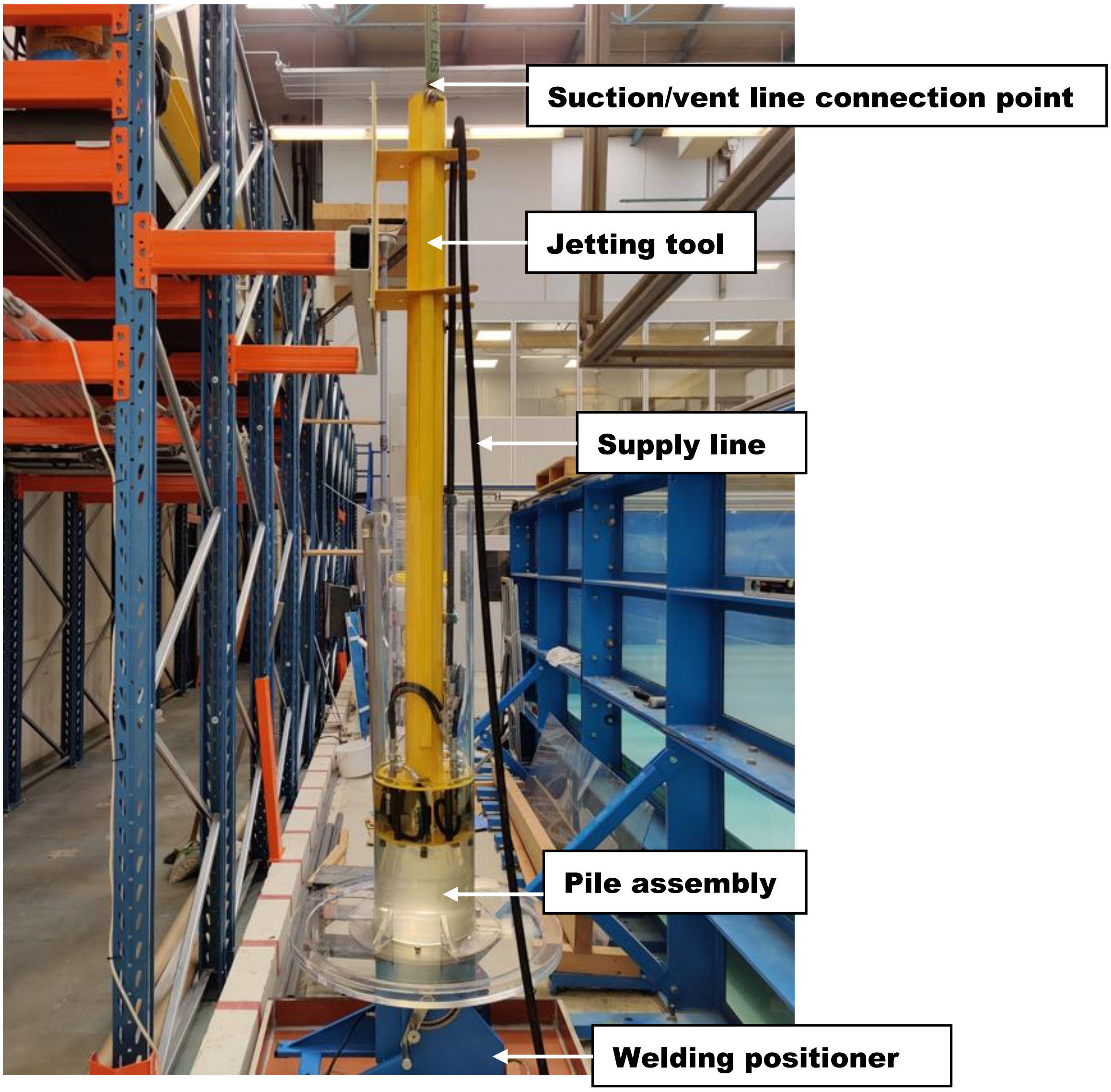

Figure 0-1:Jetting tool placed inside the pile

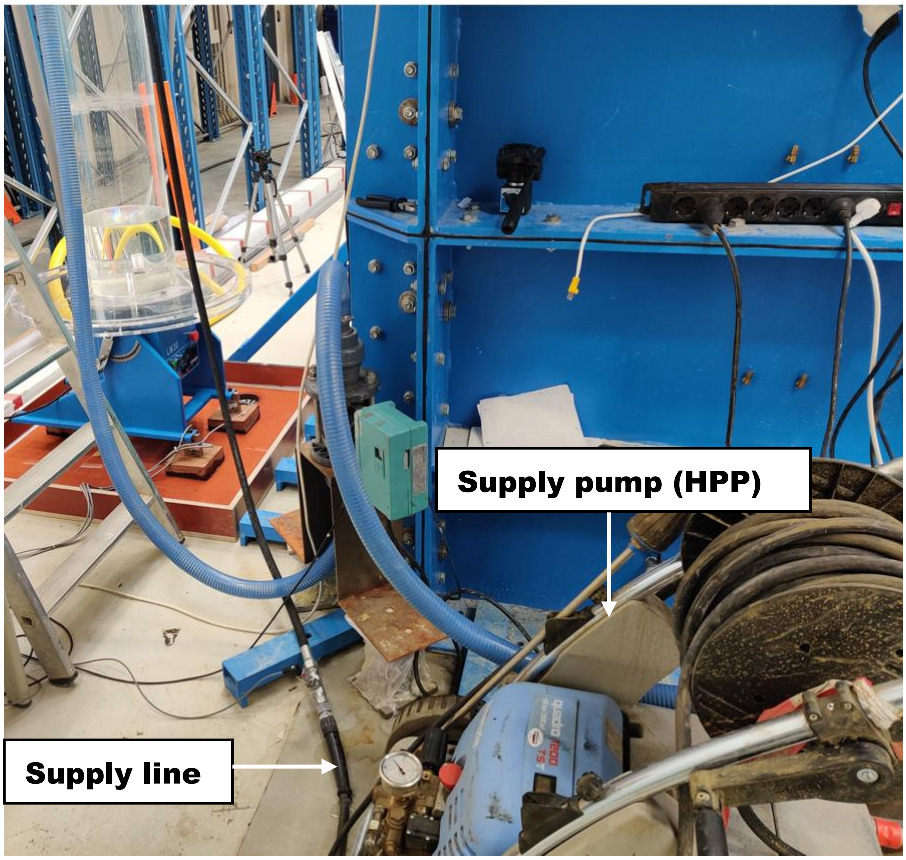

Figure 0-2: High Pressure Pump (HPP) that serves as supply pump for the jet water. Supply line is connected to the jet water distribution system mounted on the jetting tool.

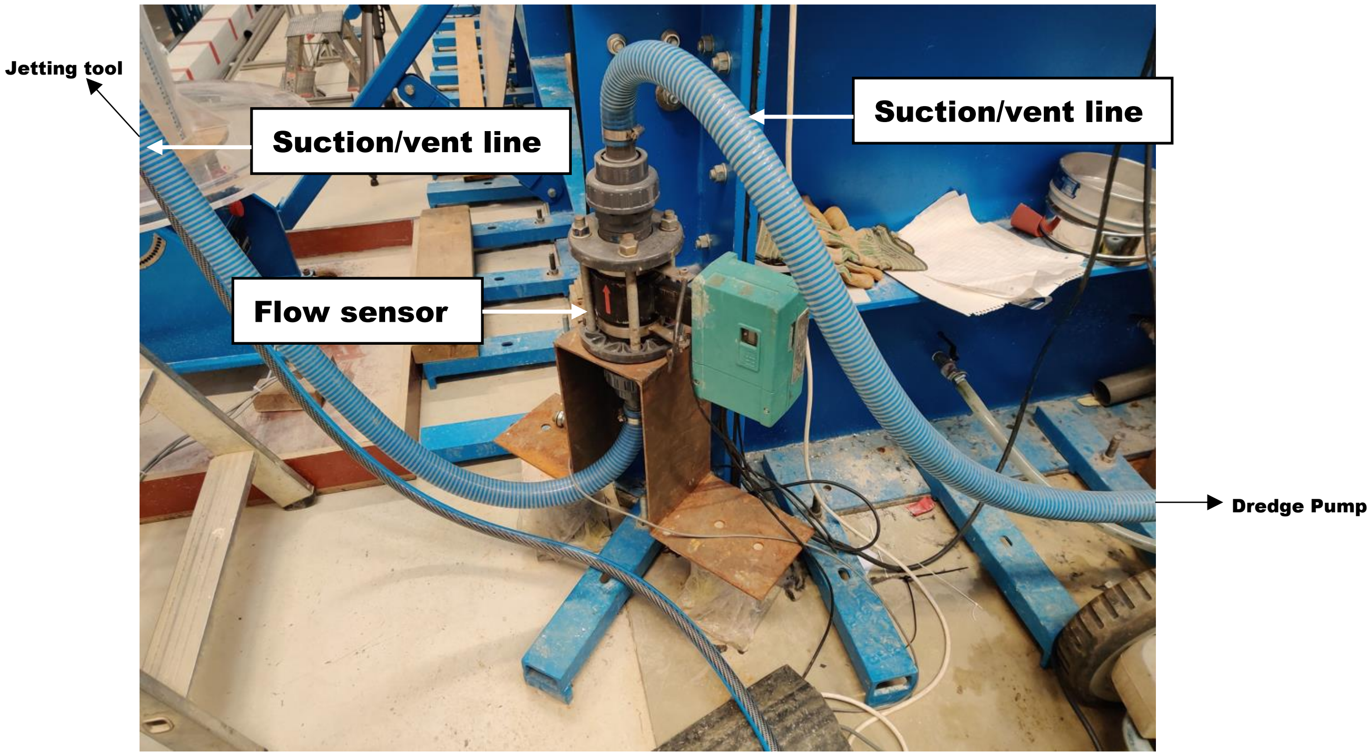

Figure 0-3: Flow sensor that connects the suction/vent line from the jetting tool on one side (to the left) and the dredge pump on the other side (to the right).

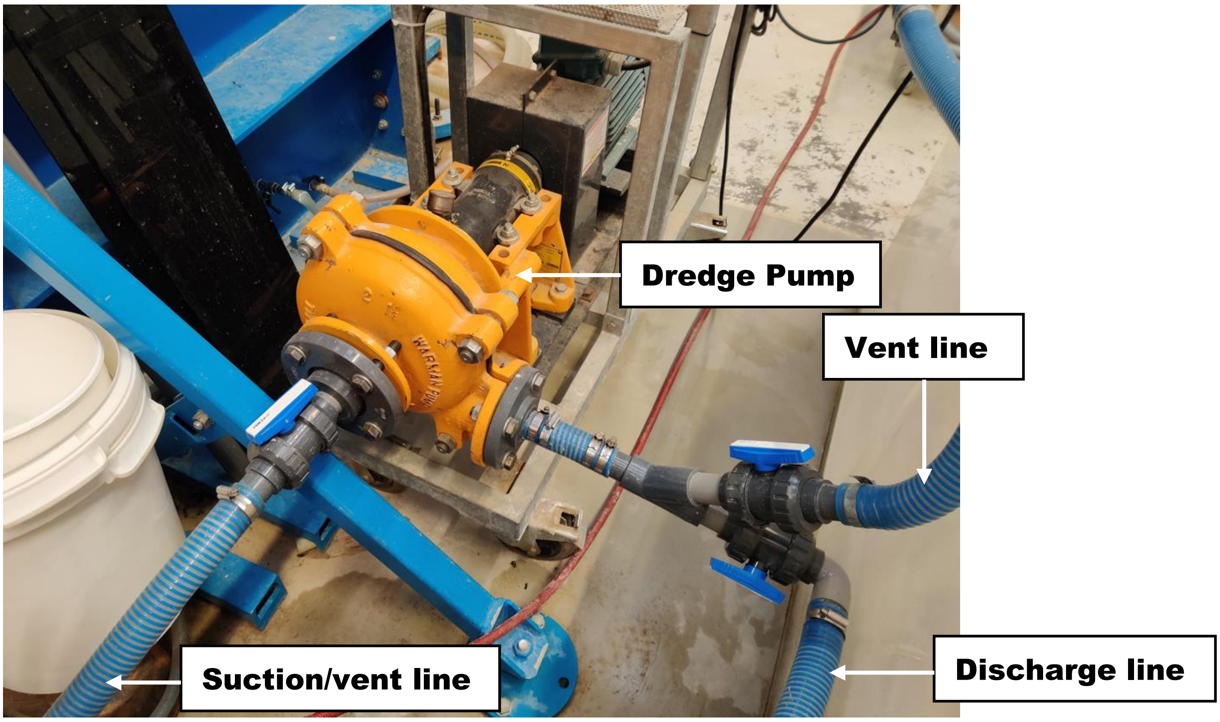

Figure 0-4: The suction/vent line is connected to the suction side of the centrifugal pump (inlet), while the discharge line is connected to the discharge side (outlet). The vent line is only used to vent the system at the beginning of each experiment (valve is opened).

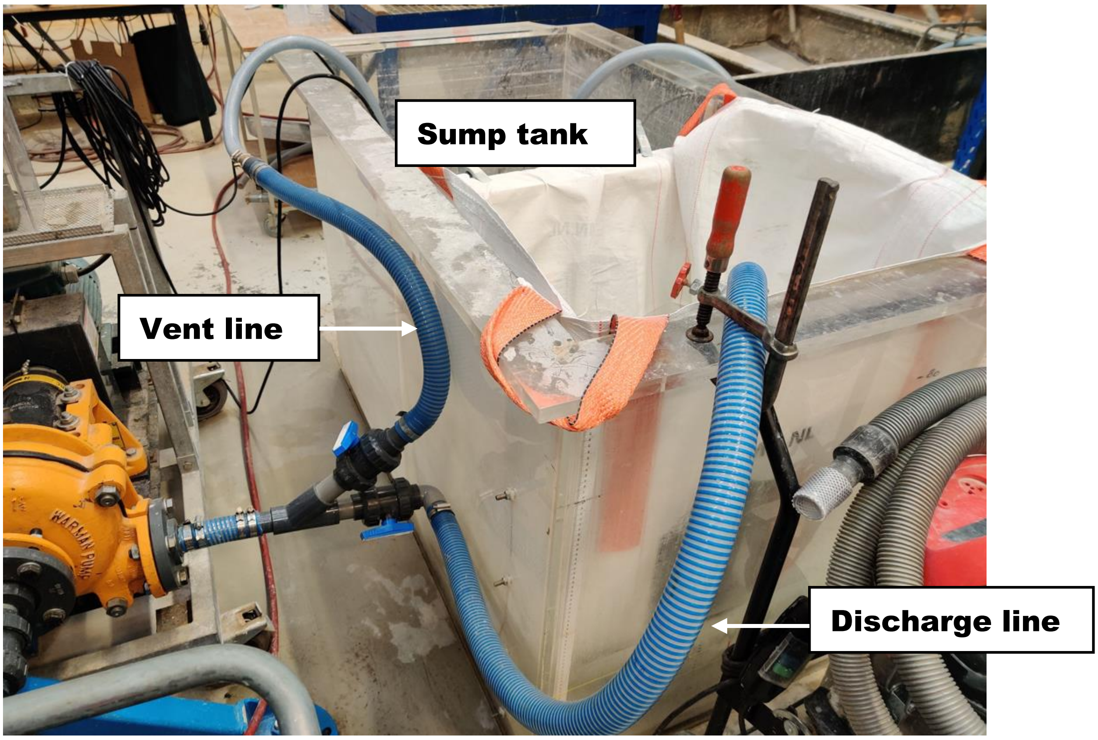

Figure 0-5: Sump tank in which the obtained slurry is discharged in a big bag.

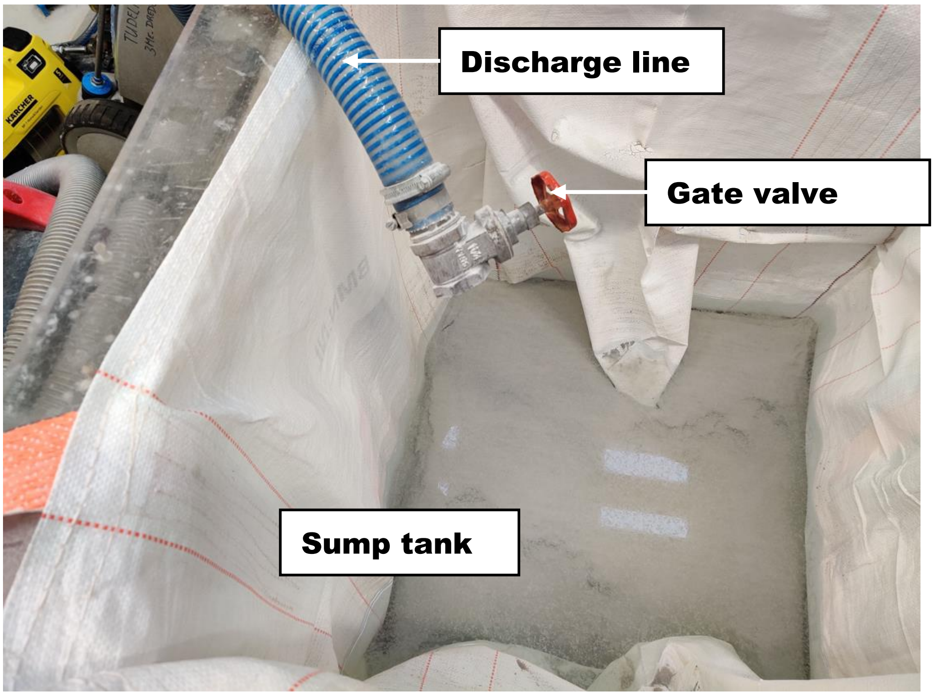

Figure 0-6: Inside view of the sump tank. The slurry through the discharge line can be altered by using the gate valve in place.

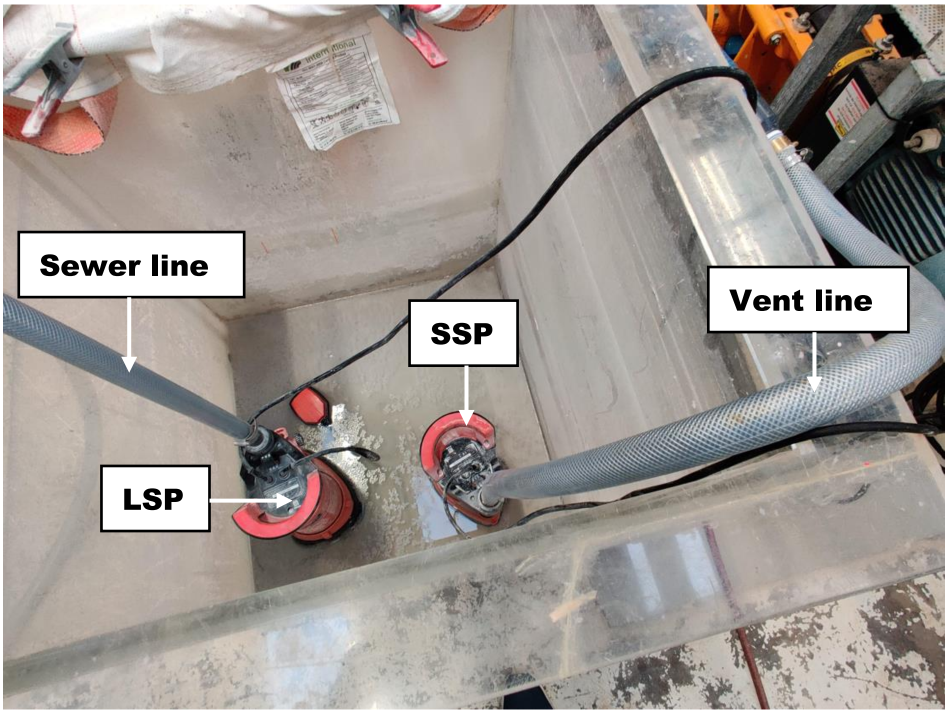

Figure 0-7: Inside view of the other compartment of the sump tank (serves as an overflow). The vent line is operated through the Small Submersible Pump (SSP). The Large Submersible Pump (LSP) removes the excess water accumulated in this overflow compartment through the sewer line towards the water reservoir.

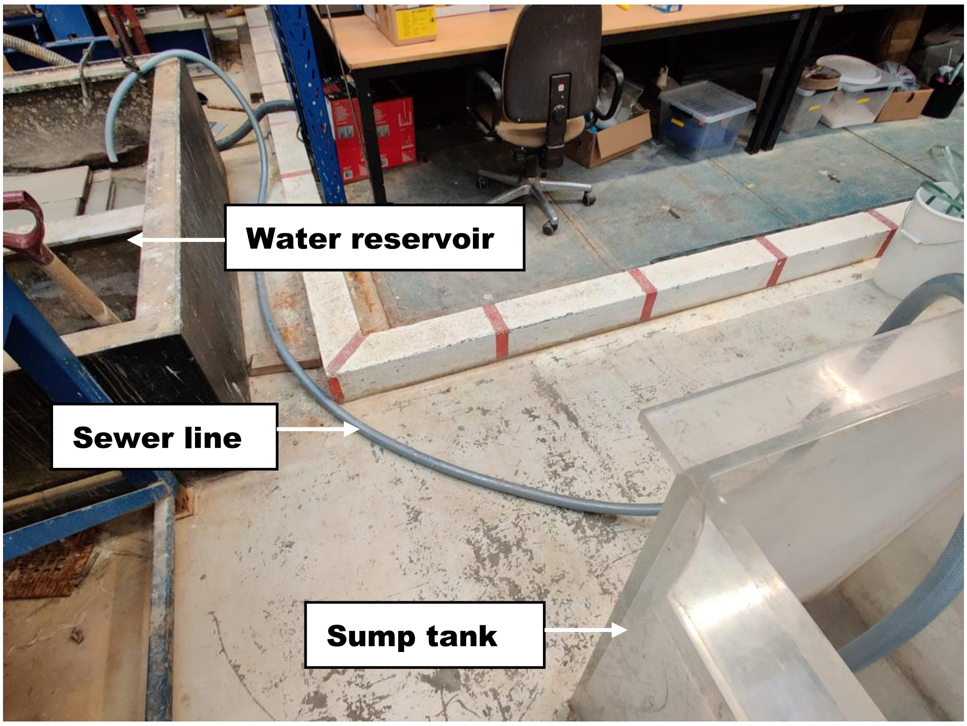

Figure 0-8: Excess water is transported through the sewer line towards the water reservoir which is connected to the sewer.

A.2 Low Pressure system

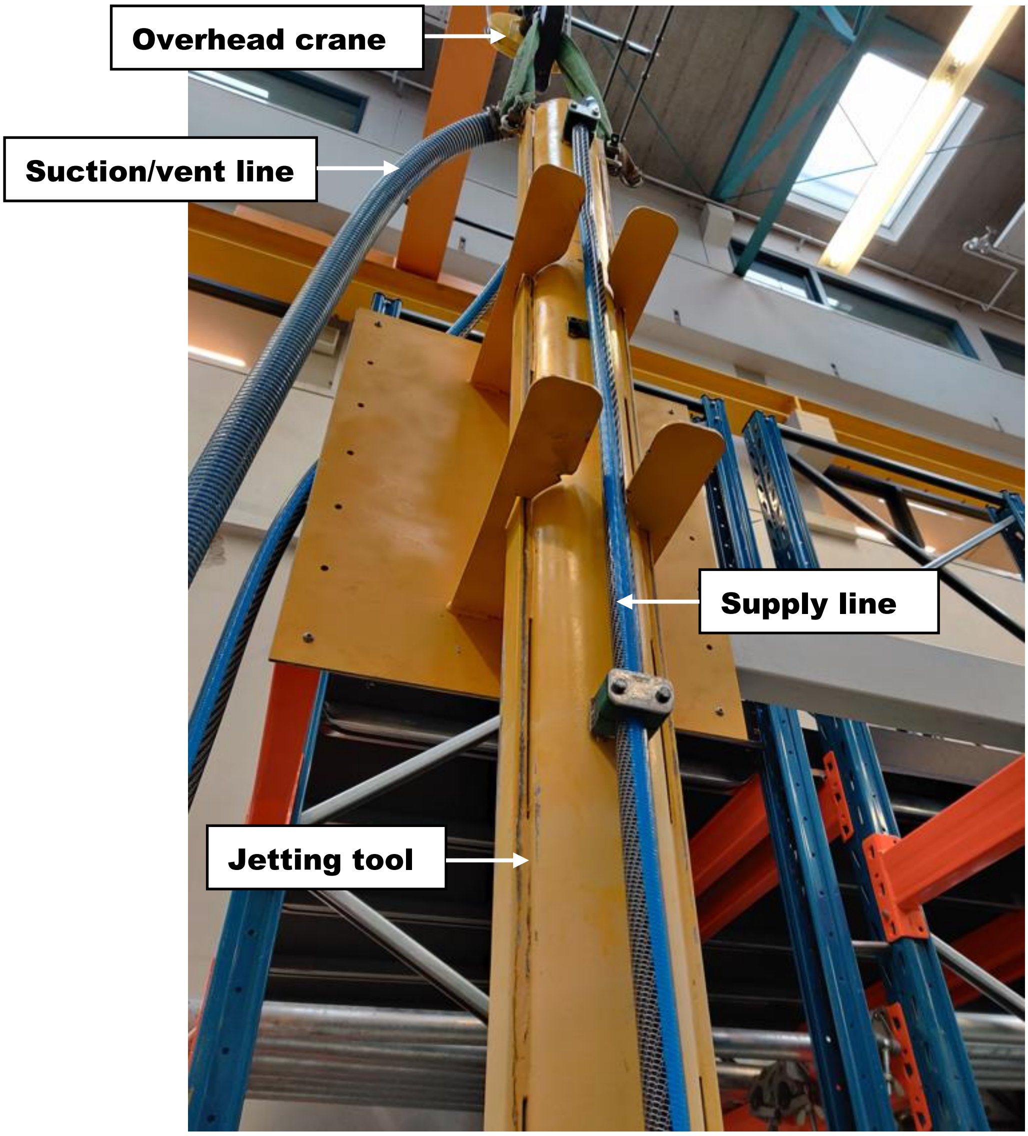

Figure 0-9: jetting tool belonging to the LP system and containing another jet water distribution system

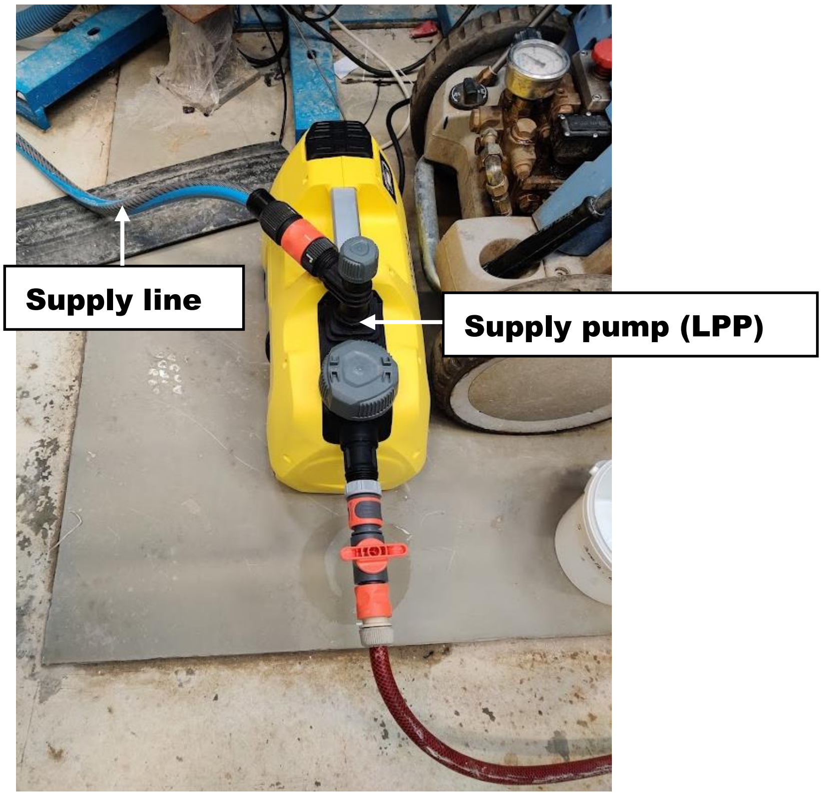

Figure 0-10: Low Pressure Pump (LPP) that serves as supply pump for the jet water. Supply line is connected to the jet water distribution system mounted on the jetting tool

A.3 Other components

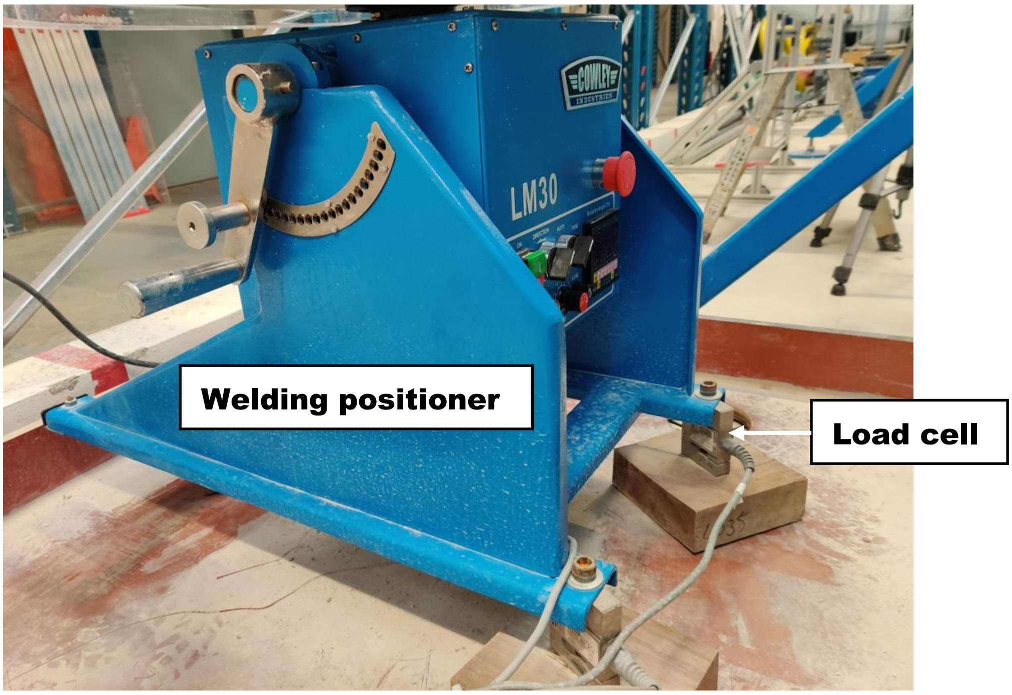

Figure 0-11: welding positioner standing on top of three loadcells

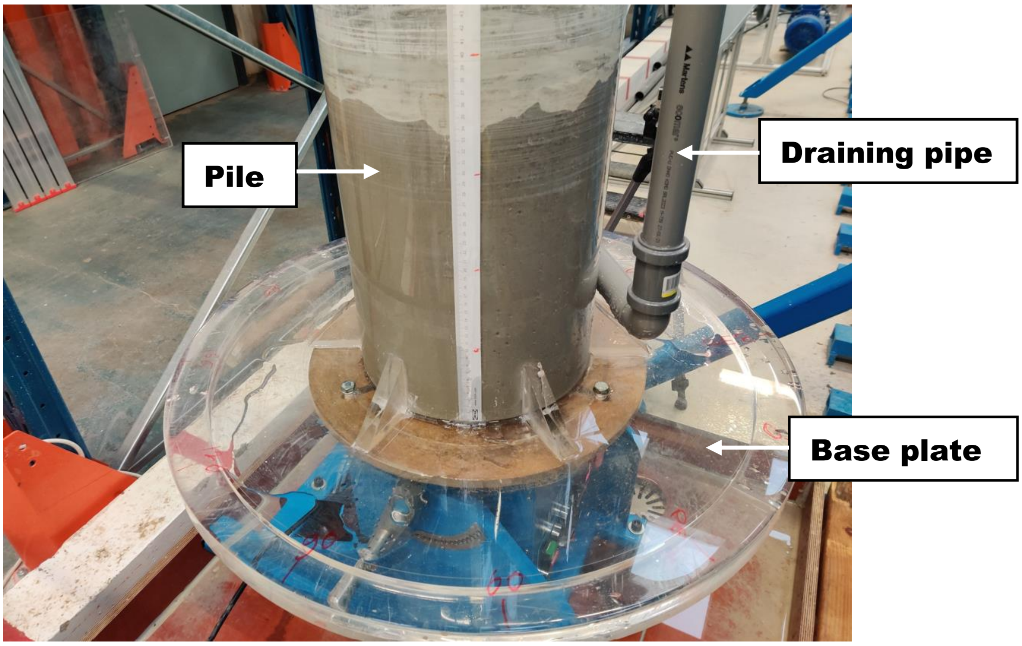

Figure 0-12: pile assembly mounted to the welding positioner

A.4 Jet water distribution system

Figure 0-13: jet water distribution system for MP&HP

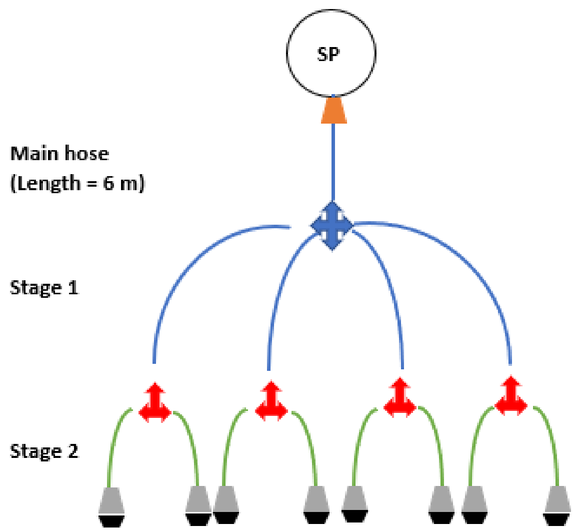

Figure 0-14: schematic representation of jet water distribution system for MP & HP

Hose	Size (inch)	ID (mm)	OD (mm)
	½	12.7	21.8
	¼	6.4	14.7

Fitting	Type	Thread dimensions	Thread
	Screw thread	$M22\ x\ 1{,}5$	Male
	Screw thread	¼″ NPT	Female
	Nozzle	¼″ NPT	Male
	T-Piece		
	Manifold		

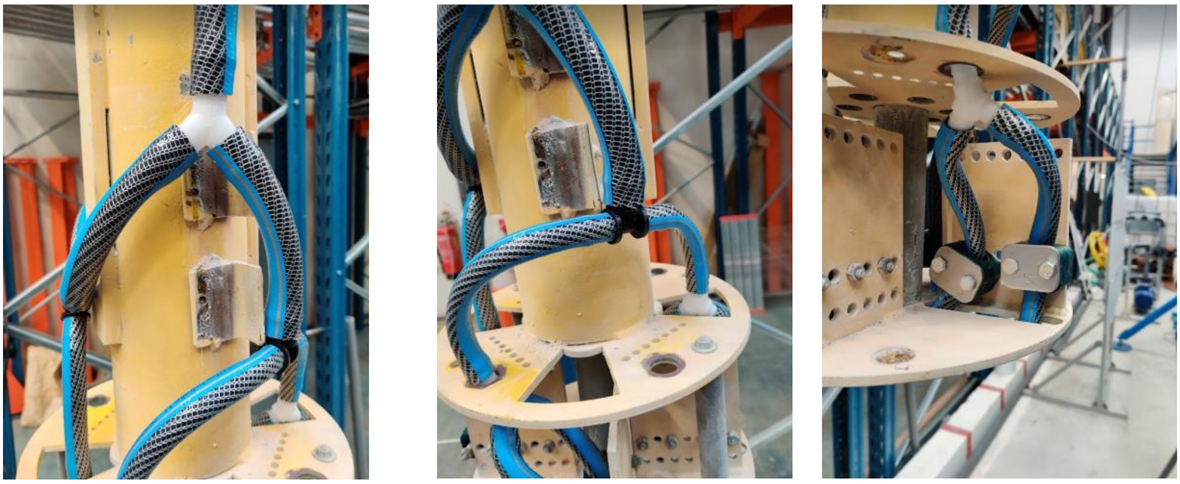

Figure 0-15: jet water distribution system for LP. From left to right: Stage 1, Stage 2, Stage 3 (see schematic representation below).

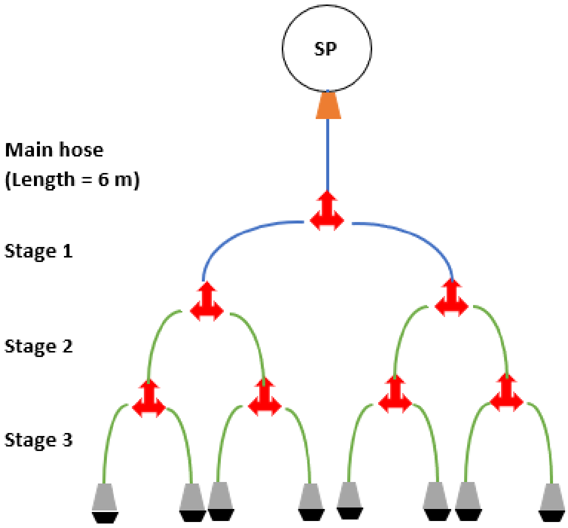

Hose	Size (inch)	ID (mm)	OD (mm)
	¾	19.0	25.1
	½	13.0	16.5

Fitting	Type	Dimension	Thread
	Gardena hose connector	¾ ″	–
	Hose nipple	13 mm x ¼ ″	Female
	Nozzle	¼″ NPT	Male
	POM Y-piece	S1 =19 mm S2 = 19 – 13 mm S3 = 13 mm	–

Figure 0-16: schematic representation of jet water distribution system for MP & HP

Appendix B

Chemical composition clay

B.1 Artificial clay

Cement

Portland cement (CEM I 42,5 N) is widely used to strengthen soils. It is a fine powder produced by grinding clinker, the product of heating limestone and clay materials in a kiln which typically contains 75% calcium silicates, 20% calcium aluminates and 5% gypsum. The constituents of Portland cement are given in Table B1.

Table B1: Constituents of Portland Cement

Constituent	Chemical formula	% by Weight
Tricalcium Silicate	$(CaO)_3 SiO_2$	$45 - 75$
Dicalcium Silicate	$(CaO)_2 SiO_2$	$7 - 32$
Tricalcium Aluminate	$(CaO)_3 Al_2O_3$	$0 - 13$
Tetracalcium Aluminoferrite	$(CaO)_4 Al_2O_3 Fe_2O_3$	$0 - 18$
Gypsum	$CaSO_4 2H_2O$	$2 - 10$

When combined, an exothermic hydration reaction occurs between tricalcium silicate and water, in which calcium hydroxide and calcium silicate hydrate are formed. The cement derives its strength from the calcium silicate hydrate which becomes a hard mass, acting to bind soil particles together.

In a secondary reaction, the calcium hydroxide produced in the hydration reaction combines with silica present in the soil, producing more calcium silicate hydrate which contributes further to the development of strength.

Bentonite

Bentonite clay powder is mineral from volcanic ash with high binding power. It consists mainly of montmorillonite ($\geq 80\%$). It has a high binding capacity and increases its surface in connection with water. This results in its unusually high absorption capacity for deposited substances. Furthermore, a very high binding capacity for pollutants of all kinds is observed. It binds heavy metals and can also bind radioactive elements. It is sometimes added to other clays to increase plasticity.

The constituents of bentonite powder are given in Table B2.

Table B2: Constituents of bentonite powder

Constituent	Chemical formula	% by Weight
Silicon dioxide	SiO_2	57.2
Aluminium oxide	Al_2O_3	23.6
Iron (III) oxide	Fe_2O_3	2.1
Titanium dioxide	TiO_2	0.2
Calcium oxide	CaO	1.4
Magnesium oxide	MgO	2.0
Sodium oxide	Na_2O	1.3
Potassium oxide	K_2O	1.1
L.O.I	-	11

B.2 Natural clay

GOERG & SCHNEIDER
Keramische Massen

Plastic body No. 208, individually wrapped

Chemical analysis:

SiO_2	75.0 %
Al_2O_3	19.8 %
TiO_2	1.4 %
Fe_2O_3	0.9 %
CaO	0.2 %
MgO	0.3 %
K_2O	2.2 %
Na_2O	0.1 %

Ceramic data:

Dry shrinkage in %:	6		
Firing temperature:	1070 ℃	1140 ℃	1240 ℃
Firing colour:	white	light-cream	cream
Firing shrinkage in %:	2	4	7
Water absorption in %:	10	7	1

Coefficient of thermal expansion (CTE):

20 ℃ - 400 ℃	66
20°C - 500 ℃	69
20 ℃ - 600 ℃	83

CTE * 10^{-7}/K

The following technical information is purely informative in character. All sales are bound to the general terms and conditions.
Goerg & Schneider GmbH u. Co. KG, Bahnhofstrasse 4, D-56427 Siershahn

Appendix C

Measuring tables

B1 - 3 bar - 20 kPa							
	Rotational speed [rpm]	**Upper** plate height [cm]	Removed layer [cm]		Duration [s]	Duration [min]	Production [cm/min]
Start	-	53.5					
1	Static	53.5	0		330	5.50	**0.00**
2a	Stepwise 1	53.1	0.4		720	12.00	
2b	Stepwise 2	51.6	1.5		960	16.00	**0.09**
		48.1					
3	1.5	48.1	0.8	No Jets	240	4.00	**0.20**
4	1.5	44.2	3.9		250	4.17	**0.94**
5	2	43.4	0.8	No Jets	240	4.00	**0.20**
6	2	38.7	4.7		250	4.17	**1.13**
7	1	38.2	0.5	No Jets	240	4.00	**0.13**
8	1	35.2	3		250	4.17	**0.72**
End							

B2 - 3 bar - 20 kPa							
	Rotational speed [rpm]	**Upper** plate height [cm]	Removed layer [cm]		Duration [s]	Duration [min]	Production [cm/min]
Start	-	52.6					
1	Static	52.6	0		300	5.00	**0.00**
2a	Stepwise 1	52.3	0.3		720	12.00	
2b	Stepwise 2	51.9	0.4		900	15.00	**0.03**
		47.6					
3	1	47.1	0.5	No Jets	240	4.00	**0.13**
4	1	44.1	3		250	4.17	**0.72**
5	1.5	43.5	0.6	No Jets	240	4.00	**0.15**
6	1.5	39.7	3.8		250	4.17	**0.91**
7	2	39	0.7	No Jets	240	4.00	**0.18**
8	2	34.4	4.6		250	4.17	**1.10**
X1 (t-5hr)	1	33.2	1.2		250	4.17	**0.29**
X2 (t-5hr)	1.5	31.2	2		250	4.17	**0.48**
X3 (t-5hr)	2	28.3	2.9		250	4.17	**0.70**
End							

B3 - 3 bar - 60 kPa							
	Rotational speed [rpm]	**Upper** plate height [cm]	Removed layer [cm]		Duration [s]	Duration [min]	Production [cm/min]
Start	-	52.3					
1	Static	52.3	0		300	5.00	**0.00**
2a	Stepwise 1	52.2	0.1		780	13.00	
2b	Stepwise 2	52.1	0.1		900	15.00	**0.01**
		50.3				0.00	
3	1	49.9	0.4	No Jets	480	8.00	**0.05**
4	1	49.4	0.5		500	8.33	**0.06**
5	1.5	49.2	0.2	No Jets	480	8.00	**0.03**
6	1.5	48.1	0.9		500	8.33	**0.11**
7	2	47.8	0.3	No Jets	480	8.00	**0.04**
8	2	46.3	1.5		500	8.33	**0.18**
End							

B4 - 30 bar - 20 kPa							
Test	Rotational speed [rpm]	Bottom plate height [cm]	Removed layer [cm]		Duration [s]	Duration [min]	Production [cm/min]
Start	-	44.7					
1	Static	44.7	0		600	10.00	**0.00**
2	1	36.9	7.8		420	7.00	**1.11**
3	1	33.8	3.1	No jets	740	12.33	**0.25**
4	1	25.9	7.9		405	6.75	**1.17**
5	2	23.5	2.4	No jets	315	5.25	**0.46**
6	2	12.6	10.9		480	8.00	**1.36**
End							

B5 - 30 bar - 60 kPa							
	Rotational speed [rpm]	Bottom plate height [cm]	Removed layer [cm]		Duration [s]	Duration [min]	Production [cm/min]
Start	-	42.7	-				
1	Static	42.7	0		180	3.00	**0.00**
2	Stepwise 1	42.2	0.5		720	12.00	
3	Stepwise 2	41.7	0.5		900	15.00	**0.05**
		39.9					
4	1	39	0.9	No Jets	600	10.00	**0.09**
5	1	36.4	2.6		600	10.00	**0.26**
6	1.5	35.4	0.8	No Jets	300	5.00	**0.16**
7	1.5	33.7	1.7		300	5.00	**0.34**
8	2	32.7	1	No Jets	300	5.00	**0.20**
9	2	29.9	1.8		300	5.00	**0.36**
End							

B6 - 30 bar - 100 kPa							
	Rotational speed [rpm]	Bottom plate height [cm]	Removed layer [cm]		Duration [s]	Duration [min]	Production [cm/min]
Start	-	46					
1	Static	46	0		270	4.50	**0.000**
2a	Stepwise 1	46	0		780	13.00	
2b	Stepwise 2	46	0		975	16.25	**0.000**
3	1	45	0.9	No jets	610	10.17	**0.089**
4a	1	44.5	0.5		350	5.83	**0.086**
4b	1	44	0.5		330	5.50	**0.091**
4c	1	43.5	0.5		350	5.83	**0.086**
4d	1	42	1.7		1080	18.00	**0.094**
5	2	41	1	No jets	600	10.00	**0.100**
6	2	39	2		1080	18.00	**0.111**
End							

B7 - 130 bar - 20 kPa							
	Rotational speed [rpm]	Bottom plate height [cm]	Removed layer [cm]		Duration [s]	Duration [min]	Production [cm/min]
Start	-	45.5	-				
1	Static	45.5	0		300	5.00	**0.00**
2a	Stepwise 1	44.1	1.4		720	12.00	
2b	Stepwise 2	39.6	3.5		840	14.00	**0.22**
		36.9					
3	1	35.8	1.1	No Jets	300	5.00	**0.22**
4	1	30.9	4.9		180	3.00	**1.63**
5	1.5	29	1.9	No Jets	300	5.00	**0.38**
6	1.5	22	7		180	3.00	**2.33**
7	2	19.7	2.3	No Jets	300	5.00	**0.46**
8	2	10.6	9.1		180	3.00	**3.03**
End							

B8 - 130 bar - 60 kPa							
	Rotational speed [rpm]	Bottom plate height [cm]	Removed layer [cm]		Duration [s]	Duration [min]	Production [cm/min]
Start	-	31.3					
1	static	31.3	0				
2a	Stepwise 1	30.9	0.4		660	11.00	
2b	Stepwise 2	29.8	1.1		840	14.00	**0.07**
		27.6					
3	1	26	1.6		180	3.00	**0.53**
4	1.5	23.1	2.9		180	3.00	**0.97**
5	2	19.2	3.9		180	3.00	**1.30**
End							

B9 - 130 bar - 100 kPa							
	Rotational speed [rpm]	Bottom plate height [cm]	Removed layer [cm]		Duration [s]	Duration [min]	Production [cm/min]
Start	-	32.2	-				
1	Static	32.2	0		300	5.00	**0.00**
2a	Stepwise 1	32.1	0.1		720	12.00	
2b	Stepwise 2	31.9	0.2		900	15.00	**0.01**
3	1	31.4	0.5	No Jets	480	8.00	**0.06**
4	1	30.7	0.7		480	8.00	**0.09**
5	1.5	29.8	0.9	No Jets	480	8.00	**0.11**
6	1.5	28.8	1		480	8.00	**0.13**
7	2	27.9	0.9	No Jets	480	8.00	**0.11**
8	2	26.8	1.1		480	8.00	**0.14**
End							

B10* - 30 bar - 30 kPa							
	Rotational speed [rpm]	Bottom plate height [cm]	Removed layer [cm]		Duration [s]	Duration [min]	Production [cm/min]
Start	-						
1	Static	39.4					
2	1	35.7	3.7		240	4.00	**0.93**
3	1	34.8	0.9	No Jets	240	4.00	**0.23**
4	1.5	30.7	4.1		240	4.00	**1.03**
5	1.5	29.5	1.2	No Jets	240	4.00	**0.30**
6	2	24.9	4.6		240	4.00	**1.15**
	2	23.3	1.6	No Jets	240	4.00	**0.40**
End							

B11* - 30 bar - 30 kPa (NC)							
	Rotational speed [rpm]	Bottom plate height [cm]	Removed layer [cm]		Duration [s]	Duration [min]	Production [cm/min]
Start	-	43.5	-				
1	Static	42.9	0.6		300	5.00	**0.12**
2a	Stepwise 1	41.3	1.6		780	13.00	
2b	Stepwise 2	39.6	1.7		900	15.00	**0.15**
		36.4					
3	1	35.9	0.5	No Jets	240	4.00	**0.13**
4	1	32.8	3		240	4.00	**0.75**
5	1.5	32.2	0.6	No Jets	240	4.00	**0.15**
6	1.5	28.7	3.5		240	4.00	**0.88**
7	2	28	0.74	No Jets	240	4.00	**0.19**
8	2	24.3	3.7		240	4.00	**0.93**
R1	1	21.3	3		240	4.00	**0.75**
R2	1.5	17.9	3.4		240	4.00	**0.85**
R3	2	14.3	3.6		240	4.00	**0.90**
End							

Appendix D
Test protocol

Day before experiment:

1. Check battery level of the camera, charge the battery if necessary
2. Check if nozzles are blocked by debris from previous experiments
3. **Set loadcell to zero**
4. Move welding positioner to the side of the drip tray
5. Check tremie pipe (attach pipe to funnel) → place it in the pile
6. Clay mixture batch
    a. Add bentonite and cement in approximate two sets
    b. Dry mix the bentonite and cement
    c. Add water (max. $10\ L$ per bucket)
    d. Use the hand-held electric mixer to mix all components
    e. **Take a small sample** ($2{,}5\ L$ bucket)
    f. Add clay mixture to the pile (through the tremie pipe)
        i. Add first bucket: read column height and weight
        ii. Add second bucket: read column height and weight
7. Seal the pile with plastic wrap and a bucket lid
8. Move welding positioner back to its initial place, aligning the pile with the jetting tool
9. Clean buckets and tremie pipe
10. Attach drainpipe to orifice

Day of experiment:

1. Attach the camera to the tripod
2. Fill right side of sump tank with water from the fire hose
3. Turn power strip on
4. High-Pressure Pump (HPP)
    a. Plug-in HPP
    b. Check if Gardena hose (water supply line) is correctly fitted to the HPP
    c. Start water supply
    d. Turn on the tap
5. Plug-in Large Submersible Pump (LSP)
6. Start laptop
    a. Open *Labview* front panel
    b. Check if all incoming signals (loadcell, pressure and discharge) are working properly
    c. Enable ''write to measurement file''
7. **Perform a shear vane test** on the sample that was made the day before → report result
8. Remove seal from the pile
9. Lower the tool, at least $0{,}5\ m$ above mudline
10. Place fire hose in the pile
11. **Start logging and camera**
12. **Vent the system**

    a. Open Small Submersible Pump (SSP) PVC ball valve
    b. Plug-in SSP and turn it on
    c. Wait until pile is filled up with water
13. Close SSP PVC ball valve and turn SSP off
14. Open fire hose ball valve
15. Open Dredge Pump (DP) PVC ball valve
16. Turn DP on
17. Regulate discharge through DP discharge line using the gate valve
18. Start the HPP and **set the pressure** to the desired value using the HPP's adjustable pressure regulator
19. **Lower the tool with the wireless crane remote until it reaches the bed**
20. Keep adjusting the height of the tool while keeping an eye on the water level in the pile
21. Collect clay particles during each test using a sieve → take pictures
22. Stop experiment after each single test (inspect measuring tape on the side of the pile)
    a. Turn HPP off
    b. Close fire hose ball valve
    c. Turn DP off
    d. **Stop logging and camera**
    e. Elevate tool
    f. Use vacuum cleaner to remove remaining water
    g. Write down remaining column length and weight
    h. Inspect clay content inside the tool and take pictures → measure trench depth with a tape measure
23. Restart from step 9
24. Stop test (see 22a – 22h)
25. **Save log data → USB → personal laptop→ run Matlab ''basis script''**
26. Cleaning
    a. Clean-up spilled water
    b. Remove pile from welding positioner
    c. Disconnect HPP from tool
    d. Connect spray lance to HPP to remove clay remnants from pile
    e. Put pile back on top of the welding positioner
    f. Reattach HPP to the tool
27. Close water supply
28. Turn off the tap
29. Unplug HPP and submersible pumps
30. Turn power strip off
31. Collect camera and transfer videos to personal laptop
32. END